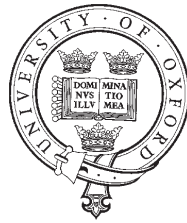


NMR Quantum Information Processing with *Para*-Hydrogen



A thesis submitted for the degree of
Doctor of Philosophy

Muhammad Sabieh Anwar
University College, Oxford
Trinity Term 2004

Abstract

NMR Quantum Information Processing with *Para*-hydrogen

A thesis submitted for the degree of Doctor of Philosophy

Muhammad Sabieh Anwar

University College, Oxford

Trinity Term 2004

Liquid state NMR quantum information processors are dominated by the problem of preparing pure initial states. Traditionally these devices employ pseudopure states instead of truly pure states, but this approach is not scalable. Furthermore, almost all previous demonstrations of information processing in liquid state NMR used separable states which can in principle be described by classical models. This thesis addresses the two-fold problem of initialization and separability by preparing pure quantum states lying above the entanglement threshold. Our pure state quantum computer derives its purity from the highly polarized nuclear spin states in the *para*-hydrogen molecule.

The thesis begins with a critique of conventional NMR based quantum information processing in Chapter 1, outlining the major strengths and weaknesses of the technology. Chapter 2 describes the enhanced magnetic ordering of the nuclear spin states in *para*-hydrogen and Chapter 3 describes an initialization experiment exploiting this effect to achieve pure, entangled states. These states can indeed be used as initial states in implementing quantum algorithms. This is shown in Chapter 4, which describes an implementation of the Deutsch and the Grover quantum algorithms.

The “twirl” operation converts a completely arbitrary input state to a Werner singlet. The NMR implementation of this operation is taken up in Chapter 5. Chapter 6 analyzes the possibility of sharing the purity of some highly polarized qubits in a quantum computer onto quantum subspaces of arbitrary dimensions, and whether these sharing operations increase or decrease the likelihood of entanglement.

Finally, this dissertation has six Appendices which contain notes on singlet-triplet mixtures, isotropic mixing sequences, systematic errors in singlet detection, data processing and decoherence modelling.

Acknowledgements

My D.Phil. work was a part of a cross-university research initiative. As such, I had the opportunity to participate in a truly wonderful mix of specialist skills. It is my great pleasure to thank Simon Duckett and Damir Blazina, without whose involvement, this project would have been impossible to realize. From the preparation of ultra-cold *para*-hydrogen to implementing our pulse sequences, they showed great skill (and patience) in deciphering my comments and incorporating them into their experiments. Thanks indeed! Similarly, Hilary Carteret in Montreal always kept me on my toes in her scintillating email conversations regarding the many theoretical aspects of our project. Many thanks to her.

Many thanks also to my post-doctoral colleague Li Xiao for implementing my twirl sequences and promising to read this thesis. I would also like to thank my doctoral colleague Tony Short for acting as an instant first source of reference for my many mathematical curiosities, and for adding a new impetus to my work on the twirl operations. Another colleague who deserves my utmost thanks is Iain Day in the Chemistry Department, for assisting and guiding me through my experiments on the NMR spectrometer. I would also like to extend my thanks to Lieven Vandersypen and to Thomas Schulte-Herbrüggen for kindly answering my questions on decoherence modelling and unitary control.

My financial and, to a large extent, my social life were taken care of by the Rhodes House at Oxford. Mary Eaton, Sheila Partridge and Catherine King have helped me in numerous ways. My sincere thanks to them as well.

A great number of friends have contributed to my Oxford life in various ways. I would specially like to mention Adeel Malik, Ali Abbas, Omer Suleman, Zunnoor Tarique, Sajid Javed, Samina Yasmin, Usman Latif, Nadir Cheema, Niharika Gupta, Edward Dewey and Eleni Hatzivassiliou for their love and constant encouragement; Mark Bowdrey, Garry Bowen, Jon Walgate, Salvador Venegas, Yasser Omar, Lucien Hardy, Mike Mosca, Raymond Laflamme and Alex Pines for many useful discussions; the Oxford University Pakistan Discussion Forum for accomplishing my literary missions; the Islamic Society for the Friday prayers in Wadham College and Gilian Evisson for giving me the master key to unlock the many treasures inside the Bodleian Libraries. All of them make my three years in Oxford look so precious.

There is however a debt of gratitude I *cannot* repay; to my supervisor Jonathan Jones who has helped me at every single step of my research. Knowing Jonathan as a teacher and as a friend has been the most satisfying experience in Oxford. His encouraging help and wisest counsel in matters of both physics and life beyond, are definitely the most valuable memories I shall be taking back home.

There is many a time when words fall short of feelings. It is difficult to express my thoughts for my family. It is fair to admit that all my accomplishments, large or small, are possible because of my parents' unparalleled support and their constant prayer for me. My fondest wishes also go to Rafay, Abu Bakar and Mehvesh who have devoted much time in their joyous youth to thinking about their brother here in Oxford. I have missed them as well.

Last but not the least, I am still thinking of a way to possibly thank my grandmother who could not outlive the three very long years she had spent, longing to see her grandson back in her loving presence.

The Wayfarer's Supplication

"Submitting myself to the test of patience,
Like the rose's scent, I bid farewell to my garden.

In my search of the wine of knowledge,
I have left my homeland, hunting new taverns.

A tree in the desert, my eyes cling onto the clouds
Of *Your* Magnanimity, and not on the gardener.

O Lord, keep me far ahead of my caravan,
So that they consider me as their destination.

The nest I had assembled straw by straw,
O God, May I see that same abode of mine.

And may I lay my forehead at my parents' feet,
by whose blessing, I possess the secret of Love."

Contents

1	Liquid state NMR quantum information processing—a critique	2
1.1	NMR States, Coherence and Dynamics	4
1.1.1	Ensemble quantum computing	4
1.1.2	Product operator basis	5
1.1.3	Coherences	6
1.1.4	Detection in NMR	8
1.1.5	Chemical shift	9
1.1.6	Spin-spin coupling	9
1.1.7	The NMR Hamiltonian	10
1.1.8	Dynamics	11
1.1.9	Quantum logic gates	12
1.1.10	Decoherence	13
1.1.11	Gradients	14
1.1.12	Quantum state tomography	15
1.2	Initialization in NMR	16
1.2.1	Initial states in “thermal” NMR	16
1.2.2	Pseudopure initial states	20
1.2.3	Climbing “Mount Scalable”?	22
1.2.4	Concentrating polarization	23
1.2.5	Re-initialization	25
1.3	Measurement in NMR	25
1.4	Entanglement in NMR	26
1.4.1	Separable and entangled states	27
1.4.2	Separability bounds for mixed states in NMR	28
1.4.3	(Quantum) nature of liquid state NMR (quantum) information processing	30

1.4.4	Detecting entanglement in two qubit states	33
1.4.5	Quantifying entanglement in two qubit systems	34
1.4.6	Entanglement in singlet-triplet mixtures	35
1.5	Methods for enhancing polarization	38
1.5.1	High fields and low temperatures	39
1.5.2	Polarization transfer from nuclear spins	39
1.5.3	Polarization transfer from electron spins	39
1.5.4	Chemically induced dynamical nuclear polarization	41
1.5.5	<i>Para</i> -hydrogen derived hyperpolarization	42
2	<i>Para</i>-hydrogen induced polarization	43
2.1	Spin isomers of hydrogen	44
2.2	<i>Para</i> -hydrogen from the perspective of statistical mechanics	48
2.2.1	<i>Para-ortho</i> ratios	49
2.3	Preparation of <i>para</i> -hydrogen	50
2.4	Chemical addition reactions with <i>para</i> -hydrogen	53
2.5	Operator description of the nuclear spin states in the <i>para</i> -hydrogen experiment	56
2.6	<i>Ex situ</i> hydrogenation	57
2.7	<i>In situ</i> hydrogenation	58
2.8	PHIP signal forms and enhancements	60
2.9	Singlet dynamics in strong field	65
2.10	Delayed PASADENA	68
2.11	Incoherent PASADENA	69
2.12	Isotropic PASADENA	71
2.13	Summary of PHIP signals	73
3	Preparing pure initial states using <i>para</i>-hydrogen	75
3.1	One-shot tomography	76
3.1.1	Implementing the partial twirl	78
3.1.2	Finite duration gradient pulses	79
3.2	The detection pulse	80
3.2.1	Implementing the selective detection pulse	81
3.3	Experimental system and methods	84
3.3.1	Chemical system	85

3.3.2	Optical assembly	87
3.3.3	Dihydride spectra	88
3.3.4	Control experiment	91
3.3.5	Active volume correction	93
3.3.6	Depletion of the precursor	94
3.4	Data processing	97
3.4.1	Peak integration	97
3.4.2	J processing	98
3.4.3	State tomography results	103
3.5	CW experiments	103
4	Implementation of quantum computation with the pure state quantum computer	
4.1	Deutsch's algorithm with pure quantum states	109
4.2	Grover's quantum search with pure quantum states	109
5	Practical implementation of twirl operations	110
6	Purity sharing	112

Chapter 1

Liquid state NMR quantum information processing—a critique

Liquid state nuclear magnetic resonance (NMR) [1, 2, 3, 4, 5, 6, 7] is a vital spectroscopic technique in analytical chemistry. It also plays a crucial role in present day medicine as a valuable imaging technology. Recently, NMR has also sought new relationships: interfacing with myriad fields in the biological and physical sciences, probing living and non-living specimens of all kinds, and now, in the form of *functional* imaging, it is taking the first few strides towards an understanding of the way humans think and act! One such exciting partnership is with quantum information processing (QIP) [8, 9], now blossoming into an established discipline in its own right. This thesis explores some facets of this ‘NMR-QIP’ interface.

NMR-QIP capitalizes on fifty years of experience in probing nuclear spins in liquid solution with radio-frequency (RF) pulses. In fact, several essential features of experimental QIP, such as Rabi oscillations [10] in single qubits, coherent manipulations of multi-qubit systems and decoherence control have long been developed and implemented in traditional NMR, decades before QIP was investigated as an independent discipline. Today, liquid state NMR is not only a leading technology for demonstrating quantum computing (QC) in small physical systems, but also enriches QIP, by inspiring new ideas for theoretical and experimental investigation.

Like all the different ideas being pursued for the physical realization of quantum computers, liquid state NMR comes with its strengths and weaknesses. A useful set of criteria was laid out by DiVincenzo [11] and since then, it has become customary to

evaluate practical QC schemes [12, 13, 14] on the basis of these rules, which are listed below:

1. there must exist well-defined, physical qubits and the system should be scalable to higher dimensions;
2. the qubits must be initializable into a well-defined quantum state;
3. the decoherence times must be long compared to the times for gate operation;
4. there must also exist a set of quantum gates capable of implementing universal quantum dynamics; and
5. it should be possible to perform single-qubit measurements.

Most of my D.Phil. research revolves around one of the major problems with liquid state NMR¹, namely initialization (criterion 2). Consequently, in this chapter, I choose to present a detailed description of the intrinsic weaknesses in conventional NMR, and only touch upon the strengths. Furthermore, this chapter is not intended to become another review of NMR-QIP; there are already excellent tutorials and monographs on the subject, such as [8, 15, 16, 17, 18, 19]. Instead, the specific aim of this chapter is to introduce the basics, to guide the reader through the material in subsequent chapters and also, to come up with a motivation for the forthcoming chapters.

Liquid state NMR quantum computers, reaching seven qubits [20], are known to be far ahead of competing technologies, at least in terms of the implementation of quantum algorithms [20, 21, 22, 23, 24, 25, 26, 27, 28, 29]. (Recently, the Deutsch-Jozsa algorithm has been implemented on a two qubit ion trap quantum computer [30].) This relative success has been made possible by the ease as well as robustness with which unitary operations can be implemented in NMR. These strengths are mentioned in Section 1.1, which describes the NMR states, coherences and universal unitary dynamics (criteria 1, 3 and 4) and also introduces the necessary notation. The problems of initialization and single qubit read-out (criteria 2 and 5) are discussed in Sections 1.2 and 1.3. Another problem, not directly encompassed in DiVincenzo's criteria, is the issue of separability and entanglement. Traditional NMR is critically analyzed in view of this requirement in Section 1.4 and finally, general methods for addressing the problem of low polarizations are addressed in Section 1.5.

¹From here onwards, NMR means 'liquid state NMR', unless the solid state is explicitly mentioned.

1.1 NMR States, Coherence and Dynamics

A qubit is a two level quantum system. A spin s nucleus has $2s + 1$ energy levels; the qubits in NMR are (generally) spin $1/2$ nuclei, and so I often use the words ‘qubit’ and ‘spin’ interchangeably. The two energy levels are labelled $|\alpha\rangle$ and $|\beta\rangle$ (or $|0\rangle$ and $|1\rangle$), and these states also serve as the computational eigenstates [15]. The most readily available two level systems are ^1H , ^{19}F , ^{31}P , ^{13}C and ^{15}N , and what characterizes these qubits are their *Larmor frequencies* [3], which in the presence of a magnetic field, B_0 , are,

$$\omega = -\gamma B_0 \tag{1.1}$$

γ being the gyromagnetic ratio of the nucleus. The qubits are therefore “identified” in frequency space, and can be perturbed by applying resonant electromagnetic radiation. For the nuclear spin levels, the Larmor frequencies (and therefore the resonant radiation) are in the RF region of the spectrum. An NMR spectrometer is a highly sophisticated, computer controlled radio receiver and transmitter, capable of delivering electromagnetic radiation to nuclei in a liquid solution placed in a strong superconducting magnet, and of detecting a time-resolved RF signal generated by the nuclei. The signal is Fourier transformed and a frequency spectrum is obtained, with the qubits identifying themselves by their individual frequencies. In short NMR furnishes well characterized qubits, partially satisfying the first DiVincenzo criterion. About the other half, that is scalability, I will say more in Section 1.2.

1.1.1 Ensemble quantum computing

In the NMR setting, each qubit resides in a molecule, along with other nuclei, with arbitrary spins. In the sample, there will be a large number of these molecules; for example, in 1 ml of a 1 mM solution, there will be roughly 10^{17} , rapidly tumbling in the liquid. As there is one n qubit quantum computer per molecule, so the sample will contain an ensemble of quantum computers. All these quantum computers are identical, act in parallel and collectively participate in producing a time-dependent macroscopic magnetization, which is manipulated and detected in the NMR experiment. A convenient language to describe such ensembles is the density operator formalism [8, 31]. An n qubit state, for example, is represented as an $2^n \times 2^n$ density matrix, expanded in some operator basis. In this thesis, I shall use the notation $N = 2^n$ for the Hilbert

dimensions of an n qubit quantum system. Different basis sets, each comprising 4^n basis elements, are in use [2]; however, one set which is the most common in the NMR community is the *product operator* [2, 32, 33, 34] set, which I now describe.

1.1.2 Product operator basis

The product operator basis elements are represented as $N \times N$ matrices and are simply re-scaled versions of products of the Pauli operators [8]. For a single qubit, the correspondence² is,

$$\frac{\mathbf{1}_2}{2} = \begin{pmatrix} 1/2 & 0 \\ 0 & 1/2 \end{pmatrix} = \frac{1}{2}\sigma_0, \quad (1.2)$$

$$I_x = \begin{pmatrix} 0 & 1/2 \\ 1/2 & 0 \end{pmatrix} = \frac{1}{2}\sigma_x, \quad (1.3)$$

$$I_y = \begin{pmatrix} 0 & -i/2 \\ i/2 & 0 \end{pmatrix} = \frac{1}{2}\sigma_y, \quad \text{and} \quad (1.4)$$

$$I_z = \begin{pmatrix} 1/2 & 0 \\ 0 & -1/2 \end{pmatrix} = \frac{1}{2}\sigma_z. \quad (1.5)$$

The symbol $\mathbf{1}_N$ is an example of a general notation I shall use for an $N \times N$ identity matrix. The matrix, $\mathbf{1}_2/2$, is commonly denoted as $\frac{1}{2}E$ in the NMR literature, but I shall keep to the notation introduced above. A single qubit density matrix, ρ can always be uniquely expanded in terms of these four basis elements,

$$\rho = \frac{\mathbf{1}_2}{2} + \sum_{i=x,y,z} c_i I_i, \quad (1.6)$$

which has unit trace matrix as it should [8], and the coefficients c_i are given by,

$$c_i = \text{Tr}(\rho I_i) / \text{Tr}(I_i^2) = 2 \text{Tr}(\rho I_i), \quad (1.7)$$

$\text{Tr}(\dots)$ representing the trace operation. It is traditional to represent operators of the qubits with labels I , S , R , and so on³. For a two qubit system, the $4^2 = 16$

²An operator basis is representation-independent whereas “writing” the basis elements in matrix form requires a representation basis. All matrices in this thesis are written in the so-called Zeeman basis [2, 6, 15], which is formed by taking the direct products of the Zeeman eigenstates, which are also the computational eigenstates. The ordering that I follow in writing these matrices is the traditional $\{|\alpha\alpha\rangle, |\alpha\beta\rangle, |\beta\alpha\rangle, |\beta\beta\rangle\}$ order.

³Sometimes, the notation $I_1, I_2 \dots$ is used, especially for homonuclear systems.

product operators are constructed by taking the tensor products of single spin operators according to,

$$2 \times I_i \otimes S_j, \quad i, j = x, y, z \quad (1.8)$$

$$2 \times \frac{\mathbf{1}_2}{2} \otimes S_j, \quad j = x, y, z \quad (1.9)$$

$$2 \times I_i \otimes \frac{\mathbf{1}_2}{2}, \quad i = x, y, z \quad \text{and} \quad (1.10)$$

$$2 \times \frac{\mathbf{1}_2}{2} \otimes \frac{\mathbf{1}_2}{2} = \frac{\mathbf{1}_4}{2}. \quad (1.11)$$

It is also common practice to drop the multiplication signs, and by slight abuse of notation, represent the two qubit operators with the same symbols as used for the single qubit (*e.g.*, $2 \times \mathbf{1}_2/2 \otimes S_j = \mathbf{1}_2 \otimes S_j \equiv S_j$), the exact meaning being apparent from the context. For example, the sixteen product operators for a two qubit system are given in Table 1.1. Any two qubit state can be expanded in terms of these product operators,

$$\rho = \frac{1}{2}(\frac{\mathbf{1}_4}{2}) + \sum_{i=x,y,z} c_i I_i + \sum_{i=x,y,z} d_i S_i + \sum_{i=x,y,z} e_{ij} 2 I_i S_j. \quad (1.12)$$

The factor of $1/2$ in front of the scalar element $\mathbf{1}_4/2$ ensures that ρ has unit trace and the coefficients c , d and e are calculated in a manner similar to (1.7). Furthermore, the $\mathbf{1}_4/4$ term does not evolve under unitary operations [31] and from the point of view of the state dynamics, is totally “dormant”. The state is called the *maximally mixed state* and is often dropped out from the state expansion, (1.12). As a result, only the *traceless* operators are written in the expansion and a unit trace scalar operator is *assumed*. The traceless part is called the *deviation* matrix [7, 15]. Although the distinction between the “real” and the deviation state is immaterial for traditional NMR and signal detection, for QIP calculations it is better to carefully appreciate this difference: therefore, I strictly use the symbol ‘ \sim ’ whenever I write only the deviation part of the state expansion. Moreover, I represent diagonal matrices with the notation $\{\{\dots\}\}$, with the diagonal elements inside the braces and reserve single braces $\{\dots\}$ for writing general lists of numbers or vectors. For the physical meaning (or lack thereof,) of the product operators, one may refer to [3].

1.1.3 Coherences

In Table 1.1, I have grouped together the product operators in terms of their *coherence order*. The concept can be defined in terms of the positions of non-zero elements in their

Scalar element	$\mathbf{1}_4/2$
Single quantum coherences	I_x, I_y, S_x, S_y $2I_xS_z, 2I_yS_z, 2I_zS_x, 2I_zS_y$
Populations	$I_z, S_z, 2I_zS_z$
Multiple quantum coherences	$2I_xS_x, 2I_yS_y, 2I_xS_y, 2I_yS_x$

Table 1.1: The 16 product operator basis elements for a two qubit (IS) system. The basis elements are grouped according to their coherence orders.

matrix representations. The *single quantum coherences* are located in the positions,

$$\begin{pmatrix} & \square & & \square \\ \square & & & \\ \square & & & \square \\ & \square & & \square \end{pmatrix}, \quad (1.13)$$

and the operators $\{I_x, I_y, S_x, S_y, 2I_xS_z, 2I_yS_z, 2I_zS_x, 2I_zS_y\}$ comprise only these coherences. The zero and double quantum coherences are in the positions,

$$\begin{pmatrix} & & \square \\ & \square & \\ \square & & \end{pmatrix} \quad \text{and} \quad \begin{pmatrix} & & \square \\ & & \\ \square & & \end{pmatrix}, \quad (1.14)$$

and are collectively designated *multiple quantum coherences*. Similarly, the diagonal terms are called the *populations* and in certain respects behave like zero quantum terms. (The matrix representations of the 16 product operators are tabulated in [6, 7].)

The spin operators involving multiple coherence terms are also expressed in terms of their linear combinations,

$$ZQ_x = \frac{1}{2}(2I_xS_x + 2I_yS_y), \quad (1.15)$$

$$ZQ_y = \frac{1}{2}(2I_yS_x - 2I_xS_y), \quad (1.16)$$

$$DQ_x = \frac{1}{2}(2I_xS_x - 2I_yS_y) \quad \text{and} \quad (1.17)$$

$$DQ_y = \frac{1}{2}(2I_yS_x + 2I_xS_y). \quad (1.18)$$

This allows us to define a new basis, which I call the *product operator-multiple quantum* basis, spanned by the product operators for single quantum terms and populations and $\{ZQ_x, ZQ_y, DQ_x, DQ_y\}$ for the multiple quantum terms.

Two other bases will be occasionally used in parts of this thesis. One is the *spherical basis* [2], in which the single qubit operators are related to the product operators through,

$$I^\pm = I_x \pm iI_y, \quad (1.19)$$

and I_z and $\mathbf{1}_2/2$ are left unchanged; the multiple qubit operators are formed analogously to (1.8)–(1.11), by taking tensor products. The other basis I shall occasionally refer to, is the *polarization operator* [2] basis, in which I_x and I_y are unchanged, and I_z and $\mathbf{1}_2/2$ are replaced by,

$$I_\alpha = \frac{\mathbf{1}_2}{2} + I_z \quad \text{and} \quad (1.20)$$

$$I_\beta = \frac{\mathbf{1}_2}{2} - I_z, \quad (1.21)$$

which are in fact equal to the projection operators $|\alpha\rangle\langle\alpha|$ and $|\beta\rangle\langle\beta|$.

1.1.4 Detection in NMR

All NMR experiments can be described in terms of transfers of coherence orders [3, 6]. Even the detection process can be clarified using the language of coherences. For example, in a standard NMR experiment, only the single quantum coherence terms can be detected. As such, they are called the *direct observables*. Suppose we wish to detect a state ρ : then only the single quantum terms in the expansion (1.12) will contribute to the signal, while all other terms will remain unobservable,

$$\rho \xrightarrow{\text{observe}} \{I_x, I_y, S_x, S_y, 2I_xS_z, 2I_yS_z, 2I_zS_x, 2I_zS_y\}. \quad (1.22)$$

The terms $\{I_x, I_y, S_x, S_y\}$ represent *in-phase* and $\{2I_xS_z, 2I_yS_z, 2I_zS_x, 2I_zS_y\}$ indicate *anti-phase* magnetization. The single quantum coherences are also assigned [3] a positive or negative sign, depending on whether they are positioned above or below the diagonal. The way quadrature detection [3, 35] is conceptually employed in modern spectrometers, measures only one kind of, (say, the negative) coherence terms; the mechanism is carefully spelled out in [3].

The spherical and polarization operators are used in predicting the NMR spectrum acquired from a state ρ . I define a *signal vector*, \mathbf{Sg} , with the terms,

$$\{Tr(\rho I_+ S_\alpha), Tr(\rho I_+ S_\beta), Tr(\rho I_\alpha S_+), Tr(\rho I_\beta S_+)\}. \quad (1.23)$$

The two leftmost entries indicate resonances of the I spin, and the two rightmost entries indicate resonances of the S spin. Mathematically, for an exponentially decaying sinusoidal time domain signal, called the *free induction decay* (FID), these resonances appear as Lorentzian lineshapes [3, 6, 7] in the spectrum; real values in \mathbf{Sg} indicate absorptive and imaginary values represent dispersive character.

1.1.5 Chemical shift

The I and S spin resonances, appearing in the NMR spectrum are distinct because the I and S qubits are different nuclei having different Larmor frequencies, (1.1). This is most obviously true for a *heteronuclear* system, involving spins with different chemical identities, such as ^1H and ^{13}C . However, NMR spectra reveal that even if the I and S spins have the same chemical identity, *i.e.*, they form a *homonuclear* system, their frequencies can be different. Each spin is surrounded by a cloud of electrons, which *shields* the externally applied field, B_0 , changing the effective field⁴ seen by the nucleus to $B_0(1 - \sigma)$. The Larmor frequency, (1.1), of each spin is, therefore, shifted,

$$\omega = -\gamma B_0(1 - \sigma). \quad (1.24)$$

If different spins belonging to a homonuclear system, have different electronic environments and therefore, different *chemical shifts*, they can still act as distinct qubits. A useful parameter is the difference in frequencies, $2\pi\delta$ (δ is assumed to be in Hz), signifying how far apart the qubit resonances are: for a pair of homonuclear spins such as two protons, δ is of the order of a kHz, whereas for heteronuclear systems, it can easily be a few hundred MHz.

1.1.6 Spin-spin coupling

For purposes of QIP, it is important, that we have two or more qubits per quantum computer, and that these qubits interact with one another. The interaction between

⁴Some authors use the ‘deshielding convention’, in which B_0 is replaced by $B_0(1 + \delta)$.

spins can assume different forms [2, 36, 37], isotropic and anisotropic, direct and indirect, depending on the molecular motions, and the physical state of the sample. In solids and liquid crystals, the interactions are dominated by direct, dipole-dipole magnetic interactions between the nuclei. The NMR of such anisotropic media is a separate realm altogether; a very good textbook on the subject is [36] and examples of QIP with dipolar coupled qubits are presented in [38, 39, 40].

In liquids, with which we are concerned, motional averaging [3] leaves us with a non-zero isotropic value of a kind of indirect coupling between the spins, which is called the J or *scalar coupling*. This magnetic spin-spin coupling is mediated by electrons bonding the nuclei, and is a kind of Fermi-contact interaction. Typical values of J are a few Hz for ^1H – ^1H couplings and slightly larger, that is between 100–200 Hz for one bond ^{13}C – ^1H couplings. The signal vector, (1.23) suggests the excitation of four lines in the spectrum of a two qubit system: in fact, the scalar coupling causes each peak to split into two halves. The first two elements, $\text{Tr}(\rho I_+ S_\alpha)$ and $\text{Tr}(\rho I_+ S_\beta)$, for example, represent the two I spin resonances, when the neighbouring S spin is in the $|\alpha\rangle\langle\alpha|$ or $|\beta\rangle\langle\beta|$ state.

In the NMR tradition, a pair of spins is classified as *weakly coupled*, if $\delta \gg J$; the system is said to be of the type **AX**. This will be the case for heteronuclear systems as well as for many homonuclear systems in the presence of strong magnetic fields, B_0 . The system is classified as *strongly coupled* [6, 7], and of the type **AB**, if $\delta \lesssim J$. Such systems are the prevalent case in weak or near zero fields. The extreme case is an **A₂** system, in which $\delta = 0$, where the spins become *equivalent* and have identical frequencies. Even two heteronuclear spins, in zero field conditions, would form an **A₂** system.

1.1.7 The NMR Hamiltonian

For a two qubit, **AB** system, the NMR Hamiltonian [1, 2, 3, 6] is given by,

$$H = \hbar(\omega_I I_z + \omega_S S_z + \pi J 2\mathbf{I} \cdot \mathbf{S}), \quad (1.25)$$

where $\mathbf{I} \cdot \mathbf{S}$ is short-hand for

$$\frac{1}{2}(2I_x S_x + 2I_y S_y + 2I_z S_z), \quad (1.26)$$

and in the weak coupling limit, *i.e.*, for an **AX** system, it becomes,

$$\hbar(\omega_I I_z + \omega_s S_z + \pi J 2 I_z S_z). \quad (1.27)$$

I call these Hamiltonians **AB** and **AX** Hamiltonians. In these expressions, ω_I and ω_s represent the chemically shifted Larmor frequencies, (1.24), of the two qubits, and I subsequently follow the convention of setting $\hbar = 1$. It is also customary, to write the rotating frame [3] versions of these Hamiltonians, replacing each ω by $\Omega = \omega - \omega_{rf}$, ω_{rf} being the frequency of the rotating frame⁵, generally taken to be equal to the transmitter frequency [41]. In this dissertation, I shall mostly deal with homonuclear systems in the weak coupling limit.

The Hamiltonian discussed so far is the background or the internal Hamiltonian, under which the system evolves at all times. A resonant magnetic field is applied to perturb the spins. This control field, B_1 is perpendicular to the static field, B_0 and oscillates in the perpendicular plane (the *transverse* plane) with a frequency ω_{RF} , expected to be close to the Larmor frequencies of the spins in order to satisfy the resonance condition. The oscillatory field, in addition to a frequency and amplitude parameter, also possesses a phase factor ϕ in the transverse plane; the control Hamiltonian for a perturbation on a single qubit is given by,

$$H_{RF} = \omega_1 (I_x \cos(\omega_{RF}t + \phi) + I_y \sin(\omega_{RF}t + \phi)), \quad (1.28)$$

where $\omega_1 = -\gamma B_1/2$ is called the *nutaton frequency*. The nutation frequency (amplitude), phase, radio frequency and the time for which this control field is applied, can all be modulated in time to achieve the desired state dynamics.

1.1.8 Dynamics

Corresponding to a Hamiltonian that is piecewise constant in time, $H_1, H_2, \dots H_k$, acting for time intervals $t_1, t_2, \dots t_k$, we can construct a propagator,

$$U = \mathcal{T}_k \exp(-iH_k t_k), \quad (1.29)$$

where \mathcal{T} is the Dyson time-ordering operator [2], and a state ρ evolves according to the Liouville-von Neumann equation [2],

$$\rho \rightarrow U\rho U^\dagger; \quad (1.30)$$

⁵The symbol for rotating frame ‘rf’ should not be confused with ‘RF’ for radio frequency.

the correspondence between this equation and the Schrodinger's equation is analogous to the relationship between the the density matrix and the pure state. What is referred to as a *pulse* in this thesis, is the pulse propagator,

$$P = \exp(-iH_{RF}t_p). \quad (1.31)$$

Selecting suitable times t_p , it is possible to achieve desired flip angles; for example, if $\omega_1 t_p = \pi/2$, the pulse flips the magnetization through 90° . I shall represent a pulse with a flip angle of θ° , with a phase angle ϕ by the symbol θ_ϕ , and for RF fields along the cardinal axes, I shall simply represent the phases by $\{x, y, -x, -y\}$. For example, in my notation, a pulse with flip angle 180° and phase of 180° , would be written as 180_{-x} . So far, I have assumed all axes of rotation to lie in the transverse plane. This is not a strict assumption, as rotations around arbitrary axes in the Bloch sphere [8] can also be implemented using composite rotations [4, 5, 42, 43, 44, 45]. This includes rotations around the $\pm z$ axes [46].

The product operators also facilitate predicting the dynamics of the spin operators. We make use of a theorem [6, 7]: for a set of three operators satisfying $[A, B] = iC$ and its cyclic variations, A evolves under the propagator $\exp(-i\theta C)$ as,

$$A \xrightarrow{\exp(-i\theta C)} A \cos(\theta) + B \sin(\theta). \quad (1.32)$$

1.1.9 Quantum logic gates

The standard network model of quantum computation [8] assumes a network built up of logic gates [47]. In NMR, these gates are generally implemented [48, 49, 50, 51, 52] through a sequence of pulses and intervals of free precession (under the internal Hamiltonian). Stated simply, single qubit gates can be implemented by pulses exciting only one qubit in the system, whereas two qubit gates normally exploit the J coupling between the spins, and often make use of the spin-echo pulse sequence [3, 4, 6]. Logic gate design often involves “sculpting” the Hamiltonian, making use of the concepts learned from average Hamiltonian theory [2]. Sometimes, use is made of frequency selective pulses, so called *soft pulses* [4], exciting peaks from a single qubit, or “finer tuned”, transition selective pulses [53, 54], exciting only one peak in a group. These selective pulses, also come with their concomitant problems of cross-talk with other qubits and coupling evolutions during finite pulse lengths; different methods have been devised

[55, 56, 57] to ameliorate these effects. In our work [58, 59], we mostly implemented selective pulses using hard pulses and periods of free precession, a technique based on the Jump-and-Return [60] sequences. I shall return to this method in Chapter 3. Furthermore, in Chapter 5, we achieve selective excitation, using a method devised by Fortunato *et al.* [61], which numerically searches for a shaped pulse profile, that maximizes some pre-defined fidelity measure. Experimentally, all pulses, be they soft or frequency non-selective (*hard*) [4], always have instrumental imperfections leading to *systematic* errors [18, 35], and these can also be tackled [62, 63, 64, 65] very effectively. (These errors are also considered in Appendix ??.) In this dissertation, I represent soft pulses achieving a flip angle of θ , as θI_ϕ or θS_ϕ , exciting the I or S spin, and hard pulses as θ_ϕ without a spin label.

It was shown early on [66] that a controlled-NOT (c-NOT) gate together with single qubit rotation, suffices for implementing universal quantum computation [67]. NMR readily provides c-NOT and single qubit rotations, and can therefore, *simulate* universal dynamics, to some required accuracy, satisfying the fourth DiVincenzo criterion. In fact, a major factor contributing to the early success of liquid state NMR, was the reliability and flexibility of applying arbitrary unitary propagators to the system, making it a convenient test-bed for many quantum experiments.

1.1.10 Decoherence

Decoherence [8] is the decay of coherences, leading to the gradual decay of off-diagonal terms in the density matrix. The time-scale over which this decay takes place is important, because quantum computations can only last for times shorter than this characteristic length of time, putting an upper limit on the length of computations, before the quantum computer “collapses” into a set of so-called *pointer* states [68]. In NMR, decoherence is captured by the term *relaxation* [1, 2, 3, 6] and two characteristic time scales are defined: T_1 which determines the return of the state to the equilibrium condition and T_2 , which accounts for phase randomization⁶. (A detailed treatise on the theory of relaxation in NMR is [69].) For all spin 1/2 nuclei, $T_2 \leq T_1$, and therefore, in a simple decoherence model, T_2 is assumed to be the limiting coherence time scale. Typically, a two qubit gate can be completed in a time proportional to $1/J$ s, so a

⁶Strictly speaking, the T_1 relaxation also contributes to the phase randomization.

rough measure of the number of (two qubit) operations that can be completed in the coherence time is $T_2/(1/J)$, a parameter we desire to maximize. I shall return to this argument in the introduction to Chapter 4. It is difficult, in general, to estimate the number of two qubit operations that can be performed before decoherence takes its toll, but a rough estimate would suggest about a thousand operations [70].

There have been several attempts [71, 72] to *model* the effects of decoherence in small NMR quantum information processors. We also used a simple model [20] to describe the decrease in signal intensity from our two qubit implementation of the Deutsch algorithm, attributable to relaxation. The experiment is explained in Chapter 4 and the model itself is outlined in Appendix ???. Interestingly, it is also possible to *reverse* the effects of unwanted system-environment interactions [73, 74] by perturbing the system, a technique called *dynamical decoupling*; or *avoiding* these interactions altogether, by working in *decoherence-free subspaces* [75]. These noiseless sub-spaces have now been experimentally realized in NMR quantum computers [76, 77].

1.1.11 Gradients

However, there are sometimes good reasons of intentionally introducing decoherence into the ensemble: as the name suggests, the *gradient* magnetic field [6, 7, 78] introduces a spatially linear magnetic field in the sample. If the gradient *strength* is G , a point in the sample at the spatial coordinate z , will experience a field of $B_0 + Gz$, instead of the otherwise homogenous field, B_0 , resulting in a position-dependent Larmor frequency,

$$\omega = -\gamma(B_0 + Gz)(1 - \sigma). \quad (1.33)$$

If we consider only the spatially dependent part, the two-qubit Hamiltonian during the gradient pulse, H_g can be written as,

$$H_g(z) = -\gamma_I Gz(1 - \sigma_I)I_z - \gamma_S Gz(1 - \sigma_S)S_z; \quad (1.34)$$

and furthermore, assuming a homonuclear system with $\sigma_I \approx \sigma_S = \sigma \approx 0$,

$$H_g(z) = -\gamma Gz(I_z + S_z), \quad (1.35)$$

and the propagator is given by,

$$U_g(z) = \exp(-iH_g(z)t) = \exp(-i\phi(z)(I_z + S_z)), \quad (1.36)$$

where $\phi(z) = -\gamma G z t$, is a space dependent phase, different points in the sample incurring different phases. Now consider a coherence term $|r\rangle\langle s|$ (an element in the density matrix), with coherence order $p = M_r - M_s$, where M_r and M_s are the magnetic quantum numbers⁷ of the states $|r\rangle$ and $|s\rangle$. The propagator transforms this coherence to,

$$\begin{aligned}
& U_g |r\rangle\langle s| U_g^\dagger \\
&= \exp(-i\phi(z)(I_z + S_z)) |r\rangle\langle s| \exp(i\phi(z)(I_z + S_z)) \\
&= \exp(-i\phi(z)M_r) \exp(i\phi(z)M_s) |r\rangle\langle s| \\
&= \exp(-i\phi(z)p) |r\rangle\langle s|,
\end{aligned} \tag{1.37}$$

indicating that the z -dependent phase also depends on the coherence order: populations and homonuclear zero quantum coherences, having $p = 0$, acquire zero phase, irrespective of the spatial position. In the post-gradient measurement, the detection coil integrates the coherences originating from across the length of the sample, and if G is sufficiently strong, (or the duration of the gradient is long enough,) the exponential terms in (1.37) will add up to zero (if $p \neq 0$). The action of an ideal, strong gradient field (also called a *crush*), is therefore to “crush” all the single and double quantum terms in the homonuclear density matrix,

$$\begin{pmatrix} \square & \square & \square & \square \\ \square & \square & \square & \square \\ \square & \square & \square & \square \\ \square & \square & \square & \square \end{pmatrix} \xrightarrow{\text{crush}} \begin{pmatrix} \square & & & \\ & \square & \square & \\ & \square & \square & \\ & & & \square \end{pmatrix}. \tag{1.38}$$

Gradients used in this way, are often called *purge* gradients [6]. I will sometimes call them *crush* sequences as well. Note that in heteronuclear systems, even the zero quantum terms will be suppressed. However, researchers have also come up with techniques for suppressing homonuclear zero quantum terms; for an example see [79]. We shall use gradient fields in different contexts through the course of this work.

1.1.12 Quantum state tomography

Quantum state tomography [8] is the process of determining a density operator ρ . A two qubit ρ has sixteen elements, and is characterized by fifteen independent param-

⁷For example, the quantum number M_r is defined by the operator equation $I_z|r\rangle = M_r|r\rangle$.

eters [80], for example, the fifteen coefficients in (1.12), and state tomography entails determining these parameters. Direct detection of ρ , gives access to only the eight direct observables, (1.22) and so, additional experiments are needed, converting the unobservable terms into observables. For example, a two qubit ρ can be characterized in four experiments; possible sets are the experiments involving,

$$\{\mathbf{1}, 90_x, 90_y, 90 I_y\}, \quad \text{and} \\ \{90 I_x, 90 I_y, 90 S_x, 90 S_y\}, \text{ etc.},$$

where $\mathbf{1}$ represents an identity operation, corresponding to direct detection. (The four-step tomography also suggests that the nine-step scheme used in [22, 23] is excessive.) In some cases, when there is some prior knowledge about the state, fewer tomography experiments may also be sufficient. One obvious method is using a crush gradient, which forces all single and double quantum coherences to the value zero. In Section 3.1, I present an example of a one-shot tomography on a state which is constrained to have only two independent parameters. Recent demonstrations of state tomography in NMR can be found in [58, 81, 82]. The reconstruction of density matrices from read-outs in an NMR experiment is exemplified in [83].

1.2 Initialization in NMR

As I have mentioned, NMR is very good at unitary operations, with fidelities approaching unity. However, its main weakness lies in non-unitary operations, namely initialization and single-spin read-out. This section discusses the problem of initialization and the following section touches upon the issue of measurement.

1.2.1 Initial states in “thermal” NMR

Consider a weakly coupled spin system. The equilibrium density matrix of an ensemble of n qubits is given by [3, 16, 17],

$$\rho_{eq} = \frac{\exp(-H/kT)}{Z}, \quad (1.39)$$

where,

$$Z = \text{Tr}(\exp(-H/kT)) \quad (1.40)$$

is the partition function and serves for normalizing the state and H is the system Hamiltonian. The operator ρ_{eq} will be diagonal in the basis of the Hamiltonian H [31], (the Zeeman basis). If q, r and s are indices for the energy levels and i is an index for the qubits, the individual matrix elements in ρ_{eq} will be given by,

$$\begin{aligned}\langle r|\rho_{eq}|s\rangle &= \langle r|\exp(-H/kT)|s\rangle \bigg/ \sum_{q=1}^{2^n} \langle q|\exp(-H/kT)|q\rangle \\ &= \delta_{rs} \exp(-E_r/kT) \bigg/ \sum_{q=1}^{2^n} \exp(-E_q/kT),\end{aligned}\quad (1.41)$$

where E_r is the energy of the r th eigenlevel (Zeeman level),

$$E_r = \hbar\omega_r \quad \text{and} \quad (1.42)$$

$$\omega_r = \sum_{i=1}^n m_i \omega_i \quad (1.43)$$

$$\overset{\text{homonuclear}}{\approx} \omega_i \sum_{i=1}^n m_i = \omega_i M_r, \quad (1.44)$$

$\omega_i = -\gamma_i B$ being the Larmor frequency of the i th qubit, and the spin magnetic quantum number [84], m_i being $1/2$ or $-1/2$ depending⁸ on whether the corresponding qubit is $|\alpha\rangle$ or $|\beta\rangle$. In writing (1.43), I assume that the coupling frequencies J (hundreds of Hz) are very small as compared to the Larmor frequencies (hundreds of MHz), and in writing (1.44), I also neglect effects of chemical shift differences between the qubits.

In (1.41), $\langle r|\rho_{eq}|r\rangle$ represents the *fractional population* in the r th level, suggesting a Boltzmann distribution of qubits in the 2^n available levels. For a homonuclear system, these levels are distributed in $n+1$ “steps”, in a Pascal’s triangle fashion. The distribution of levels and steps in the energy manifold is exemplified in Table 1.2 and illustrated for two and three qubits in Figure 1.1. The summary is that the distributions of levels in steps of a “Pascal’s ladder” is a direct result of the addition of the magnetic quantum numbers m_i . The sum of the magnetic quantum numbers, $M_r = \sum_i m_i$, can take up a value from the range, $\{n/2, n/2-1, n/2-2, \dots, -(n/2-1), -n/2\}$. The number of steps is $n+1$, and if we index the steps $k=0, 1, \dots, n$, then the number of levels in the k th step is nC_k , and the M_r of the individual levels belonging to this step is $n/2 - k$.

With this background, we can derive a product operator form for an n qubit initial state. This will also be a convenient entry into understanding the problem of initializa-

⁸Without loss of generality, I *assume* that $m = 1/2$ for the $|\alpha\rangle$ state and $-1/2$ for the $|\beta\rangle$ state. This translates into $|\alpha\rangle$ being a low energy state for positive γ nuclei such as hydrogen. In fact, understanding the signs of frequencies in NMR is a convoluted undertaking; see, for example [41].

no. of qubits	no. of levels	no. of “steps”	levels per step
1	2	2	1
2	4	3	1, 2, 1
3	8	4	1, 3, 3, 1
\vdots			
n	2^n	$n + 1$	$1, {}^nC_1, {}^nC_2, \dots, {}^nC_{n-1}, {}^nC_n$

Table 1.2: Arrangement of energy levels in the nuclear spin energy manifold for n qubit homonuclear systems, neglecting coupling interactions.

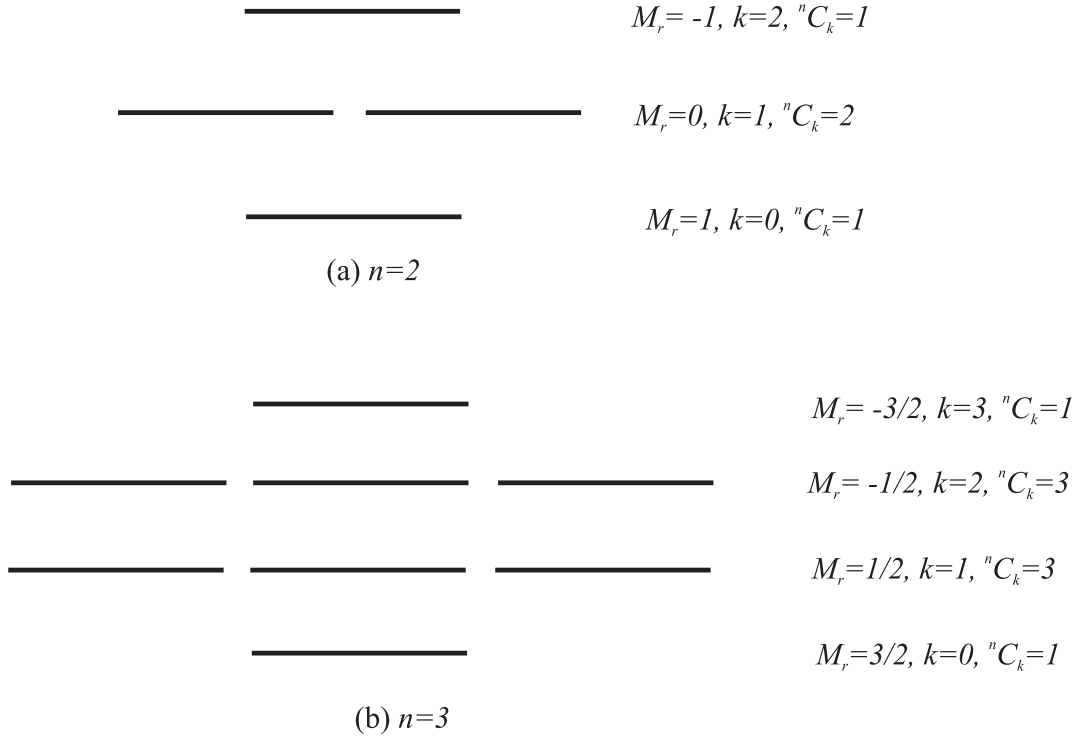


Figure 1.1: Conceptual representation of energy levels in steps on a Pascal’s ladder, and correspondence with the total magnetic quantum number M_r . Case (a) is for two qubits ($n = 2$) and case (b) represents three qubits ($n = 3$). The M_r , step index k and number of levels in each step, nC_k are written alongside the steps.

tion in NMR. Consider a single qubit $n = 1$; there are two energy levels, each level in a separate step, $|\alpha\rangle$ being lower in energy than $|\beta\rangle$. Suppose the fractional populations in these states are n_α and n_β ; from (1.41), n_α is given by,

$$\begin{aligned} n_\alpha &= \exp(-E_\alpha/kT) / \left(\sum_{q=\alpha,\beta} \exp(-E_q/kT) \right) \\ &= \exp(-\hbar\omega_\alpha/kT) / \left(\exp(-\hbar\omega_\alpha/kT) + \exp(-\hbar\omega_\beta/kT) \right), \quad (\text{from (1.42)}) \\ &= \exp(-\hbar\omega/2kT) / \left(\exp(-\hbar\omega/2kT) + \exp(\hbar\omega/2kT) \right), \quad (\text{from (1.44)}), (1.45) \end{aligned}$$

where ω is the Larmor frequency of the first and the only qubit. In the high temperature limit, $kT \gg \hbar\omega$, n_α is approximated as,

$$\begin{aligned} n_\alpha &\approx (1 - \hbar\omega/2kT) / (1 - \hbar\omega/2kT + 1 + \hbar\omega/2kT) \\ &= (1 - \hbar\omega/2kT) / 2, \end{aligned} \quad (1.46)$$

and similarly,

$$n_\beta \approx (1 + \hbar\omega/2kT) / 2. \quad (1.47)$$

With these fractional populations, the equilibrium state can be written as,

$$\begin{aligned} \rho_{eq} &= \{ \{ n_\alpha, n_\beta \} \} \\ &= \frac{1}{2} \begin{pmatrix} 1 - \hbar\omega/2kT & 0 \\ 0 & 1 + \hbar\omega/2kT \end{pmatrix} \\ &= \frac{1}{2} (\mathbf{1}_2 - \mathcal{B}I_z) \sim I_z, \end{aligned} \quad (1.48)$$

where $\mathcal{B} = \hbar\omega/kT$ is what I refer to as the *Boltzmann factor*. Similarly, for two homonuclear qubits, the equilibrium state is

$$\frac{1}{4} (\mathbf{1}_4 - \mathcal{B}(I_z + S_z)) \sim I_z + S_z, \quad (1.49)$$

and for n qubits,

$$\frac{1}{N} (\mathbf{1}_N - \mathcal{B}(\sum_{i=1}^n I_{iz})) \sim \sum_{i=1}^n I_{iz}. \quad (1.50)$$

For a proton frequency of 400 MHz, the high temperature approximation will be valid for $T \gg 0.02$ K, indicating that the equilibrium states (1.50) are an extremely good description at temperatures of even a few hundred millikelvins, and therefore, must also accurately describe our initial states at room temperature. I shall refer to these high temperature equilibrium states as *thermal* states in the remainder of this thesis.

Now some important comments on the energy gaps and population differences between levels, which are significant because the NMR signal arises from *differences* in level populations. The ball-park figures derived in the following discussion all assume a proton frequency of 400 MHz and a temperature of 295 K. The *Zeeman splitting* defined as the energy gap between levels in adjacent steps, is always $\hbar\omega$, resulting in the steps being evenly spaced. This splitting is extremely small, a tiny 2.6×10^{-25} J, and the available thermal energy $kT \approx 4 \times 10^{-21}$ J is four orders of magnitude larger, resulting in *almost* equal populations between the levels. Another way of stating this is that \mathcal{B} is exceedingly small: about 6.5×10^{-5} . However, the populations in the adjacent levels are not *exactly* identical, otherwise thermal NMR would not have been possible in the first place. In fact, the fractional population difference between adjacent levels is proportional to \mathcal{B} . For example, in a single qubit, the difference is $\mathcal{B}/2 \approx 3.2 \times 10^{-5}$: which means that for roughly every 3×10^4 spins, there will be one extra spin in the lower $|\alpha\rangle$ level and if the sample contains 10^{15} spins, the net excess of spins will be of the order of 10^{10} ; not a very large number, keeping in view the very small magnetic moment of the nucleus. For all other nuclei (except radioactive tritium, $^3\text{H}_1$), the Zeeman splitting is even smaller.

1.2.2 Pseudopure initial states

The foregoing discussion explains the origins of the notoriously low sensitivity of NMR arising from the tiny Zeeman splittings: small gaps lead to small population differences which in turn lead to small signals. The insensitivity is a problem in analytical NMR, especially if the concentration of the sample is small. A lot of effort, therefore, is devoted to attaining increased polarization or hyperpolarization and some techniques for achieving this will be touched upon in Section 1.5. However, in the context of quantum information processing, the low magnetic to thermal energy ratio is also a limiting factor in a slightly different way and I now outline this limitation.

Every computational process must start off by placing the computational register in a well-defined initial state; for a quantum computer, we normally expect the (register of) qubits to be placed in the energetically ground state $|\mathbf{0}\rangle = |00\dots 0\rangle = |\alpha\alpha\dots\alpha\rangle$, a

pure quantum state. For example, for two qubits, a suitable initial state would be,

$$\begin{aligned}\{\{1, 0, 0, 0\}\} &= \frac{\mathbf{1}_4}{4} + \frac{I_z + S_z + 2I_z S_z}{2} \\ &\sim I_z + S_z + 2I_z S_z,\end{aligned}\tag{1.51}$$

having only one non-zero eigenvalue. What nature furnishes instead is the thermal state, $(1.49) \sim I_z + S_z = \{\{1, 0, 0, -1\}\}$, having two non-zero eigenvalues. We immediately encounter two problems: *first*, the thermal and desired initial states are not identical and *second*, the amount of the (deviation) thermal state is proportional to a very small number, \mathcal{B} . How do we then prepare a pure initial state, suitable for quantum computing? The answer was provided by Cory *et al.*, [17, 85], who suggested that it is *not* necessary to prepare pure states, rather it is sufficient to prepare only *pseudopure* states, that are given by the general form,

$$\rho_{ps} = (1 - \varepsilon) \frac{\mathbf{1}_N}{N} + \varepsilon |\psi\rangle_p \langle \psi|_p,\tag{1.52}$$

the subscript “*ps*” and “*p*” indicating pseudopure and pure states. For a two qubit system, a conventional pseudopure state is,

$$\rho_{ps} = (1 - \varepsilon) \frac{\mathbf{1}_4}{4} + \varepsilon |00\rangle \langle 00|,\tag{1.53}$$

comprising ε parts of the desired pure state mixed with $1 - \varepsilon$ parts of the maximally mixed state. This factor, ε , is what I term the *polarization*, signifying the amount of “polarized” pure component in the overall state, the maximally mixed (unpolarized) state being NMR silent. The dynamics of ρ_{ps} are exactly identical to $|00\rangle \langle 00|$, and so the pseudopure state effectively behaves as a pure state, albeit with smaller polarization and hence lower sensitivity.

How do we prepare these effective pure states? The eigenvalue spectra for the thermal and pure states are different, and so some kind of non-unitary operation is required [31, 86]: as a result, the different approaches for assembling pseudopure states all involve some kind of non-unitary averaging of eigenvalues. At the end of the averaging process, we are left with one *non-degenerate* eigenvalue. (A pure state has one *non-zero* eigenvalue.)

The different strategies for pseudopure state generation are reviewed in [15, 19]. In summary, the earliest proposals [17, 85], called *spatial averaging*, employed field gradients, whereby the averaging is achieved by entangling the spin degrees of freedom

with spatial dimensions and later taking a partial trace over space. Another approach [87, 88], called *temporal averaging*, performs the averaging by carrying out multiple experiments, each experiment using a different initial state unitarily derived from the thermal state. This second approach, in a sense, entangles the spin degrees of freedom with time and throws away the time information at the end. A third scheme [89, 90], called *logical labelling*, selects a subset of qubits embedded in a higher dimensional quantum space, conditioned upon the state of the unselected qubits. This last approach is elegant in principle, but the complexity of the pulse sequences has limited its applicability to small homonuclear systems. There is yet another efficient strategy [91] for “extracting” an $n - 1$ qubit pseudopure state from n -multiple quantum coherence terms (related to “cat” states [8]) which are selected using filtration sequences based on the use of gradients or phase cycling [3].

1.2.3 Climbing “Mount Scalable”?

A large part of this thesis concerns the preparation of a two qubit NMR based quantum computer, so what method do we use to prepare pseudopure states? The answer is, simply, we do not prepare pseudopure states, instead our system is directly initialized in an almost pure state. A part of the very first DiVincenzo requirement [11] is scalability and the pseudopure strategy does not satisfy this requirement, as I now review. Most of the following criticism was anticipated in Warren’s paper [92] and more comprehensive reviews on the scalability issue can be found in [70, 93], the latter reference being the source of the term “Mount Scalable”.

Warren derived an upper bound on the polarization factor for a pseudopure state in a homonuclear system, which I call the *Warren bound*. The derivation is based on the fact that the theoretical maximum polarization achievable from a thermal state is upper bounded by the maximum fractional population difference in an n qubit system: the maximum difference is between the $|\alpha\alpha\dots\alpha\rangle$ and $|\beta\beta\dots\beta\rangle$ states, which are the furthest apart in energy. These “all α ” and “all β ” states have magnetic quantum numbers $n/2$ and $-n/2$, and using (1.41)–(1.44), the corresponding difference⁹ can be

⁹This difference enables excitation of the multiple quantum coherence of order n [4]. In reference [92], the expression (1.54) does not carry the negative sign, however, this sign is consistent with our assumption that for positive γ (and negative ω) nuclei, $|\alpha\rangle$ is the lower energy state, resulting in $n_{\text{all } \alpha} > n_{\text{all } \beta}$.

derived as,

$$\begin{aligned} n_{\text{all } \alpha} - n_{\text{all } \beta} &= (\exp(-n\hbar\omega/2kT) - \exp(n\hbar\omega/2kT))/Z \\ &= -2 \sinh(n\hbar\omega/2kT)/Z. \end{aligned} \quad (1.54)$$

The partition function Z can be written in compact form as the Binomial expansion,

$$\begin{aligned} Z &= \sum_{k=0}^n {}^nC_k (\exp(-\hbar\omega/2kT))^{n-k} (\exp(\hbar\omega/2kT))^k \\ &= (\exp(-\hbar\omega/2kT) + \exp(\hbar\omega/2kT))^n \\ &= 2^n \cosh^n(\hbar\omega/2kT), \end{aligned} \quad (1.55)$$

and therefore, Warren's bound is given by,

$$(n_{\text{all } \alpha} - n_{\text{all } \beta})/Z = -2 \sinh(n\hbar\omega/2kT)/(2^n \cosh^n(\hbar\omega/2kT)), \quad (1.56)$$

which in the limit of high temperature and ignoring the negative sign, is,

$$\frac{n}{2^n}(\hbar\omega/kT) = \frac{n}{2^n}\mathcal{B}, \quad (1.57)$$

where I have used the limiting values of the hyperbolic functions, $\lim_{x \rightarrow 0} \sinh x = x$ and $\lim_{x \rightarrow 0} \cosh x = 1$.

The exact polarization extracted from the the thermal state, depends on the method used to prepare the pseudopure state, however in all cases, the Warren bound (1.57) sets an upper limit. In the high temperature limit, the bound results in an exponential decrease in polarization as we linearly increase the number of qubits; and therefore to defeat the exponential loss in sensitivity, exponentially more resources are required, such as exponentially larger samples. This is not only impractical but also defeats the fundamental gain expected (and desired) from a quantum computer, that is exponentially bigger Hilbert dimensionality with at the most, polynomial resources. It appears that thermal NMR based on assembling pseudopure states is not scalable and this statement is the gist of the initialization problem.

1.2.4 Concentrating polarization

However, the literature suggests that the problem of low polarization and scalability can be sidestepped, using a computational (technology independent) approach outlined

by Schulman and Vazirani [94]. The method centres around polarization *concentration*: given an ensemble of n weakly polarized qubits, it is possible to extract $k < n$ hyperpolarized qubits, at the expense of maximally randomizing the remaining $n - k$ qubits. The scheme for extracting pure qubits can be represented as,

$$\bigotimes_n \left((1 - \varepsilon) \frac{\mathbf{1}_2}{2} + \varepsilon |0\rangle\langle 0| \right) \xrightarrow{\text{S. V.}} \left(\bigotimes_k |0\rangle\langle 0| \right) \otimes \left(\bigotimes_{n-k} \frac{\mathbf{1}_2}{2} \right), \quad (1.58)$$

\bigotimes_j denoting the tensor product between j qubits. The algorithm operates on classical states and conserves the classical entropy S [8] of the system. From this condition, an upper limit on the number of pure qubits extracted can be determined: the entropy of a single qubit with polarization ε (and fractional populations $(1 \pm \varepsilon)/2$) is

$$S(\varepsilon) = -\left(\frac{1+\varepsilon}{2}\right) \lg_2\left(\frac{1+\varepsilon}{2}\right) - \left(\frac{1-\varepsilon}{2}\right) \lg_2\left(\frac{1-\varepsilon}{2}\right), \quad (1.59)$$

and as the entropy is conserved, we can write,

$$nS(\varepsilon) = kS(1) + (n - k)S(0) \quad (1.60)$$

$$= k(0) + (n - k)(1)$$

$$\begin{aligned} \implies k &= n(1 - S(\varepsilon)) \\ &= n\left(1 + \left(\frac{1+\varepsilon}{2}\right) \lg_2\left(\frac{1+\varepsilon}{2}\right) + \left(\frac{1-\varepsilon}{2}\right) \lg_2\left(\frac{1-\varepsilon}{2}\right)\right), \end{aligned} \quad (1.61)$$

$$(1.62)$$

and using the expansion $\lg_2(1 \pm x)/2 = -1 \pm x/\ln 2 - x^2/(2 \ln 2) \pm \mathcal{O}(x^3)$ for small x ,

$$k \approx \frac{n\varepsilon^2}{2 \ln 2} \approx n\varepsilon^2 \quad (\text{for large } n). \quad (1.63)$$

The equation indicates that we can extract k pure qubits from k/ε^2 low-bias qubits; the scaling is only linear in k . This may seem to be an exciting possibility for NMR but taking a more practical point of view, the restrictively small values of $\varepsilon \approx 10^{-5}$ in thermal NMR, require a prohibitively large ($\approx 10^{10}$) number of initial qubits, even to extract a single pure qubit. However, despite this limitation, an NMR demonstration of the basic building block in the polarization boosting has already been demonstrated [95].

Another variant of the above technique is the so-called *algorithmic cooling* method [96] which is an entropy non-conserving algorithm for polarization concentration. The method beats the Shannon bound (1.60) through the use of rapidly relaxing qubits in an

open quantum system and an initial implementation of this non-adiabatic version has also been reported [97]. However, it seems that both of these computational schemes will become practically useful in small sized spin systems, only when used in conjunction with higher initial polarizations.

1.2.5 Re-initialization

Quantum error correction [98, 99] is an attempt to counteract the effects of decoherence, reversing errors once they have occurred. Thermal NMR is not well suited for this purpose, because of two major reasons: *first*, most error detection and correction schemes work by encoding a physical qubit in several logical qubits, the increased number of qubits reducing the sensitivity; and *second*, repeated error correction requires one to reuse the ancillary qubits and currently, no practical schemes are known for resetting NMR qubits into pure states at will. Thermal NMR cannot realize pure states *initially*, let alone provide a *continuous* supply of pure qubits *during* the experiment and so, even though, simple error detection [100] and correction [101] have now been implemented in small NMR systems, they mostly remain proof of principle experiments.

1.3 Measurement in NMR

Liquid state NMR does not implement projective measurements [8] on single qubits. A projective (“strong”) measurement on a qubit in the state $(c_0|0\rangle + c_1|1\rangle)(c_0^*\langle 0| + c_1^*\langle 1|)$, yields $|0\rangle$ with probability $|c_0|^2$ and $|1\rangle$ with probability $|c_1|^2$, leaving the state in $|0\rangle\langle 0|$ or $|1\rangle\langle 1|$, also showing that such measurements constitute one (though not the only) way of initializing the qubit. In liquid state NMR, we do not have access to single qubits but rather ensembles of qubits, and the so-called “weak” measurements performed in these systems provide ensemble averages [17]: the final result is a noisy expectation value of a spin operator, such as $\langle I_x \rangle$ or $\langle I_y \rangle$, taken over *all* molecules in the sensitive region of the detection coil. Furthermore, the wavefunction does not collapse into one post-measurement state as the system is only feebly affected by the detection process [41, 102]. In short, it appears that these weak measurements are statistically equivalent to standard, single-qubit measurements, and will suffice, until we make enough progress to start actively considering resetting qubits for quantum error correction.

It is not out of place to comment upon a few research initiatives aimed at single-spin or single-molecule detection. Single sub-atomic particles have small magnetic moments [31] and are difficult to measure in normal circumstances. There has, however, been recent progress in detection of single electron spins using the spin-dependent magnetic force on a ferromagnetic tip [103] and spin-dependent charge transport [104]. Direct spin detection of protons and nuclear spins is even more difficult, as their gyromagnetic ratios are much smaller. The detection of single nuclear spins, therefore, requires some kind of “amplification” of nuclear Zeeman splittings by correlating them with the wider energy gaps present in another degree of freedom. For example, in the first optically-detected magnetic resonance experiments [105, 106], the magnetic transitions (microwave) in the electronic spectrum of a *single molecule* were indirectly detected as optical transitions, which are intense and can be monitored with much higher quantum efficiencies. Another interesting experiment in this regard is the optical detection of nuclear magnetic transitions in a single quantum well [107]. It is widely felt that any envisaged single-nuclear spin detection scheme is likely to involve detection of optical photons.

I have now discussed liquid state NMR in terms of the DiVincenzo criteria. There remains another important and more fundamental aspect of thermal NMR that has even raised questions about its acceptance as a truly “quantum” process. In the next section, I take up the widely debated issue of entanglement in liquid state NMR.

1.4 Entanglement in NMR

Entanglement [8] is undoubtedly an important resource in quantum information processing; some researchers would argue that it is *the* “characteristic trait of quantum mechanics” [108]. Entanglement is interesting because it enables quantum states to exhibit correlations that have no classical analog. Of its many example applications in quantum information science, entanglement enables quantum teleportation [109, 110], superdense coding [111, 112] and secure communication [113, 114].

A bipartite pure state will be entangled if its Schmidt number is greater than one [8] and a mixed state of two or more qubits will be entangled if it cannot be written as the convex sum of the direct products of the component density operators (Section 1.4.1). Several operational criteria for detecting and quantifying entanglement will be

taken up in the following subsections.

As an example of the consequences of entanglement, consider the maximally entangled state,

$$|\phi^+\rangle = \frac{1}{\sqrt{2}}(|01\rangle + |10\rangle). \quad (1.64)$$

Tracing out the second qubit, the reduced density matrix [8] of the first qubit will be the maximally mixed state, $\rho_A = 1/2 \{\{1, 1\}\}$, implying that measuring this qubit along any axis would result in a random result, and thus measuring one subsystem *alone* provides no information about the preparation of the composite state, (1.64). In this sense, the entangled state contains “hidden information” which cannot be revealed by measurements on either qubit. However, if both subsystems are measured and the results are compared, they will be perfectly correlated.

Conventional NMR based QIP uses highly mixed, separable (non-entangled) states. In this section we explore the relations between entanglement and the purported power of quantum computers, more specifically, NMR quantum computers. For example, can NMR devices exhibit entanglement? And are current devices truly quantum? In fact, most of the work in the current thesis addresses the two-fold problem of initialization and entanglement. Subsequent chapters will discuss in detail, our experimental implementations, of *initializing* a two qubit system in an *entangled* state. A gentle introduction to the role of entanglement in NMR can also be found in [115].

1.4.1 Separable and entangled states

Traditional QIP experiments using liquid state NMR furnish and employ separable states. A two qubit pure state will be separable if it can be written as a tensor product [8, 31] of the component pure states,

$$|\chi\rangle_{AB} = |\psi\rangle_A \otimes |\phi\rangle_B, \quad (1.65)$$

where A and B label the qubits. Examples of separable states include $|00\rangle = |0\rangle \otimes |0\rangle$ and $(|01\rangle + |11\rangle)/\sqrt{2} = ((|0\rangle + |1\rangle)/\sqrt{2}) \otimes |1\rangle$. A pure state is non-separable, or entangled, if it cannot be brought into the form (1.65); examples are the Bell states [8], defined as,

$$|\phi^\pm\rangle = (|00\rangle \pm |11\rangle)/\sqrt{2} \quad (1.66)$$

$$|\psi^\pm\rangle = (|01\rangle \pm |10\rangle)/\sqrt{2}. \quad (1.67)$$

However, as pointed out earlier, states encountered in traditional NMR are mixed and have exceedingly small polarizations. Separability for such mixed states is, at least, *well-defined*: a two qubit mixed state ρ will be separable if it can be decomposed as a weighted sum of *product* states,

$$\rho = \sum_i p_i (\rho_A \otimes \rho_B)_i, \quad \text{with } p_i \geq 0 \text{ and } \sum_i p_i = 1. \quad (1.68)$$

The product state $(\rho_A \otimes \rho_B)_i$, prepended with a non-negative classical probability p_i , has the property that the A and B quantum sub-systems are independent: knowledge of one sub-system does not depend on or affect the other sub-system. Product states are not entangled; and neither are their convex combinations, such as (1.68). All states in low-polarization NMR can be written in the form (1.68), and are therefore, always separable.

A state we shall frequently encounter in this work is the Werner state [116]. For two qubits the state is given by,

$$\rho_\varepsilon = (1 - \varepsilon) \frac{\mathbf{1}_4}{4} + \varepsilon |\psi_{ent}\rangle \langle \psi_{ent}|, \quad (1.69)$$

where $|\psi_{ent}\rangle$ is one of the four maximally entangled Bell states, (1.66) and (1.67). Whether ρ_ε is entangled or not, depends on the precise value of ε , and is investigated in Section 1.4.4. The headline result is that the Werner state (1.69) will be entangled when $\varepsilon > 1/3$.

1.4.2 Separability bounds for mixed states in NMR

Until now, I have defined separability and given examples of two qubit entangled states. Can we also come up with general separability tests for n qubit states, where $n \geq 2$? This question is important in understanding the scalability characteristics of quantum computers, and in context of NMR, was first addressed by Braunstein *et al.* [117]. The major results of their work and some interesting observations are summarized in this section¹⁰. A general method¹¹ for deriving the lower bound and constructing explicit decompositions of separable states can also be found in [120].

¹⁰It should be noted that since Braunstein's original work, tighter bounds have been proposed [118, 119]. These new bounds modify the finer details, but do not affect the overall broad results.

¹¹The method is based on decomposing a density operator in an over-complete basis, and based on the constraints on the operator eigenvalues, looking for conditions that guarantee non-negative probabilities in (1.68).

NMR deals with highly mixed states. The maximally mixed state $M_n = \mathbf{1}/2^n$ is clearly separable, as are states lying sufficiently close to M_n . Braunstein and co-workers determined [117] lower and upper bounds on the size of the separable neighbourhoods of M_n , for arbitrary n . The concept is illustrated in Figure 1.2, indicating that the bounds result in three distinct regions: **S**, where all states are provably separable, **E**, where entanglement can definitely exist, or in other words, where the states are unitarily equivalent [121] to entangled states, and a region in between, **ES**, where it is not clear whether entangled states can or cannot exist. Consider the n qubit state, with a “distance” ε from M_n ,

$$\rho = (1 - \varepsilon)M_n + \varepsilon\rho_1, \quad (1.70)$$

ρ_1 being an arbitrary density matrix. For sufficiently small ε ,

$$\varepsilon \leq \varepsilon_l = \frac{1}{1 + 2^{2n-1}} \stackrel{\text{large } n}{\approx} \frac{2}{4^n}, \quad (1.71)$$

ρ lies in the region S . Similarly, for sufficiently large values¹² of ε ,

$$\varepsilon > \varepsilon_u = \frac{1}{1 + 2^{n/2}} \stackrel{\text{large } n}{\approx} \frac{1}{2^{n/2}}, \quad (1.72)$$

entangled states *can* exist. These bounds are shown in Figure 1.3.

Some important observations emerging from the Braunstein and Warren bounds are the following.

1. As the number of qubits increases, the size of **S** shrinks, increasing the *likelihood* of entanglement, even for reasonably small values of ε .
2. For a typical value of $\mathcal{B} \approx 10^{-5}$, and the modest number of qubits presently employed in NMR quantum computers, (the current record is at seven qubits [20],) all states lie in the region **S**. This has lead to interesting discussions raising suspicions about the very nature of liquid state NMR as a truly “quantum”, computing paradigm.
3. Fixing \mathcal{B} , we can estimate the number of qubits at which the **S** to **ES** cross-over will take place. For $\mathcal{B} = 10^{-5}$, this transition would occur with fourteen qubits.

¹²The upper bound is determined by projecting an arbitrary 2^d dimensional state of two *qudits* onto a four dimensional Werner state of two *qubits*, and using Werner’s separability criterion [122] to estimate the threshold.

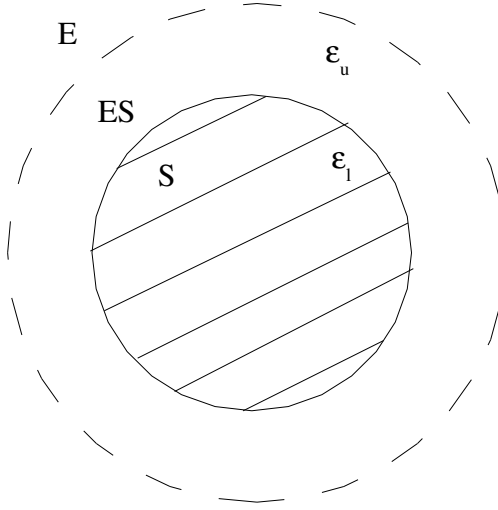


Figure 1.2: Lower ε_l and upper ε_u bounds as constructed by Braunstein and co-workers [117]. The regions **S**, **E** and **ES** indicate the existence of definitely separable, definitely entangled and “maybe-entangled” states. The maximally mixed M_n lives in the middle of **S**. The continuous **S-ES** boundary belongs to **S**, and the dashed **ES-E** boundary belongs to **ES**.

4. If instead of fixing \mathcal{B} , we choose to fix n at seven qubits, then \mathcal{B} should be at least 0.002 for the transition into **ES**. On modern high-field spectrometers, this translates into a maximum temperature of about 10 K; most liquid samples would be frozen at this temperature.
5. Figure 1.3 also suggests that with low polarization NMR, it will never be possible to cross over into the provably entangled region **E**: a radically different approach is therefore needed to realize entanglement in liquid state NMR.

1.4.3 (Quantum) nature of liquid state NMR (quantum) information processing

The above findings have led to considerable concern about the *nature* of liquid state NMR: the statistics of experimental outcomes from separable states can be described perfectly well using classical probability distributions, and therefore, in its very essence, liquid state NMR may not be quantum at all [123]! This might seem to be the end of the story for liquid state NMR *quantum* computing, but luckily, the details are much subtler.

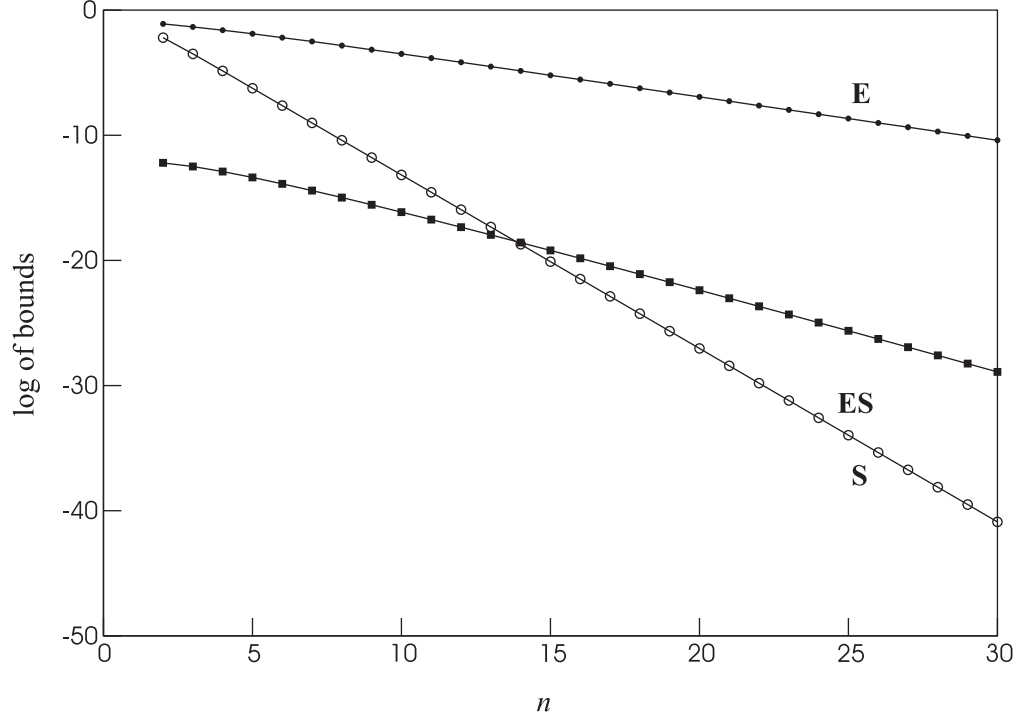


Figure 1.3: Lower (ε_l) and upper (ε_u) separability and Warren bounds as a function of the number of qubits n . The ordinate scale is logarithmic. The line with the open circles indicates ε_l , the **S-ES** boundary and the one with filled circles represents ε_u , separating **ES** and **E**. The line identified with squares is the Warren bound, plotted assuming $\mathcal{B} = 10^{-5}$.

To start with, there are differing “definitional” stances on the “quantumness” of liquid state NMR, views revolving around the question of whether entangled states are a *prima facie* signature of quantum behaviour, or if the real quantum character lies in quantum mechanical dynamics, or possibly somewhere else. No doubt, the quantum states are separable, but what about the dynamics? Can quantum information also “reside” in states that are not entangled, as discussed in the context of quantum discord [124]? Finally, can we come up with efficient classical models to simulate the *dynamics* of separable states?

In short, the role of entanglement in quantum computing *per se*, remains an open question [115, 125]. At the one end, entanglement has been viewed as the source of the enhanced information processing capabilities of quantum computers, a view resonating in [126]. But at the same time, liquid state NMR (quantum) information processors routinely implement quantum dynamics governed by the Liouville-von Neumann Equation [2], even though they do not exhibit entangled states. Having said this, we must also remember that efficiency arguments must be analyzed in light of the fact that the enhanced power of quantum computers is only an assumption, although a very tempting one, and except for the black box or oracle case, there is no proof as yet of the increased power of quantum processors. Second, quantum algorithms outperform only the best *known* classical algorithms. For example, in the case of the factoring problem, one day somebody might also come up with a classical algorithm for efficient factoring [127]. In this case, most of our fundamental perspectives on quantum information processing would be subject to major change anyway. In light of this discussion, we can safely conclude, that the essential nature of high temperature liquid state NMR is an open-ended question, and is intertwined with the *supposed* role of entanglement in conferring *arguably* better information processing capabilities to quantum computers.

The present work, however, by-passes this interesting discussion by preparing *de facto* entangled states; the first demonstration of entanglement in liquid state NMR. As a result, most of the charges made against the very nature of liquid state NMR implementations can no longer be directed against our two qubit quantum computer.

1.4.4 Detecting entanglement in two qubit states

One of the main claims made in the forthcoming chapters is that we achieve entangled states in liquid state NMR. In this respect, one might ask the following questions. How can entanglement be *detected* in our two qubit system? Finally, can we go one step beyond detection, and actually *quantify* the amount of entanglement? This section deals with these questions. Useful primers on the subject of detecting and quantifying entanglement are the references [128, 129].

Positivity of partial transpose

For a two qubit state, entanglement can be detected, for example, through the so-called positivity of partial transpose (PPT) test, first proposed and exemplified in [122]. Consider the separable mixed state (1.68). Taking the transpose of the reduced density matrix [31], ρ_A , results in an overall state,

$$\rho^{TA} = \sum_i p_i (\rho_A^T \otimes \rho_B)_i, \quad \text{with } p_i \geq 0 \text{ and } \sum_i p_i = 1, \quad (1.73)$$

where T denotes the transpose operation. As the reduced matrix ρ_A is hermitian (being a valid density operator [8]), $\rho_A^T = \rho_A^*$ is also an hermitian, unit trace matrix and hence another legitimate density operator. This, in turn, implies that the state ρ^{TA} is also a valid density operator and has non-negative eigenvalues. The PPT test, therefore, detects non-separability by searching for negative numbers in the eigenvalue spectrum of the partial transpose¹³ of ρ .

The PPT is a simple operational test and I illustrate it with a relevant example. Consider the Werner state,

$$\rho_\varepsilon = (1 - \varepsilon) \frac{\mathbf{1}_4}{4} + \varepsilon |\psi^-\rangle \langle \psi^-| \quad (1.74)$$

$$= \begin{pmatrix} \frac{1-\varepsilon}{4} & 0 & 0 & 0 \\ 0 & \frac{1+\varepsilon}{4} & -\frac{\varepsilon}{2} & 0 \\ 0 & -\frac{\varepsilon}{2} & \frac{1+\varepsilon}{4} & 0 \\ 0 & 0 & 0 & \frac{1-\varepsilon}{4} \end{pmatrix}, \quad (1.75)$$

¹³It is equally valid to find ρ^{TB} instead of ρ^{TA} .

and taking the partial transpose with respect to the first qubit,

$$\rho^{T_A} = \begin{pmatrix} \frac{1-\varepsilon}{4} & 0 & 0 & -\frac{\varepsilon}{2} \\ 0 & \frac{1+\varepsilon}{4} & 0 & 0 \\ 0 & 0 & \frac{1+\varepsilon}{4} & 0 \\ -\frac{\varepsilon}{2} & 0 & 0 & \frac{1-\varepsilon}{4} \end{pmatrix}, \quad (1.76)$$

we obtain an eigenvalue spectrum, $\{(1 + \varepsilon)/4, (1 + \varepsilon)/4, (1 + \varepsilon)/4, (1 - 3\varepsilon)/4\}$. For legitimate values of ε , the first three eigenvalues are always positive, whereas the fourth eigenvalue will be non-negative only if $\varepsilon \leq 1/3$. This immediately suggests that an inseparable or entangled ρ_ε will always have $\varepsilon > 1/3$. In fact, the $1/3$ threshold can also be deduced by setting $n = 2$ in Braunstein's upper bound, (1.72). Horodecki, Horodecki and Horodecki went on to show [130] that the positivity of the partial transpose is not only a necessary, but also a sufficient requirement for separability of systems of dimensions 2×2 and 2×3 , but the result cannot be extended to higher dimensional systems. (For example, there exist [131] entangled states which satisfy the PPT test; such states are called *bound* entangled states, and are undistillable [132].) Multi-partite entanglement, is in fact, an open theoretical challenge in present-day quantum information science, and many general results are still unknown or are being investigated (for example, see [133]). However, for two qubits (a 2×2 system), the situation is rosier, and luckily, we shall be primarily concerned with two qubit (four dimensional) quantum systems in *most* parts of this thesis.

1.4.5 Quantifying entanglement in two qubit systems

As indicated earlier, *qualifying* entanglement is an arduous task, especially for higher dimensional mixed systems. How can we expect the *quantification* to be any easier? Several conditions for a “good” entanglement measure have been compiled [8, 129, 134], and there do exist a range of measures, satisfying some or all of these conditions. Once again, for two qubit systems, the situation is relatively simple and well understood.

Concurrence and entanglement of formation

According to the PPT criterion, negative eigenvalues of ρ^{T_A} are a signature of entanglement; the negativity of the most negative eigenvalue is one straightforward measure. However, for another entanglement measure, called the entanglement of formation

(EOF) [135], there also exists a closed form mathematical expression [136] (in the case of two qubits). We denote this quantity as E_f , and is our measure of choice for detecting and quantifying entanglement: a non-zero E_f indicating the existence of entangled states. A prescription for finding E_f [136] for a state ρ is outlined below.

1. Determine the “spin-flipped” operator, $\tilde{\rho} = (\sigma_y \otimes \sigma_y) \rho^* (\sigma_y \otimes \sigma_y)$, where ρ^* is the complex conjugate of ρ .
2. Find the non-Hermitian operator, $\rho' = \rho \tilde{\rho}$.
3. Compute the positive square roots of the eigenvalues of ρ' and sort them in decreasing order, $\{\lambda_1, \lambda_2, \lambda_3, \lambda_4\}$.
4. Find the concurrence defined as $C = \text{maximum}(0, \lambda_1 - \lambda_2 - \lambda_3 - \lambda_4)$.
5. The value of C is then used to calculate the value of

$$x = \frac{1}{2}(1 + \sqrt{1 - C^2}). \quad (1.77)$$

6. We then use x to calculate the entanglement of formation, through the formula,

$$E = -x \lg_2 x - (1 - x) \lg_2 (1 - x), \quad (1.78)$$

reminding us of the classical binary entropy [8] function. Note that in computing (1.78), we use the convention $0 \lg_2 0 \equiv 0$.

The concurrence and entanglement of formation E_f , can both be used as legitimate measures of entanglement. Both measures are zero for a separable state and non-zero for entangled states. For maximally entangled states, E_f is 1 and C is 1. Furthermore, E_f is a monotonically increasing convex function of C [136], the functional dependence is shown in Figure 1.4.

1.4.6 Entanglement in singlet-triplet mixtures

In this section, I determine E_f for a special class of two qubit density matrices: mixtures involving four states $|\psi^-\rangle\langle\psi^-| \equiv S_0$, $|\psi^+\rangle\langle\psi^+| \equiv T_0$, $|00\rangle\langle 00| \equiv T_1$ and $|11\rangle\langle 11| \equiv T_{-1}$. The first two (S_0 and T_0) are the Bell states (1.67) and the other two (T_1 and T_{-1}) are separable states. S_0 is conventionally called the singlet and $T_0, T_{\pm 1}$, the triplets. I also define T_m as,

$$T_m = \frac{1}{2}(T_1 + T_{-1}), \quad (1.79)$$

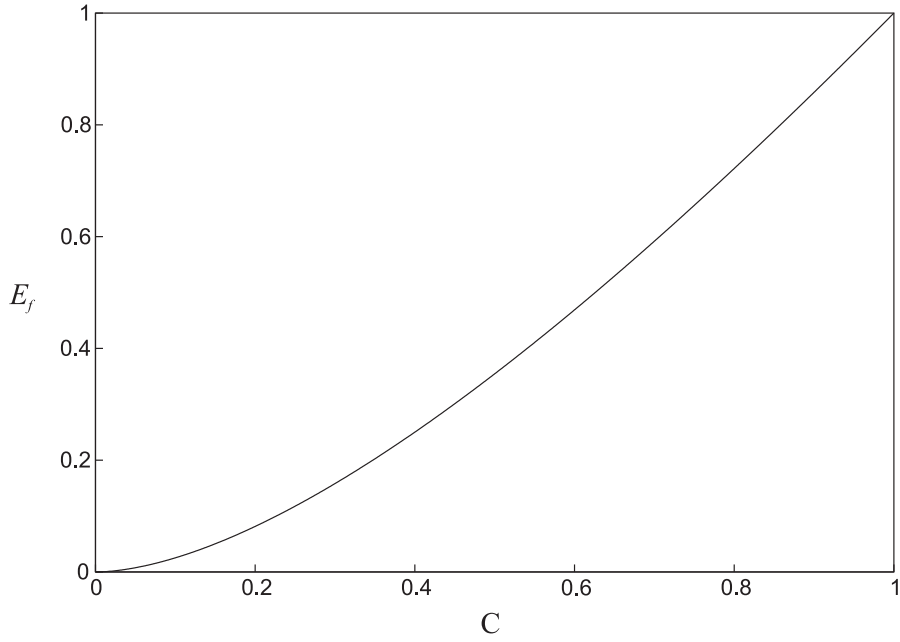


Figure 1.4: The entanglement of formation E_f as a function of concurrence C .

and observe that T_m is also an equal mixture of the Bell states $|\phi^+\rangle\langle\phi^+|$ and $|\phi^-\rangle\langle\phi^-|$.

These S/T mixtures have a special place in the present work, as our initialization experiment, to be discussed in Chapter 3, prepares states containing combinations of only S_0 , T_0 and T_m . The ideal experiment prepares S_0 , but the triplets mix in, in varying proportions, resulting in an S/T mixture. Whether the resulting mixture is entangled or not, depends on what is mixed in and in what amounts. Based on E_f measurements, we can outline some important results. These results are helpful in determining the correct threshold for entanglement.

1. The E_f for the pure S_0 is obviously 1.
2. Now consider the “binary” S_0/T_0 mixture, $\varepsilon S_0 + (1 - \varepsilon)T_0$, where $\varepsilon \leq 1$. The resulting E_f as a function of the amount of singlet, ε , is shown in Figure 1.5(a), showing that E_f is always non-zero, except when the the amounts of S_0 and T_0 are perfectly balanced, *i.e.*, when $\varepsilon = 1/2$. Interestingly, adding an entangled state (T_0) to another entangled state (S_0) reduces the overall amount of entanglement. This can also be seen in light of the convexity property [129] of the entanglement of formation,

$$E_f(\varepsilon S_0 + (1 - \varepsilon)T_0) \leq \varepsilon E_f(S_0) + (1 - \varepsilon)E_f(T_0), \quad \text{for } \varepsilon \leq 1. \quad (1.80)$$

The take-home lesson is that the S_0/T_0 mixture will *always* be entangled if $\varepsilon > 1/2$.

3. Figure 1.5(b) shows the E_f for an S_0/T_1 mixture: like the case for T_0 , adding T_1 also reduces the entanglement but it is not as effective in “pushing” the state to the separable region, and the mixture is entangled for $\varepsilon > 0$.
4. If we mix in T_m , the state is entangled for $\varepsilon > 1/2$; the E_f is plotted in Figure 1.5(c). This indicates that T_m , a balanced mixture of separable states, is more effective in destroying the entanglement of the singlet, as compared to adding T_1 or T_{-1} on its own. In fact, T_0 and T_m are the most effective states in destroying the entanglement in the singlet state. The motivation for this argument is also discussed in Appendix ??, Section ??.
5. Finally, the “ternary” $S_0/T_0/T_m$ mixture,

$$\rho = \varepsilon S_0 + (1 - \varepsilon)(\chi T_0 + (1 - \chi)T_m), \quad \text{where } 0 \leq \varepsilon, \chi \leq 1, \quad (1.81)$$

will *always* be entangled for $\varepsilon > 1/2$, irrespective of the value of χ . This is illustrated in the two-dimensional plot, Figure 1.5(d), which also points towards additional subtleties, as now, $\varepsilon > 1/2$ is not a necessary but only a sufficient condition. This is suggested by the non-zero E_f for large values of χ , even when $\varepsilon < 1/2$, indicating that this time, the mixture is “reflecting” the entanglement present in the T_0 state.

6. For arbitrary mixtures, the state is always entangled when $\varepsilon > 1/2$; E_f depends only on ε , and is independent of the *relative* proportions of T_0 and T_m . A simple proof to this hypothesis is presented in Appendix ??, Section ??.
7. I now come back to the Werner state, (1.74), for which I have already shown that ρ_ε will be entangled for $\varepsilon > 1/3$. In fact, the Werner state can also be viewed as a ternary mixture, by decomposing the maximally mixed state into the singlet and triplets,

$$\frac{\mathbf{1}_4}{4} = \frac{S_0 + T_0 + 2T_m}{4}, \quad (1.82)$$

enabling us to re-write ρ_ε as,

$$\begin{aligned} \rho_\varepsilon &= \left(\frac{1-\varepsilon}{4}\right)(S_0 + T_0 + 2T_m) + \varepsilon S_0 \\ &= \left(\frac{1-\varepsilon}{4}\right)(T_0 + 2T_m) + \left(\frac{3\varepsilon+1}{4}\right)S_0, \end{aligned} \quad (1.83)$$

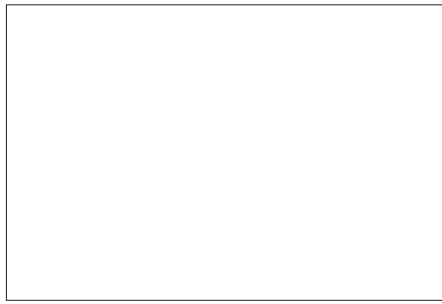


Figure 1.5: Entanglement of formation E_f for singlet triplet mixtures: (a) S_0 and T_0 , (b) S_0 and T_1 , (c) S_0 and T_m and (d) S_0 , T_0 and T_m . The E_f versus ε plot for an S_0/T_{-1} mixture is identical to (b).

where the co-efficient of S_0 , signifying the amount of singlet is now $(3\varepsilon + 1)/4$, instead of ε . The $\varepsilon > 1/3$ condition deduced above, then translates to the condition $(3\varepsilon + 1)/4 > 1/2$, which is identical to the threshold derived above for $S_0/T_0/T_m$ mixtures. Thus, states involving S_0 , T_0 and T_m , (including the Werner states), will always be entangled if the *amount of the singlet* exceeds the *entanglement threshold* of $1/2$. (A formal term for the amount of singlet in a state ρ is the *singlet fraction* [135] and is defined as,

$$F = \langle \psi^- | \rho | \psi^- \rangle. \quad (1.84)$$

A more concise proof of these arguments can also be found in [137]: the reduced density matrices [31] for the state ρ , (1.81), are the maximally mixed states, $\mathbf{1}_2$. It has been shown that a state ρ with maximally disordered subsystems, will be separable if and only if its largest eigenvalue is at the most, $1/2$. The state ρ has an eigenvalue f , ensuring *inseparability* for $f > 1/2$.

1.5 Methods for enhancing polarization

It is clear that pure initial states, also lying above the entanglement threshold cannot be achieved without resorting to some means for enhancing the polarization. Several methods have been proposed and implemented for reaching non-Boltzmann spin populations, and most of them have been motivated by the need for enhanced signal-to-noise ratios in conventional NMR. I now briefly review some of these methods in the context of quantum information processing.

1.5.1 High fields and low temperatures

One of the most obvious methods for increasing the polarization, achieving almost pure states, would be to increase $\mathcal{B} = \hbar\omega/kT$. Calculations with the single qubit fractional populations at room temperature, suggest that to achieve a purity of 99% ($n_\alpha = 0.99$ and $n_\beta = 0.01$), a magnetic field of roughly 200000 T is needed which is clearly impossible to achieve in the foreseeable future. Alternatively, using a reasonable field of 9.5 T requires a temperature as small as 10 mT, which is technologically possible, but no liquid exists at this temperature! Therefore, it seems that the naïve approach is not feasible and a more indirect method is needed.

1.5.2 Polarization transfer from nuclear spins

One method to increase the polarization of a qubit would be to “borrow” it from another more polarized qubit. Polarization transfer techniques exploit the small population differences in thermal states and the gains in sensitivity are proportional to γ_I/γ_S , the gyromagnetic ratios of the sensitive and insensitive nuclei. These techniques, for example, involve the incoherent nuclear Overhauser effect [3, 4, 7] or the coherent INEPT (**i**nsensitive **n**uclei **e**nhanced by **p**olarization **t**ransfer) sequence and its refocussed version, [3, 4, 7]; the latter two effectively acting as a kind of SWAP [138] between the sensitive and insensitive nuclei. However, in these experiments, not only are the gains small for most nuclei of interest, but also, it is not clear how they can be of any use in enhancing polarizations in ^1H nuclei, which already have the largest gyromagnetic ratios (besides ^3H). Due to these very limitations, these methods are likely to be of little value in realizing hyperpolarization for NMR quantum computers.

1.5.3 Polarization transfer from electron spins

Instead, it is more promising to make use of the hyperfine interaction: highly polarized electrons cannot only facilitate in indirectly detecting nuclear spins (Section 1.3), but can also contribute in the converse manner by transferring polarizations *to* the nuclei. These techniques have been given the generic name of *dynamical nuclear polarization* (DNP) [1], and are closely related to the original Overhauser effect [139, 140]: one of the spins in a coupled pair is perturbed from equilibrium and cross-relaxation effects [3, 4] result in enhanced polarization for the unperturbed spin. In DNP, the pair of

spins are a nucleus and an unpaired electron. Another related experiment is ENDOR (**e**lectron **n**uclear **d**ouble **r**esonance) [141], which traditionally involves transferring electron polarizations to the nuclei, performing an NMR experiment and detecting the NMR transitions indirectly, by transferring nuclear polarizations back to the electrons. For example, using the ENDOR approach, Mehring *et al.* recently demonstrated [82] preparation of pseudoentangled states between nuclear and electron spins. However, all of these methods are mostly employed in the solid state and their real potential in the liquid phase is only recently being explored; for example, it has been demonstrated that during rapid dissolution of a solid sample polarized by the DNP effect, the nuclear polarization is preserved, and can result in enhancements of four orders of magnitude [142].

Optical pumping and spin exchange

Another important method that produces non-Boltzmann spin distributions is optical pumping followed by spin exchange [143, 144]: circularly polarized laser light is used to pump electrons in alkali metal vapour (such as Rb) into a non-equilibrium distribution, increasing the electronic spin polarization by as much as four orders of magnitude. The electronic polarization is then transferred to the nuclear spins in a noble gas such as ^{129}Xe via the hyperfine interaction. Optical pumping is, therefore, another example of transferring polarization from electrons to nuclei. The method, however, is limited in its applicability to quantum computing, because only a few noble gas isotopes are known to be polarizable by optical pumping, and being chemically inert, they do not normally participate in bond formation, resulting in isolated systems unsuitable for universal quantum information processing. In principle though, the spin polarization of the Xe nuclei *can* be transferred to protons using SPINOE (**s**pin-**p**olarization **i**nduced **n**uclear **p**olarization) [145, 146, 147]—without the need for irradiating the spins, as in a conventional Overhauser experiment—but the transfer efficiency remains very low (nearly 10%). One demonstration of using optical pumping to obtain a ten-fold increase in polarization over the thermal state, and subsequently implementing a quantum algorithm is given in [148].

1.5.4 Chemically induced dynamical nuclear polarization

CIDNP (chemically induced dynamical nuclear polarization) [4, 5] is a misleading name for another technique for generating enhanced magnetic ordering; the method is unrelated to the dynamical nuclear polarization discussed above. The effect is based on the experimental observation that nuclear spins can “steer” the course of a chemical reaction; this seems quite a remarkable fact because the nuclear spin Zeeman energies are negligible as compared to bond energies, yet the former can exert a decisive influence on bond formation. I present a simple description of this phenomenon. Suppose we are given a pair of free radicals \mathbf{A}^* and \mathbf{B}^* , where $*$ represents an unpaired electron and \mathbf{B} is a spin-1/2 nucleus, that can exist in the state $|\alpha\rangle$ or $|\beta\rangle$. Also suppose that the radicals are “caged” together in solution, and the pair of lone electrons are in a triplet state ($T_0, T_{\pm 1}$). Recombination *inside* the cage (geminate recombination) takes place only if the pair of electrons can be brought into the singlet state (S_0), as required in a stable, bonding molecular orbital [149]. The reaction,



therefore, can happen only if there is a concomitant triplet to singlet conversion of the electronic states. How can such a conversion take place? The nucleus \mathbf{B} is hyperfine coupled with its electron and causes the electronic spin state to precess at a certain frequency, allowing the parallel T_0 configuration to evolve towards the anti-parallel S_0 , and the conversion will be more favoured if \mathbf{B} is in one particular spin state rather than the other. Suppose the $|\alpha\rangle$ state encourages the $T_0 \rightarrow S_0$ conversion. This implies that most geminally recombined radicals, that is the molecules \mathbf{AB} , will have the \mathbf{B} nuclear spins predominantly in the $|\alpha\rangle$ state. Likewise, the remaining molecules will eventually escape the cage and will recombine instead with the solvent or some other species, possibly forming another molecule \mathbf{CB} , this time with preferential magnetic ordering in the $|\beta\rangle$ state. At the end, we have two distinct manifolds comprising spin-polarized molecules. For QIP, the prospects of CIDNP are as yet unexplored. For example QIP requires multiple polarized spins in a *single* molecule and it is not clear how this can be realized by CIDNP.

1.5.5 *Para*-hydrogen derived hyperpolarization

The *para*-hydrogen induced polarization (PHIP) effect has been used not only to obtain large enhancements in spectroscopy [150] and imaging [151] applications, but has also demonstrated initial success in quantum information processing [58, 59, 152, 153, 154] in the liquid state. The following three chapters of this thesis will describe the PHIP effect (Chapter 2); employing it to prepare pure, entangled states (Chapter 3); and the first demonstrations of quantum algorithms on the pure state NMR quantum computer (Chapter 4).

Chapter 2

Para-hydrogen induced polarization

“...NMR is the premier spectroscopic example, not of quantum mechanics, but of quantum *statistical* mechanics [92] ...” The fact that most high temperature NMR quantum (statistical) computers, are in fact, “ensemble processors” [17], with spins statistically distributed in closely spaced energy levels, requires the generation of pseudopure states. However, we have also seen that the pseudopure approach cannot lead to computers of useful sizes. It appears that quantum statistical mechanics limits the usefulness of NMR as a viable technology for future computing, and the opening remark to this chapter, is a reflection of this view.

Ironically, quantum statistical mechanics also helps in overcoming some of the obstacles it creates for itself in the first place: the connection between spin statistics and sensitivity enhancement in NMR [155], was known even before NMR celebrated its debut in the quantum computing arena. One possible solution to enhanced NMR sensitivity exploits the coupling between nuclear spin and molecular rotation and the coupling obeys rules laid out by quantum statistical mechanics. The origin of the hyperpolarization lies in the almost perfect *spin order*, sometimes also called the *symmetrization order* [156] of the nuclear spin state derived from *para*-hydrogen. Our motivation in using this spin order is in producing nearly pure states in liquid NMR, thereby initializing the quantum computer in a well-defined state and realizing entanglement in high temperature liquids.

This chapter is a foray into the fundamentals of the spin order which arises as

a result of the strict correlation between the nuclear spin and molecular rotational degrees of freedom. I shall explore the symmetry requirements on the wavefunction of a diatomic molecule, such as dihydrogen. These requirements apparently restrict “homonuclear freedom”, but in effect, cool the pair of nuclear spins into a pure quantum state. The symmetrization postulate [157, 158, 159] results in the existence of two distinct spin isomers of the molecule; this effect is discussed in Section 2.1. Sections 2.2 and 2.3 explain the relative proportions of the spin isomers and outline some methods of isolating the *para* isomer. For quantum computing, the exceptionally high purity “locked” in the *para*-hydrogen molecule has to be transferred to a suitable molecule in solution; the underlying chemistry is described in Section 2.4. A thorough description of the nuclear spin states in *para*-hydrogen and its derivatives in solution requires a formal treatment in the language of density operators. This formalism is spelled out in Section 2.5. The hydrogenation can take place outside or inside the strong magnetic field leading to different descriptions. These experiments are outlined in Sections 2.6 and 2.7. The signal enhancements in these experiments are described in Section 2.8. Depending on the details of the hydrogenation and detection, variants of the *in situ* experiment are possible, which are explained in Sections 2.10–2.12. Finally, I present a brief summary in Section 2.13. In short, this chapter prepares the necessary theoretical background for the initialization experiment to be discussed in Chapter 3.

One of the most comprehensive reviews on *para*-hydrogen induced polarization (which I shall define later) is [160], while one of the earliest is [161]. Another review focusing on the chemical applications is [150].

2.1 Spin isomers of hydrogen

In common usage, the word “hydrogen” can refer to either the simplest atom, H, or the diatomic molecule, H₂. To keep the following discussion clear, I shall refer to the diatomic molecule as dihydrogen. We observe that even a simple molecule such as dihydrogen can exhibit a vast richness of properties. One such property is its nuclear spin isomerism [162] and forms a central topic of this chapter.

The spin isomers are a result of the symmetrization postulate and the Pauli principle [84, 163, 157, 158, 164], which impose certain symmetry requirements on a composite system comprising any number of identical particles: under the exchange of any two

particles, the *total* wavefunction must be either symmetric (even) or antisymmetric (odd). Furthermore, for particles, which are called *fermions*, the wavefunction must be odd under the exchange operation, also called the parity operation \mathcal{P} [31].

Suppose we have two fermions in distinct positions; I label their positions as A and B and assume their wavefunctions are χ and ϕ . The overall wavefunction could then be written as $\psi = \chi_A \phi_B$, and if we interchange their labels the resulting wavefunction becomes $\psi' = \mathcal{P}(\psi) = \phi_A \chi_B$. Now, the Pauli principle simply requires the wavefunction to be odd, *i.e.*, $\psi' = -\psi$. There is another interesting consequence of the odd symmetry of the fermionic wavefunction. If the fermions have the same position, say A , then $\phi_A \chi_A = -\chi_A \phi_A$ implies a vanishing wavefunction, $\psi' = -\psi = 0$: two fermions with identical wavefunctions *cannot* occupy the same position, they are *excluded* from being in the same state—this latter fact being an expression of the Pauli Exclusion Principle.

For dihydrogen, containing two protons, which are of course fermions, the overall wavefunction ψ_{total} must be odd for the same reason. This wavefunction has contributions from several degrees of freedom, all of which we assume act independently. These contributions come from the electronic states, translational, vibrational and rotational molecular motions and nuclear spin degrees of freedom,

$$\psi_{total} = \psi_e \psi_{trans} \psi_{vib} \psi_{rot} \psi_{ns}. \quad (2.1)$$

In keeping with the Pauli principle, I analyze the parities of the five independent contributions, and permit only those combinations for which the overall parity comes out to be odd. For the dihydrogen molecule the ground state electronic function ψ_e is even [164]. Exchanging the protons in the diatomic molecule has no effect on the translational motion, which is simply a centre of mass motion, and so the translational part ψ_{trans} is also even. Likewise, for its vibrational motion, the molecule can be modelled as a pair of identical masses connected through a spring; interchanging the masses leaves the system unchanged, and so ψ_{vib} is also even. The first three contributions in (2.1) being even, the parity of ψ_{total} is therefore determined by the combined parity of the last two terms, ψ_{rot} and ψ_{ns} : even rotational terms must combine with odd nuclear spin terms and odd rotational terms must combine with even spin terms. The reasoning is simple: odd functions multiplied by even functions result in an odd product. This explains the exact correlation between the molecular rotation and nuclear spin degrees

of freedom. The natural question to ask next is how the individual wavefunctions ψ_{rot} and ψ_{ns} behave under the exchange operation.

The rotational wavefunction of the molecule is a representation [31] of the rotational state vector in the position space

$$\psi_{rot}(\theta, \phi) = \langle \theta, \phi | J, m_J \rangle, \quad (2.2)$$

where θ and ϕ are angles in space and J is the angular momentum quantum number of the molecule, m_J being its projection along the quantization axis. The function $\psi_{rot}(\theta, \phi)$ transforms under rotations like the spherical harmonic function $Y_{m_J}^J$ [84], and the parity operator rotates this function according to

$$\mathcal{P}(\psi_{rot}(\theta, \phi)) \propto Y_{m_J}^J(\pi - \theta, \phi + \pi) = (-1)^J Y_{m_J}^J(\theta, \phi) \propto (-1)^J \psi_{rot}(\theta, \phi), \quad (2.3)$$

which clearly shows that the parity is controlled by the quantum number J through the factor $(-1)^J$: an even J ($= 0, 2, 4, \dots$) results in symmetric rotational functions and odd J ($= 1, 3, 5, \dots$) gives rise to antisymmetric functions.

I now turn to the parities of the nuclear spin wavefunctions. The kets corresponding to ψ_{ns} for two spins can assume four forms,

$$|00\rangle = |T_1\rangle, \quad (2.4)$$

$$|11\rangle = |T_{-1}\rangle, \quad (2.5)$$

$$\frac{1}{\sqrt{2}}(|01\rangle + |10\rangle) = |T_0\rangle \quad \text{and} \quad (2.6)$$

$$\frac{1}{\sqrt{2}}(|01\rangle - |10\rangle) = |S_0\rangle. \quad (2.7)$$

The first three of these states (2.4-2.6) are characterized by the spin quantum number $S = 1$, and are referred to as the spin *triplet* states and are denoted in general as $|T_{sub}\rangle$. The subscripts 1, -1 and 0 correspond to the projection m_S of the triplets along the spin quantization axis. The state $|S_0\rangle$, given in (2.7), is characterized by $S = 0$ and is called the spin *singlet*. (Finding these nuclear spin vectors for a composite two-spin system is a straightforward application of the problem of addition of two angular momenta [84]). The proton is a spin-half particle (a fermion) and so for dihydrogen $S_1 = S_2 = 1/2$, implying that the total angular momentum quantum number S can be 1 or 0. The projections for $S = 1$, are clearly $m_1 = \{1, -1, 0\}$ and for $S = 0$ the only possible projection is $m_0 = \{0\}$. Corresponding to the four distinct $\{S, m_s\}$

J	parity of ψ_{rot}	parity of ψ_{ns}	allowed spin vectors	form of H_2
0	even	odd	$ S_0\rangle$	<i>para</i>
1	odd	even	$ T_1\rangle, T_{-1}\rangle, T_0\rangle$	<i>ortho</i>
2	even	odd	$ S_0\rangle$	<i>para</i>
3	odd	even	$ T_1\rangle, T_{-1}\rangle, T_0\rangle$	<i>ortho</i>
\vdots				

Table 2.1: Correlation between molecular rotational and nuclear spin wavefunctions. *Para* and *ortho* spin manifolds of H_2 .

pairs, four nuclear spin states are possible, which are exactly the states (2.4)–(2.7). These kets also completely span the four dimensional Hilbert space of the two nuclear spins in dihydrogen and a basis comprising these basis elements is generally called the *symmetrical* basis.

For the purpose of establishing the correlation with the molecular rotational states, we are interested in the symmetry properties of these nuclear spin states. The triplets are symmetrical with respect to proton interchange whereas the singlet is antisymmetrical. For example, relabelling the spins in the singlet $|S_0\rangle$ would result in

$$|S_0\rangle = \frac{1}{\sqrt{2}}(|01\rangle - |10\rangle) \xrightarrow{P} \frac{1}{\sqrt{2}}(|10\rangle - |01\rangle) = -|S_0\rangle. \quad (2.8)$$

In short, the nuclear spin triplets $|T_1\rangle$, $|T_{-1}\rangle$ and $|T_0\rangle$ have even spin wavefunctions and combine with odd rotational states. The singlet $|S_0\rangle$ has an odd spin wavefunction and must combine with even rotational states. This correlation is summarized in Table 2.1.

Now suppose we can sort the dihydrogen molecules according to their values of J , keeping *all* odd J molecules in one cylinder and *all* even J molecules in another. As molecular rotation and nuclear spin are intertwined, the “rotational sieve” also acts as a “spin sieve”, separating the singlet and triplet nuclear spin states. As a result, the odd J cylinder will be an equal mixture of the *three* kinds of triplet molecules, called *ortho* and the even J cylinder will solely comprise singlet molecules — their spin states are of just *one* kind and the molecules are termed *para*. Therefore if we can somehow partition the even and odd J rotational manifolds, then in principle one of these compartments will contain a pure quantum spin state. This pure quantum state is the initial state of our quantum computer and will be discussed in subsequent parts

of this thesis.

2.2 *Para*-hydrogen from the perspective of statistical mechanics

How do we in practice, achieve the spin sorting described above? Remembering that zero is an even number, we can cool the molecules to their rotational ground state $J = 0$ and expect all nuclear spins to be in the singlet state. This approach effectively freezes the rotation of the molecules, locking them into the rotational ground state, and as a result, traps the nuclear spins in the singlet state. It is like manipulating the spin manifold through a more congenial arbiter, the molecular rotational manifold—as we now explore.

The rotational energy levels are populated according to the Boltzmann equilibrium distribution [84, 163, 164], the fractional population n_J in each state being given as,

$$n_J = \frac{1}{Z} (g_J g_S \exp(-E_J/kT)), \quad (2.9)$$

Z being the relevant partition function, E_J the energy of the state with degeneracy $g_J g_S$, k the Boltzmann constant and T the absolute temperature. In the rigid rotor model [164, 165] of dihydrogen, the energy corresponding to the angular momentum P_J is,

$$E_J = \frac{P_J^2}{2I} = J(J+1) \frac{\hbar^2}{2I}, \quad (2.10)$$

where I is the moment of inertia of dihydrogen. Defining the *rotational temperature* [164],

$$\theta_r = \frac{\hbar^2}{2Ik}, \quad (2.11)$$

(2.9) can also be written as,

$$n_J = \frac{1}{Z} (g_J g_S \exp(-J(J+1)\theta_r/T)). \quad (2.12)$$

Among gases, dihydrogen has the largest rotational temperature of about 85 K (calculated from data for rotational constants presented in [162]). Furthermore, the energy difference between any two levels J and $J+1$,

$$(E_{J+1} - E_J)/k = \theta_r(J+1)(J+2) - \theta_r J(J+1) \quad (2.13)$$

$$= 2\theta_r(J+1) \quad (2.14)$$

is proportional to the rotational temperature and $J + 1$. For example, in dihydrogen the energy gap between the lowest ($J = 0$) and first excited ($J = 1$) rotational states corresponds to a temperature of $2\theta_r = 170$ K. It is therefore possible to cool to low temperatures, ensuring that most molecules are in the $J = 0$ state. All other diatomic molecules have smaller rotational constants and the $0 \leftrightarrow 1$ gap is smaller, requiring substantially lower temperatures to preferentially populate the $J = 0$ state. For example, in the homonuclear molecule comprising two deuterium nuclei, $^2\text{H}_2$, the lowest rotational states are separated by $2\theta_r = 86$ K; furthermore, as the deuterium nucleus is a boson (nuclear spin $I = 0$), the lowest rotational ($J = 0$) state would be populated by *ortho*-deuterium molecules.

In the absence of external electric and magnetic fields, the J th rotational state is $(2J + 1)$ -fold degenerate ($g_J = 2J + 1$), and the allowed projections are given as

$$m_J = -J, -(J - 1), \dots, J - 1, J, \quad (J \geq 0). \quad (2.15)$$

We have also seen that for even J , only one spin state (the singlet) is allowed and for odd J , three spin states (triplets) are allowed, and so the spin degeneracy g_S in (2.9) is one or three depending on the parity of J . These degeneracies allow us to write the partition function for the dihydrogen molecule,

$$Z = \sum_{J=0,2,4,\dots} (2J+1) \exp(-J(J+1)\theta_r/kT) + 3 \sum_{J=1,3,5,\dots} (2J+1) \exp(-J(J+1)\theta_r/kT). \quad (2.16)$$

2.2.1 *Para-ortho* ratios

With these expressions, we can determine the relative ratio of the *para* and *ortho* molecules,

$$\frac{N_{para}}{N_{ortho}} = \frac{\sum_{J=even} (2J+1) \exp(-J(J+1)\theta_r/kT)}{3 \sum_{J=odd} (2J+1) \exp(-J(J+1)\theta_r/kT)}. \quad (2.17)$$

The fraction is a function of temperature and can be calculated numerically for different values of T , however analytical expressions can also be found under certain assumptions. For example, in the high temperature limit $T \gg \theta_r$, the spacing between the levels is small compared to kT and the discrete levels can be treated as a continuum of levels, replacing the discrete sums in (2.16)–(2.17) with continuous integrals. For example, consider the sum

$$\sum_{J=0}^{\infty} (2J+1) \exp(-J(J+1)\theta_r/T). \quad (2.18)$$

Carrying out the substitutions $J(J+1) = x^2$, $2J+1 = 2x dx$ and $\theta_r/T = \alpha$, the sum can be approximated as

$$\int_{x=0}^{\infty} 2x \exp(-\alpha x^2) dx \quad (2.19)$$

which is in fact a standard integral [166] with the solution

$$\frac{1}{\alpha} = \frac{T}{\theta_r}. \quad (2.20)$$

Therefore, the sum over only the even or only the odd J states (in the high temperature limit) is,

$$\frac{1}{2} \frac{1}{\alpha} = \frac{1}{2} \frac{T}{\theta_r}. \quad (2.21)$$

These integrals allow us to calculate the *para:ortho* molecular ratio in the high temperature limit. From (2.17) and the values of the integrals, we get,

$$\frac{N_{para}}{N_{ortho}} \xrightarrow{T \gg \theta_r} \frac{T/(2\theta_r)}{3T/(2\theta_r)} = 1/3, \quad (2.22)$$

showing that at temperatures above $2\theta_r$, dihydrogen is essentially a $\approx 1 : 3$ mixture of *para* and *ortho* molecules.

At lower temperatures, when $T \lesssim \theta_r$, the sums in (2.16)–(2.17) must be calculated explicitly. The series rapidly converges as only the lowest J states (such as $J = 0, 1, 2$) are populated and it is both permissible and customary to take only the first few terms in,

$$\frac{N_{para}}{N_{ortho}} = \frac{1}{3} \left(\frac{1 + 5 \exp(-6\theta_r/T) + 9 \exp(-20\theta_r/T) + \dots}{3 \exp(-2\theta_r/T) + 7 \exp(-12\theta_r/T) + 11 \exp(-30\theta_r/T) + \dots} \right). \quad (2.23)$$

This expression can be evaluated numerically to estimate the percentage of *para*-hydrogen in a *para-ortho* mixture as a function of temperature. Results are presented in Table 2.2 and Figure 2.1, showing that at the temperature of liquid N_2 (77 K) we have roughly an equal mixture of *para* and *ortho*-hydrogen and at temperatures at or below 20 K, we obtain essentially pure *para*-hydrogen.

2.3 Preparation of *para*-hydrogen

Table 2.2 immediately suggests a method of preparing pure *para*-hydrogen: cooling the dihydrogen molecules to around 20 K and waiting for sufficient time, expecting the *para-ortho* mixture to equilibrate into the pure *para* form. However, this picture is not

Temperature T (K)	% age of <i>para</i> -hydrogen
300	25.06
200	25.25
150	28.56
100	38.55
80	46.45
77 (liquid N ₂)	50.47
60	65.46
40	88.66
20	99.81
18	99.93

Table 2.2: Percentage of *para*-hydrogen as a function of temperature.

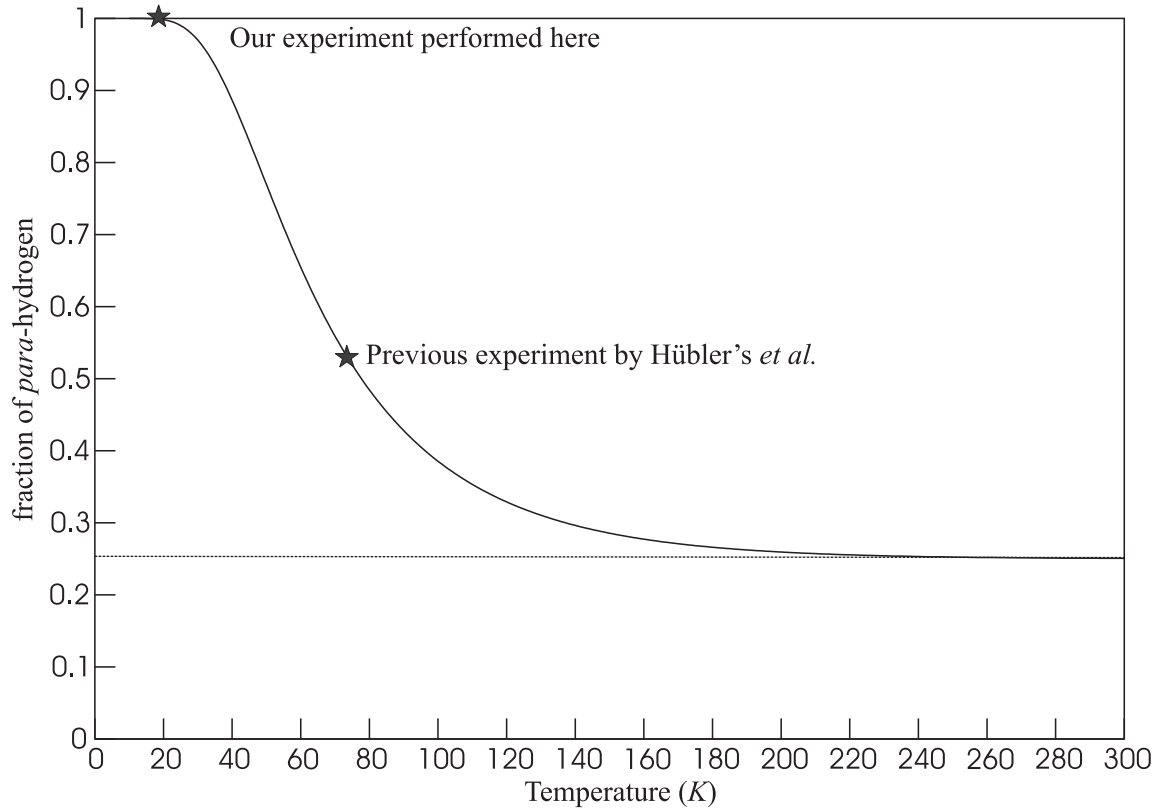


Figure 2.1: Percentage of *para*-hydrogen as a function of temperature T . The plot also indicates the *para*-hydrogen temperatures employed in our experiment [58] and the previous work by Hübler *et al.* [152]. These experiments are described in Chapter 3. The dashed line is a guide to the eye, representing a *para*-hydrogen fraction of $1/4$, the limit at high temperature.

accurate, to say the least. *Ortho* to *para* conversion is normally forbidden by angular momentum selection rules [162, 163, 164], and so we need a slightly more sophisticated approach. For *ortho* to *para* conversion, J must change by ± 1 and *at the same time* the nuclear spins must reorient from the $S = 1$ triplet state into the $S = 0$ singlet. This reorientation can take place for example, in the presence of dipolar couplings with neighbouring *ortho* molecules [167], however the intrinsic conversion is extremely slow [167] and takes place over a matter of days. To expedite the equilibration between the *ortho* and *para* manifolds, we can introduce an exogenous source of a magnetic field gradient [168], breaking the nuclear symmetry of the *ortho* molecules, and for this purpose a catalyst with paramagnetic properties is normally used.

The *ortho* \leftrightarrow *para* conversion takes place on or near the surface of the catalyst, rapidly achieving equilibration and the resulting *para:ortho* ratio reflects the temperature of the surface, in accordance with (2.23). If the surface temperature is about 20 K, the *ortho* to *para* conversion reaches almost 100% completion. Removing the catalyst and warming the *para*-hydrogen to room temperature does not significantly alter the purity of *para*-hydrogen as the *para* molecules do not convert back into the *ortho* form, by virtue of the same rules that had prohibited their generation in the first place. It appears as if the molecules “remember” the surface temperature, the ratio of the isomers continues to reflect the catalyst surface temperature¹. Upon warming, the molecules redistribute themselves in the even J rotational manifold according to Boltzmann rules; however their nuclear spin state does not change from the antisymmetrical singlet. Theoretically, we can store the *para*-hydrogen for indefinite periods of time; practically, for hours and whatever little conversion takes place is either at the surface of the storage cylinder or due to traces of impurities including residual *ortho* molecules.

Several experimental setups are being used for the generation of *para*-hydrogen in laboratories around the world (for an overview of the methods, see [150]). Our collaborators in York have devised a method that uses liquid He as the refrigerant,

¹This suggests that the *para-ortho* ratio can act as a reliable temperature probe. For example, studying this ratio for the isotopomers of water [169] in different comets, nuclear spin temperatures of ≈ 25 K have been suggested [170, 171], significantly cooler than the observed rotational temperatures. Due to the strongly forbidden *ortho* \leftrightarrow *para* conversion, we can glimpse the inter-stellar environment billions of years ago—approaching the lifetimes of comets!

cooling dihydrogen to temperatures as low as 7 K, allowing production of pure *para*-hydrogen. The *para-ortho* equilibration takes place on an activated charcoal catalyst. The H₂ outlet is equipped with valves that allow evacuation via a vacuum pump, and sample filling via a Young’s NMR tube adapter. Furthermore, the apparatus is equipped with a thermocouple, which allows the temperature of the H₂ gas to be controlled (our studies use temperatures in the range 18 K to 20 K), as well as a hydrogen pressure regulator on the inlet line and a pressure gauge on the outlet. The apparatus is left on permanently, except when the liquid helium reservoir needs to be re-filled, ensuring that high-purity *para*-hydrogen is always available.

The pure *para*-hydrogen results in extremely low spin temperatures [1], effectively in the mK range, while physically the gas can still be at room temperature. The spin temperature is now decoupled from the lattice temperature and from the perspective of the spins, the lattice is at infinite temperature, an approximation I shall use in modelling decoherence in our spin system (in Appendix ??). In other words, the spin entropy is very close to zero while the thermodynamic entropy of the gas remains very high. In effect, this is like placing a tiny spin refrigerator inside a molecular oven, which is hotter by five orders of magnitude.

2.4 Chemical addition reactions with *para*-hydrogen

Despite the exceptional purity, the *para*-hydrogen singlet state is spectroscopically useless. The $S = 0$ state is the solitary inhabitant of the even J rotational manifold and no other spin states are available to which nuclear spectroscopic transitions can occur [156]. So *para*-hydrogen is NMR silent. Furthermore, dihydrogen is a symmetric molecule and the two protons are magnetically equivalent [3]. There is no way to distinguish between the nuclei and so, if we wish to exploit the very high purity of our *para*-hydrogen product, we must somehow break the symmetry and transfer the singlet state to another more interesting molecule, which allows for some greater variety. It is therefore clear that some kind of chemical reaction is needed. In fact, chemical applications have steered research in *para*-hydrogen, which has now been used for a number of years, in probing the structure of transition metal complexes and the study of reaction pathways involving hydrogenation of unsaturated organic molecules. (For example, see [150] and the references therein.)

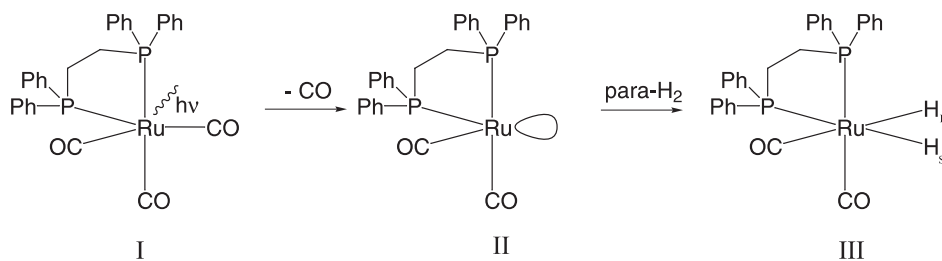


Figure 2.2: Photolysis reaction scheme for hydrogenation of $\text{Ru}(\text{CO})_3(\text{dppe})$ to produce $\text{Ru}(\text{H})_2(\text{CO})_2(\text{dppe})$. The Ph represents an aromatic phenyl group. The C and H atoms in the bidentate side chain are not shown.

Figure 2.2 shows the reaction scheme for a *photolysis* reaction [172, 173] involving the addition of *para*-hydrogen to a precursor molecule, **I**, $\text{Ru}(\text{CO})_3(\text{dppe})$ where (dppe) indicates 1,2-bis(diphenylphosphino)ethane [174]. The molecule is stable and does not normally add dihydrogen, but a UV photon knocks off one carbonyl group to generate an unstable intermediate **II**, which immediately reacts with *dissolved para*-hydrogen to give the desired product **III**, which I refer to as the *dihydride*. The intermediate, **II**, is a transitory species and is known to react with *para*-hydrogen almost instantaneously; the reaction, in fact, takes place on the sub-microsecond timescale [175]. The dihydride, **III**, contains two inequivalent hydrogen nuclei, H_I and H_S , the former being trans to a carbonyl group and the other, trans to a diphenylphosphino group. The two hydrogen nuclei form an **AX** spin system in the presence of a strong magnetic field.

However, only breaking the symmetry in the *para*-hydrogen molecule is not enough. The addition of *para*-hydrogen to the precursor **I**, must be coherent, preserving the singlet spin state, both in *form* and *magnitude*, quality and quantity. This means that the pure $|S_0\rangle$ state must remain unblemished during the chemical reaction, without dephasing into a mixture of states or decohering into the maximally mixed state, which is always accompanied by a loss of valuable polarization. The pair of hydrogen nuclei in the dihydride, in other words, must *fully inherit* the *pure* singlet state from the *para*-hydrogen molecule. This is possible only if the hydrogenation is *pairwise*, meaning that both protons bonding with a transition metal centre in a single molecule, are derived from the same *para*-hydrogen molecule. This concern for preserving the singlet is a major concern in our experiments involving *para*-hydrogen and will be discussed in detail in the following sections.

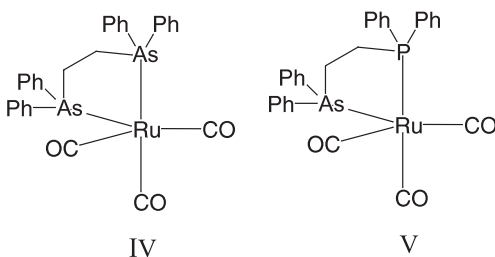


Figure 2.3: Compound **IV** is 1,2-bis(diphenylphosphino) ethane and **V** is a “mixed” phosphino-arsino compound 1,2-bis(diphenylphosphinoarsino) ethane

In addition to the “dppe” compound **I**, we have also used an analogue compound **IV** (see Figure 2.3), 1,2-bis(diphenylarsino) ethane, replacing the P atoms with As. Collaborators in York are also investigating other variants of **I** and **IV**, such as **V**, in which only one P atom is replaced with an As, or deuterating the compounds in the phenyl groups or the CH side chain, either fully or partially. In the context of *para*-hydrogen enhanced quantum information processing, the search for new compounds with better decoherence properties and more amenable spectral features continues, and chemistry continues to guide our way.

The reaction depicted in Figure 2.2 is photo-induced, which means that the reaction only takes place in the presence of a UV trigger. A very short (12 ns) flash of UV radiation (308 nm) from a pulsed excimer laser [172] is used to initiate the photochemical reaction. The reaction is triggered by the laser flash and is complete within one μs [175]. This allows precise control over the reaction, which can now be initiated and terminated at precise times. The laser effectively behaves as a switch, preparing pure singlet states in an **AX** system, as and when they are needed. Instead of using a single burst of radiation from a pulsed laser, we can also apply radiation for an extended period of time, using a continuous wave (CW) laser. In fact, we have performed experiments using both the pulsed and CW lasers, the former, for purposes of quantum computation and the latter, for purposes of demonstration and investigating the time dynamics of the spin system, especially over extended periods of time. The CW experiments, for example, can be useful in studying the decoherence properties of the system.

2.5 Operator description of the nuclear spin states in the *para*-hydrogen experiment

Investigating the *para*-hydrogen enhanced systems from a quantum mechanical perspective [160, 176], requires a description of the nuclear spin states in the language of density operators. The allowed spin states for the dihydrogen molecule are given in (2.4-2.7). Committing a slight abuse of notation, I drop the kets and use the same symbols to now represent the corresponding density matrices,

$$T_1 \equiv |T_1\rangle\langle T_1|, \quad T_{-1} \equiv |T_{-1}\rangle\langle T_{-1}|, \quad T_0 \equiv |T_0\rangle\langle T_0| \text{ and } S_0 \equiv |S_0\rangle\langle S_0|. \quad (2.24)$$

Writing these density operators (I call them states²) in the computational basis, we obtain,

$$T_1 = \{|1, 0, 0, 0\rangle\}, \quad T_{-1} = \{|0, 0, 0, 1\rangle\},$$

$$T_0 = \frac{1}{2} \begin{pmatrix} 0 & 0 & 0 & 0 \\ 0 & 1 & 1 & 0 \\ 0 & 1 & 1 & 0 \\ 0 & 0 & 0 & 0 \end{pmatrix} \quad \text{and} \quad S_0 = \frac{1}{2} \begin{pmatrix} 0 & 0 & 0 & 0 \\ 0 & 1 & -1 & 0 \\ 0 & -1 & 1 & 0 \\ 0 & 0 & 0 & 0 \end{pmatrix}. \quad (2.25)$$

These states can also be written in product operator notation as,

$$T_{\pm 1} = \frac{\mathbf{1}_4}{4} + \frac{1}{2}(\pm I_z \pm S_z + 2 I_z S_z), \quad (2.26)$$

$$T_0 = \frac{\mathbf{1}_4}{4} + \frac{1}{2}(2 I_x S_x + 2 I_y S_y - 2 I_z S_z) = \frac{\mathbf{1}_4}{4} + (ZQ_x - I_z S_z) \quad \text{and} \quad (2.27)$$

$$S_0 = \frac{\mathbf{1}_4}{4} + \frac{1}{2}(-2 I_x S_x - 2 I_y S_y - 2 I_z S_z) = \frac{\mathbf{1}_4}{4} + (-ZQ_x - I_z S_z) = \frac{\mathbf{1}_4}{4} - \mathbf{I} \cdot \mathbf{S}. \quad (2.28)$$

Pure *para*-hydrogen is the nuclear singlet state and would therefore be represented by S_0 given in (2.28),

$$\rho_{para} = S_0 = \frac{\mathbf{1}_4}{4} + (-ZQ_x - I_z S_z), \quad (2.29)$$

and pure *ortho*-hydrogen, being an equal mixture of the triplet states has an operator form,

$$\rho_{ortho} = \frac{1}{3}(T_1 + T_{-1} + T_0) = \frac{\mathbf{1}_4}{4} + \frac{1}{3}(ZQ_x + I_z S_z). \quad (2.30)$$

²The exact meaning of the word ‘state’ should be apparent from context.

Similarly a mixed state with a singlet fraction F will have the form,

$$\begin{aligned}\rho_F &= F\rho_{para} + (1 - F)\rho_{ortho} \\ &= \frac{\mathbf{1}_4}{4} + \left(\frac{1 - 4F}{3}\right)(ZQ_x + I_zS_z),\end{aligned}\tag{2.31}$$

which reproduces the states in (2.29-2.30) by setting $F = 1$ and $F = 0$ respectively.

2.6 *Ex situ* hydrogenation

There are two kinds of experiments involving addition of *para*-hydrogen to a precursor, depending on *when* and *where* the reaction takes place [160, 161]. The first method involves hydrogenating the precursor outside the magnet and slowly transferring it into the strong field of the spectrometer [177]; slow enough to ensure that the transfer is quantum mechanically adiabatic [84], but fast enough to be rapid in comparison with the T_1 recovery towards the Boltzmann populations. This experiment was called ALTADENA (**a**diabatic **l**ongitudinal **t**ransport **a**fter **d**issociation **e**ngenders **n**et **a**lignment) by its inventors [177].

In ALTADENA, the dihydride is formed outside the magnet, spins I and S acquire almost indistinguishable frequencies $\omega_I \approx \omega_S \implies (\omega_I - \omega_S) \ll 2\pi J$, and therefore constitute a strongly coupled \mathbf{A}_2 spin system. Only the S_0 state will be populated and the triply degenerate triplets $\{T_{\pm 1}, T_0\}$ will be separated from S_0 by the J coupling [176, 178], (Appendix ??,) as shown in Figure 2.4(a). The dihydride is then adiabatically transferred into the intense field with the result that the system becomes weakly coupled, $(\omega_I - \omega_S) \gg 2\pi J$, forming an \mathbf{AX} system. The eigenstates in the weakly coupled system are the product states and out of these four states, only $|01\rangle$ and $|10\rangle$ have a non-zero overlap with the singlet,

$$\left|\frac{1}{\sqrt{2}}\langle 01|01 - 10\rangle\right|^2 = \left|\frac{1}{\sqrt{2}}\langle 10|01 - 10\rangle\right|^2 = \frac{1}{2},\tag{2.32}$$

whereas,

$$\left|\frac{1}{\sqrt{2}}\langle 00|01 - 10\rangle\right|^2 = \left|\frac{1}{\sqrt{2}}\langle 11|01 - 10\rangle\right|^2 = 0.\tag{2.33}$$

Due to the adiabatic condition, the system ends up in one of these states and the details are described in Appendix ??. The experiment is schematically depicted in Figure 2.4(b). As only one state (assume $|\alpha\beta\rangle = |01\rangle$) is populated, two transitions are allowed, one for each spin, as is shown in the Figure. What the diagram does not

faithfully depict is the fact that if dephasing and decoherence are ignored, then the population difference between the populated and unpopulated levels will be of the order of unity; the spin order and state purity is conserved and the signal strengths will be very high as compared to the thermal signal intensities, shown somewhat generously, in part (d) of the same Figure.

The ALTADENA experiment is related in spirit, to the remote detection experiment [179], in which the magnetization is encoded in a low-field environment and then the sample is physically transported to a high-field magnet, conditions optimized for detection. However, such techniques which involve shuttling the sample back and forth are instrumentally demanding and for purposes of quantum information processing, we can achieve the same spin purity using an experimentally simpler approach.

2.7 *In situ* hydrogenation

The ALTADENA approach relies on slowly varying the Hamiltonian so that the spin system always remains in an eigenstate of the new Hamiltonian. What if the Hamiltonian changes suddenly, for example, by switching on the magnetic field B_0 instantaneously? This is the basis of a second kind of experiment, called PASADENA (***p****ara*-hydrogen **a**nd **s**ynthesis **a**llow **d**ramatic **e**nhancement of **n**uclear **a**lignment), and was discussed in the original prediction [156] of signal enhancements that are achievable using *para*-hydrogen. The effect can be explained using the “sudden” approximation [80] in quantum mechanics. Consider a state $\rho(t)$ and suppose that at time $t = 0$, the Hamiltonian suddenly changes from H_1 to H_2 . The approximation tells us that the state $\rho(t = 0^-)$ does not change at the very moment the perturbation takes place, *i.e.*,

$$\rho(t = 0^+) = \rho(t = 0^-). \quad (2.34)$$

Furthermore, for $t > 0^+$, the initial state $\rho(t = 0^+)$ evolves under the new Hamiltonian H_2 ,

$$\rho(t > 0^+) = \exp(-iH_2t) \rho(t = 0^+) \exp(+iH_2t), \quad \text{for } t > 0^+. \quad (2.35)$$

In zero-field conditions, the state of the two spin system is clearly $\rho_1 = \rho_{para}$ (as in 2.29) and whatever the Hamiltonian suddenly changes to, the new state of the system

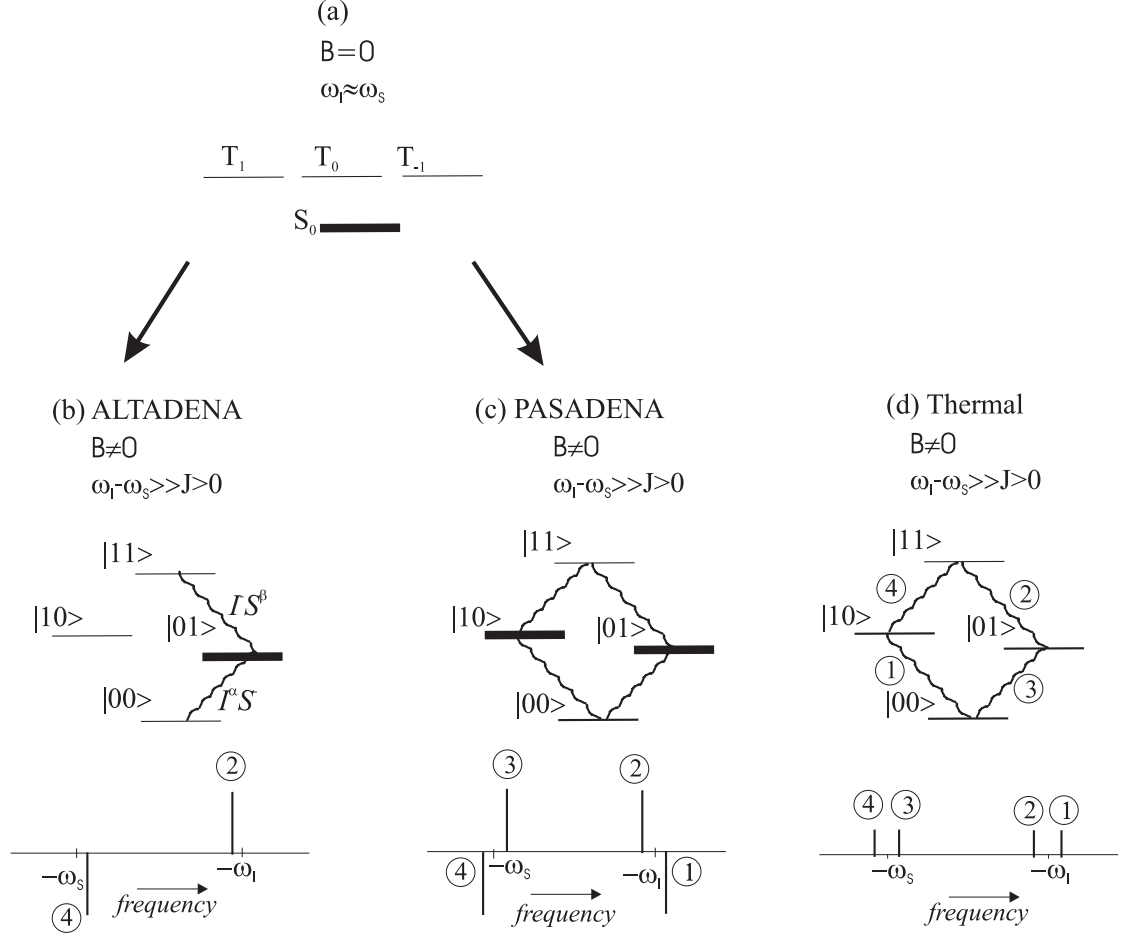


Figure 2.4: PASADENA and ALTADENA experiments: (a) is the energy level diagram for the dihydride product outside the magnetic field. Only S_0 is populated and the triplets are triply degenerate. Diagram (b) includes the ALTADENA population diagram and spectrum for small θ , (2.43). The diagram assumes that $\omega_S > \omega_I$, resulting in only the $|01\rangle$ state being populated. All spectra are drawn assuming $J > 0$ and follow the sign conventions described in [41]. Part (c) shows the population diagram and spectrum for the PASADENA experiment with selective excitation, (2.47). Finally, (d) shows the population diagram and spectrum for the thermal state, (2.39), also serving as a reference for labelling the coherences. In all spectra, frequency is positively increasing from left to right and the vertical heights of the spectra are not to scale.

at time $t = 0^+$ remains unchanged,

$$\rho(t = 0^+) = \rho(t = 0^-) = \rho_{para} = S_0. \quad (2.36)$$

Therefore $\rho_{para} = S_0$ is indeed an accurate initial state and can be directly used for determining the dynamics of our two qubit computer after the Hamiltonian switches from one form to another.

One means to instantaneously change the Hamiltonian is to carry out the experiment *inside* a strong field: the dihydride product is formed inside the magnet, instantaneously changing the spin system from \mathbf{A}_2 to \mathbf{AX} and therefore changing the Hamiltonian. This is the scheme we employed in our experiments. An *in situ* hydrogenation, can be achieved, quite conveniently, with our photolytic reaction, already illustrated in Figure 2.2, in which a laser is used to trigger the formation of the dihydride, at times of *our choosing*. Furthermore, the reaction takes place sufficiently fast, justifying the validity of the sudden approximation, which dictates that the two spins before and *immediately after* the *in situ* hydrogenation are in the state S_0 . This results in both the $|01\rangle$ and $|10\rangle$ levels being populated, as shown in the energy diagram in Figure 2.4(c), from which we deduce the possibility of four transitions, resulting in the characteristic PASADENA spectrum, a pair of anti-phase doublets. The exact form of the spectrum, however, depends on the details of the experiment and the excitation pulse, both of which I shall discuss shortly. It must also be remembered that population diagrams [4], such as the one shown in Figure 2.4(c), may sometimes lead us to the wrong impression: for example, it is not evidently clear whether the population distribution sketched out in Figure 2.4(c) suggests an incoherent mixture of states, $1/2(|01\rangle\langle 01| + |10\rangle\langle 10|)$, or the coherent state $1/2(|01\rangle - |10\rangle)(\langle 01| - \langle 10|) = S_0$. What we know from the PASADENA density matrix calculations, corroborated by the spectra, is that it is indeed the latter.

2.8 PHIP signal forms and enhancements

I have indicated that in ideal cases both ALTADENA and PASADENA preserve the purity of the quantum state. The perfect spin order of the pair of ^1H nuclei in the dihydride product, results in very strong signals, when compared with the signals derived from the thermal state. These exceptional polarizations, whether obtainable from

ALTADENA or PASADENA are often captured in the term *para-hydrogen induced polarization* or simply PHIP [160]. In fact, signal enhancements in NMR experiments involving hydrogen were observed even before the theoretical prediction of PHIP was made, and they were wrongly attributed [180] to CIDNP effects. Puzzlingly, the enhancements increased when hydrogen was stored in liquid N₂ temperatures for longer periods before the reaction, and only later, researchers realized the origin of these increased intensities and that storing the dihydrogen in ultra-cold environments simply increased the mole fraction of *para*-hydrogen. (For a historical review of the PHIP effect, see [160].)

The form and intensity of the PHIP signal depends upon the details of the experiment and the flip angle of the detection pulse. Consider a state ρ subject to a detection pulse P_d ; the state transforms to $\rho' = P_d \rho P_d^\dagger$ and consider the signal vector, (1.23), from ρ' , which I denote $\mathbf{Sg}(\rho, P_d)$. This vector indicates the *relative* directions (emission or absorption) and *relative* strengths of spectral lines; but additional information, including reference spectra, are needed to associate individual vector terms with individual spin resonances.

Thermal signal

For a two spin *homonuclear* system, the density matrix ρ_{th} in the high temperature limit $kT \gg \hbar\omega$ can be approximated³ as

$$\rho_{th} = \frac{\mathbf{1}_4}{4} + \frac{\mathcal{B}}{4}(I_z + S_z). \quad (2.37)$$

At 295 K and for a proton frequency of 400 MHz, the Boltzmann factor, \mathcal{B} , is 6.48×10^{-5} . A 90_y hard pulse converts ρ_{th} to the state

$$\rho'_{th} = \frac{\mathbf{1}_4}{4} + \frac{\mathcal{B}}{4}(I_x + S_x), \quad (2.38)$$

corresponding to the signal,

$$\mathbf{Sg}(\rho_{th}, 90_y) = \frac{\mathcal{B}}{8}\{1, 1, 1, 1\}. \quad (2.39)$$

³An equally valid approximation is $\mathbf{1}_4/4 - \mathcal{B}/4(I_z + S_z)$ in accordance with (1.49); but the sign of \mathcal{B} is immaterial for our purposes.

ALTADENA enhancement

The ideal ALTADENA experiment results in a state (*e.g.*),

$$\rho_{alt} = |01\rangle\langle 01| = \frac{\mathbf{1}_4}{4} + \frac{1}{2}(I_z - S_z - 2I_z S_z), \quad (2.40)$$

which can be excited by a θ_y detection pulse to yield the observable terms,

$$\frac{1}{2}(\sin \theta)(I_x - S_x) - \frac{1}{2}(\sin \theta \cos \theta)(2I_z S_x + 2I_x S_z). \quad (2.41)$$

If $\theta = \pi/2$, the vector becomes,

$$\mathbf{Sg}(\rho_{alt}, 90_y) = \frac{1}{4}\{1, 1, -1, -1\}, \quad (2.42)$$

showing that the spectrum comprises two in-phase doublets, one being in positive and the other in negative absorption. If the excitation angle θ is small, $\sin \theta \approx \theta$ and $\cos \theta \approx 1$ and the signal vector can be approximated as,

$$\mathbf{Sg}(\rho_{alt}, \text{small } \theta) \approx \{0, \theta/2, -\theta/2, 0\}, \quad (2.43)$$

showing that only the inner two transitions will be excited, in accordance with the ALTADENA spectrum predicted in Figure 2.4(b). Comparing (2.39) and (2.42), we can compute the relative enhancement of the signal intensities,

$$\eta_{alt} = \frac{1/4}{\mathcal{B}/8} = \frac{2}{\mathcal{B}}, \quad (2.44)$$

which is ≈ 30864 for a proton frequency of 400 MHz at 295 K, showing that the ALTADENA signals will be about four orders of magnitudes stronger than the thermal signal. This remarkable signal-to-noise enhancement motivated research in the detection of minor concentrations of dihydride isomers, sometimes appearing as intermediates, in catalytic hydrogenation reactions. The enhancement is itself a proof of the coherent addition of the pair of ^1H nuclei to the precursor: the hydrogens add pairwise, both nuclei coming from the same dihydrogen molecule.

PASADENA enhancement

The state after the PASADENA style *para*-hydrogenation is given by the singlet state (2.28,2.29,2.36) and to compute the enhancements, we must first consider a suitable detection pulse. A simple hard pulse will not work here: the singlet is an isotropic

state, with a deviation component $1/2(-2 I_x S_x - 2 I_y S_y - 2 I_z S_z) = -\mathbf{I} \cdot \mathbf{S}$, which is symmetric in the I and S spin operators. Hard pulses, also have symmetric spin Hamiltonians of the form $I_\alpha + S_\alpha$ and therefore commute with the isotropic state,

$$[\mathbf{I} \cdot \mathbf{S}, \theta(I_\alpha + S_\alpha)] = 0, \quad \text{where } \alpha = x, y, z. \quad (2.45)$$

So, the singlet remains invariant and therefore undetectable under hard pulses, suggesting the need to apply an asymmetric RF Hamiltonian. Soft pulses such $\theta_1 I_y + \theta_2 S_y$ with $\theta_1 \neq \theta_2$, asymmetrically excite the spin system and could therefore be used for detection. In our experiments, we use a soft $90 I_y$ pulse, selectively exciting *only* the I spin. We can deduce the observable terms using the product operator notation,

$$\begin{aligned} -\mathbf{I} \cdot \mathbf{S} &= \frac{1}{2}(-2 I_x S_x - 2 I_y S_y - 2 I_z S_z) \\ &\xrightarrow{90 I_y} \frac{1}{2}(2 I_z S_x - 2 I_y S_y - 2 I_x S_z) \\ &\xrightarrow{\text{obs}} \frac{1}{2}(2 I_z S_x - 2 I_x S_z), \end{aligned} \quad (2.46)$$

suggesting that the spectrum comprises two opposite anti-phase doublets. This is also captured in the corresponding signal vector,

$$\mathbf{Sg}(\rho_{para}, 90 I_y) = \frac{1}{4}\{-1, 1, 1, -1\}, \quad (2.47)$$

which suggests *seeing* a spectrum of the form $\{-, +, +, -\}$ or $\{+, -, -, +\}$ depending on the identities of I and S spin resonances, where “+” and “-” refer to positive and negative absorption lines respectively. The enhancement for the PASADENA $90 I_y$ experiment is identical to the ALTADENA $90 I_y$ detection, *i.e.*,

$$\eta_{pas} = \frac{1/4}{\mathcal{B}/8} = \frac{2}{\mathcal{B}}. \quad (2.48)$$

Similarly, if we have a mixed state of the form (2.31), the signal vector and enhancement will be rescaled by a factor of $(4F - 1)/3$, indicating that the enhancements are maximum for pure *para*-hydrogen.

In short, if we trigger the reaction inside the magnetic field using a short laser pulse and detect the singlet immediately after the product formation using a selective 90° pulse, we should observe two anti-phase doublets. Subsequently, allowing the spins to relax to the thermal state and detecting with a hard 90° excitation pulse, we shall see two in-phase doublets, and the intensities of the thermal signal would be smaller by a

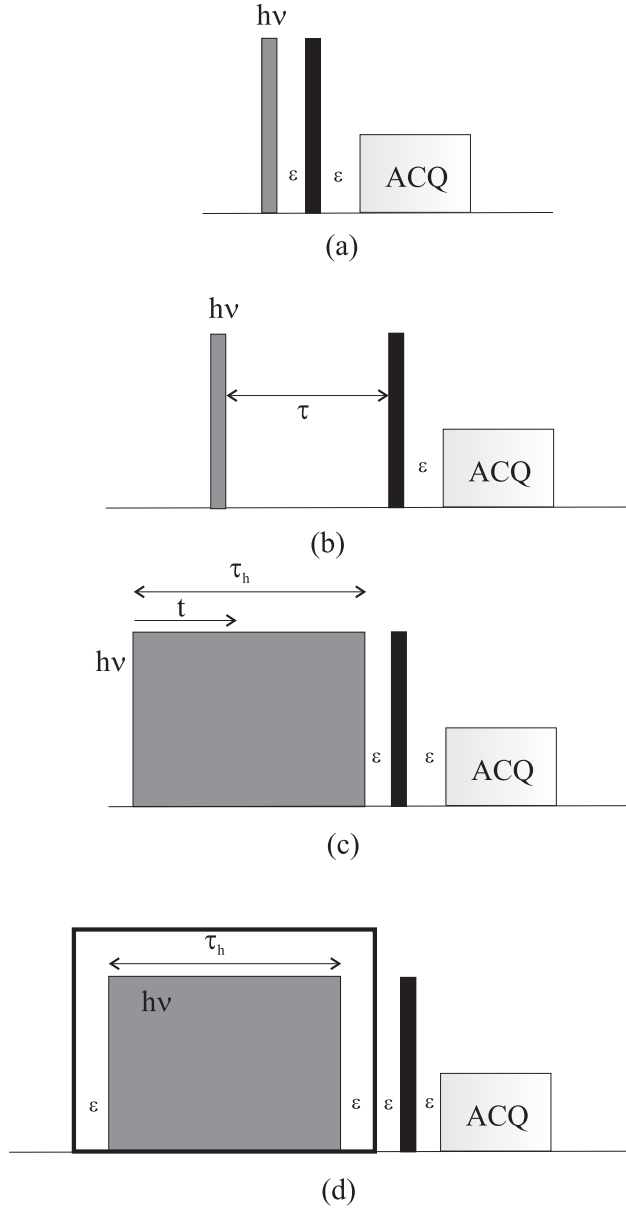


Figure 2.5: Different modifications of the PASADENA experiment: (a) instantaneous PASADENA involves detection right after a short laser flash from a pulsed laser, (b) the delayed version of PASADENA when the singlet is allowed to evolve for a duration τ before being detected, (c) incoherent PASADENA, representing hydrogenation for an extended period of time τ_h , which can be achieved using our CW laser, (d) isotropic PASADENA when extended hydrogenation takes place in the presence of an isotropic mixing sequence, shown here by an outlined rectangle. In each of these diagrams, the solid black rectangle represents a detection pulse of some kind, the grey rectangle represents laser irradiation, ACQ represents acquisition, and periods marked by ε are infinitesimal delays, shown only for illustrative clarity.

factor of $2/\mathcal{B} = 2\hbar\omega/kT$. This factor is ≈ 30864 for a proton frequency of 400 MHz at 295 K.

As a part of a research collaboration, we have investigated four kinds of experiments exploiting the PHIP effect.

1. In the *instantaneous* PASADENA experiment, we detect the singlet immediately after it is formed. The laser shot and the detection pulse are controlled through a common spectrometer trigger, synchronizing the two events. Instantaneous PASADENA is schematically sketched in Figure 2.5(a).
2. We also performed a *delayed* PASADENA: detecting the state at a time $\tau > 0$ after the dihydride product is formed. This is depicted in Figure 2.5(b).
3. Another modification is *incoherent* PASADENA, which involves hydrogenation over an extended period of time τ_h , shown in Figure 2.5(c).
4. The extended hydrogenation can also take place in the presence of an isotropic mixing sequence (to be described in Section 2.12). I call this experiment *isotropic* PASADENA, and is shown in Figure 2.5(d).

To understand these different versions of the PASADENA, we must first look at the evolution of the singlet in the presence of strong fields.

2.9 Singlet dynamics in strong field

The dihydride **AX** spin system will evolve in the presence of the **AX** Hamiltonian,

$$H = \Omega_I I_z + \Omega_S S_z + \pi J 2 I_z S_z, \quad (2.49)$$

where Ω_I and Ω_S are rotating frame angular frequencies of the two spins. Defining average and differential frequencies,

$$\Sigma = \frac{\Omega_I + \Omega_S}{2} \quad \text{and} \quad (2.50)$$

$$\Delta = \frac{\Omega_I - \Omega_S}{2}, \quad (2.51)$$

State ρ	$[\rho, I_z S_z]$	$[\rho, I_z - S_z]$	$[\rho, I_z + S_z]$
ZQ_x	0	$\neq 0$	0
DQ_y	0	0	$\neq 0$
$I_z S_z$	0	0	0

Table 2.3: Important commutation relations of different states ρ with operator terms.

the Hamiltonian can be rewritten as,

$$\begin{aligned}
H &= (\Sigma + \Delta)I_z + (\Sigma - \Delta)S_z + \pi J 2 I_z S_z \\
&= \overbrace{\Sigma(I_z + S_z) + \pi J 2 I_z S_z}^{H_c} + \overbrace{\Delta(I_z - S_z)}^{H_{nc}} \tag{2.52}
\end{aligned}$$

$$= H_c + H_{nc}, \tag{2.53}$$

where, in the last step, I have decomposed the Hamiltonian into two parts, H_c and H_{nc} , the first commuting and the second, non-commuting with the isotropic singlet,

$$[H_c, \mathbf{I} \cdot \mathbf{S}] = 0 \quad \text{and} \tag{2.54}$$

$$[H_{nc}, \mathbf{I} \cdot \mathbf{S}] \neq 0. \tag{2.55}$$

These Hamiltonians also commute between themselves,

$$[H_c, H_{nc}] = 0, \tag{2.56}$$

allowing us to make the simplification,

$$\exp(-iH\tau) = \exp(-i(H_c + H_{nc})\tau) = \exp(-iH_{nc}\tau) \exp(-iH_c\tau). \tag{2.57}$$

Important commutation relations between several operator terms are summarized in Table 2.3.

Considering only the deviation terms $(-ZQ_x - I_z S_z)$, the singlet S_0 evolves for time τ according to the prescription,

$$\begin{aligned}
-ZQ_x - I_z S_z &\xrightarrow{H\tau} \exp(-iH_{nc}\tau) \exp(-iH_c\tau) (-ZQ_x - I_z S_z) \exp(iH_c\tau) \exp(iH_{nc}\tau) \\
&= \exp(-iH_{nc}\tau) (-ZQ_x - I_z S_z) \exp(iH_{nc}\tau) \\
&\quad (\text{as } H_c \text{ commutes with the singlet, from (2.54)}) \\
&= \exp(-i\Delta(I_z - S_z)\tau) (-ZQ_x - I_z S_z) \exp(i\Delta(I_z - S_z)\tau). \tag{2.58}
\end{aligned}$$

The evolution can be simplified even further, as the $-I_z S_z$ term commutes with $\Delta(I_z - S_z)$,

$$[\Delta(I_z - S_z), -I_z S_z] = 0, \quad (2.59)$$

and so the problem is reduced to considering the evolution of the ZQ_x term under the Hamiltonian term $\Delta(I_z - S_z)$. The discussion leads us to two important observations. *First*, the singlet does not evolve under the weak coupling $2I_z S_z$ Hamiltonian and *second*, the evolution of the singlet is completely determined by the evolution of the zero quantum term $ZQ_x = I_x S_x + I_y S_y$, and that too, under only the term $\Delta(I_z - S_z)$, while the $-I_z S_z$ term remains invariant,

$$-ZQ_x - I_z S_z \xrightarrow{H\tau} \{\exp(-i\Delta\tau(I_z - S_z))(-ZQ_x) \exp(i\Delta\tau(I_z - S_z))\} - I_z S_z. \quad (2.60)$$

I now consider the evolution of *only* ZQ_x under *only* $\Delta(I_z - S_z)$. Suppose we place the transmitter (Tx) frequency in the exact centre of the I and S spin resonances; under these conditions, $\Omega_S = -\Omega_I$ and the angular frequency Δ becomes $(\Omega_I - (-\Omega_I))/2 = \Omega_I$, which for simplicity, I denote as Ω . With this definition, the spin resonances will be 2Ω or $2\pi\delta$ radians s^{-1} apart, where I have defined δ as the difference between the spin frequencies in Hz. (Frequency separation is $2\Omega = 2\pi\delta$ rad s^{-1} .) Now predicting the evolution of $-ZQ_x$ under the Hamiltonian $\Delta(I_z - S_z)$ is straightforward if we consider the commutation relation,

$$[ZQ_x, ZQ_y] = i \frac{(I_z - S_z)}{2}, \quad (2.61)$$

and, defining⁴,

$$ZQ_z = \frac{(I_z - S_z)}{2}, \quad (2.62)$$

enables us to write

$$[ZQ_x, ZQ_y] = iZQ_z, \quad (2.63)$$

which is in complete one-to-one correspondence with $[I_x, I_y] = iI_z$. I rewrite the Hamiltonian $\Delta(I_z - S_z)$ as $2\Delta(I_z - S_z)/2 = 2\Delta ZQ_z$, and predict the dynamics of ZQ_x ,

$$ZQ_x \xrightarrow{ZQ_z\tau} ZQ_x \cos(2\Delta\tau) + ZQ_y \sin(2\Delta\tau). \quad (2.64)$$

The evolution is illustrated in Figure 2.6 and shows that the ZQ_x term evolves in a subspace spanned solely by zero quantum vectors, $\{ZQ_x, ZQ_y, ZQ_z\}$, continuously

⁴This definition is found in [181] but it is not widely used in standard NMR literature.

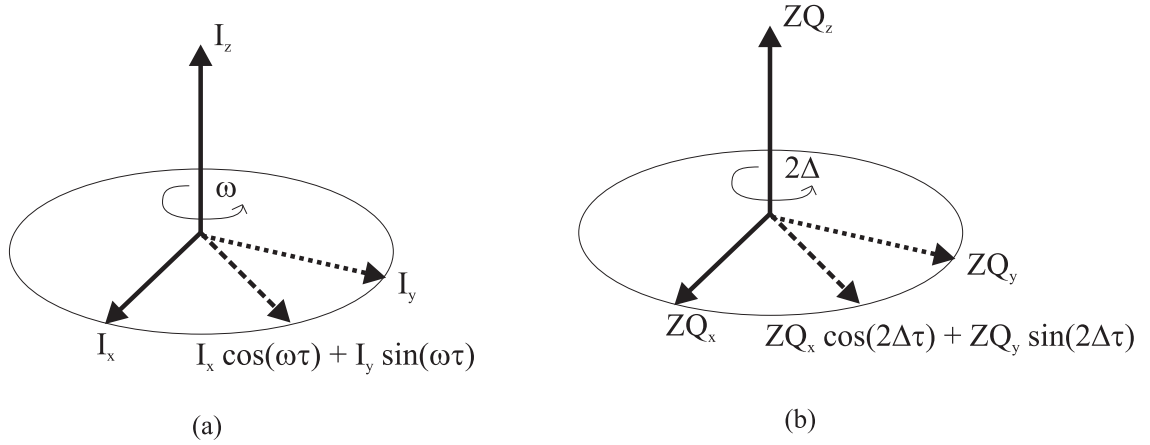


Figure 2.6: Correspondence between the dynamics of (a) single spin operators and (b) two spin operators in the zero quantum subspace. The correspondence is $I_z \leftrightarrow ZQ_z$, $I_x \leftrightarrow ZQ_x$, $I_y \leftrightarrow ZQ_y$ and $\omega \leftrightarrow 2\Delta$.

traversing the “transverse” zero quantum plane with a precession frequency $2\Delta = 2\pi\delta$, and sinusoidally interconverting between ZQ_x and ZQ_y .

2.10 Delayed PASADENA

I have already derived the signal obtainable from instantaneous PASADENA, (2.47), and I now predict the outcomes from the other experiments. In delayed PASADENA, the pure singlet evolves for a time τ under the Hamiltonian (2.49), in accordance with

$$S_0 \sim -ZQ_x - I_z S_z \xrightarrow{H\tau} -ZQ_x \cos(2\Delta\tau) - ZQ_y \sin(2\Delta\tau) - I_z S_z \quad (2.65)$$

$$= -ZQ_x \cos(2\pi\delta\tau) - ZQ_y \sin(2\pi\delta\tau) - I_z S_z \sim \rho(\tau), \quad (2.66)$$

provided we place the transmitter in the exact centre of the resonances. (As mentioned in Section 1.1.2, “ \sim ” denotes the deviation part of the matrix.) The second of these equations, (2.66), re-parameterizes the frequency in terms of the absolute frequency difference δ . The equation also shows that in time $\tau = 1/(4\delta)$, ZQ_x fully converts into ZQ_y and if we wait four times longer, *i.e.*, for $\tau = 1/\delta$, ZQ_x would go full circle and end up where it started from. This points towards the possibility of stroboscopic observation: if decoherence is neglected, S_0 would *appear* static at times which are multiples of the precessional time period, k/δ , for $k = 0, 1, 2, \dots$. Furthermore, $ZQ_y = I_y S_x - I_x S_y$ is antisymmetric in the I and S spin operators, and so we can detect the

state with a hard pulse. In Section 3.2, I shall describe how we can use properly timed delays, fully converting the symmetric ZQ_x into antisymmetric ZQ_y and hard pulses, to effectively achieve a selective $90 I_y$ pulse.

The state $\rho(\tau)$ (as in (2.66)), can be detected using either a selective $90 I_y$ pulse or a hard 90° pulse. The selective pulse, results in the observable terms,

$$\rho(\tau) \xrightarrow{90 I_y, \text{obs}} I_z S_x \cos(2\pi\delta\tau) - I_z S_y \sin(2\pi\delta\tau) - I_x S_z, \quad (2.67)$$

which compares with (2.46) by setting $(2\pi\delta\tau) = 0$. The resultant signal will take up the form,

$$\text{Sg}(\rho(\tau), 90 I_y) = \frac{1}{4} \{-1, 1, -\exp(2\pi\delta\tau), \exp(2\pi\delta\tau)\}, \quad (2.68)$$

indicating that the I spin remains in the anti-phase absorption mode, while the S lines contain dispersive components, the phases varying sinusoidally with τ , although they always remain 180° apart within themselves. A hard 90_x detection pulse applied to $\rho(\tau)$ results in the state,

$$\rho(\tau) \xrightarrow{90_x, \text{obs}} (-I_z S_x + I_x S_z) \sin(2\pi\delta\tau), \quad (2.69)$$

and the spectrum,

$$\text{Sg}(\rho(\tau), 90_x) = \frac{\sin(2\pi\delta\tau)}{4} \{1, -1, -1, 1\}. \quad (2.70)$$

2.11 Incoherent PASADENA

In incoherent PASADENA, the CW laser irradiates the precursor for an extended duration τ_h : singlets are formed at different times and consequently, evolve by different amounts. If the duration $\tau_h \gg 1/\delta$, the average state will be $\rho_{inc} = -I_z S_z$ as the terms in the ZQ plane will have dephased completely, as shown in Figure 2.7. Incoherent PASADENA is, in fact, a time-distributed ensemble of coherent processes, the averaging in time acts as decoherence in disguise [182].

The state ρ_{inc} is incoherent, yet the magnetic ordering is very high. Traditional PHIP experiments usually generate this state, after photochemical or thermal hydrogenation is allowed to proceed for a protracted length of time. A selective $90 I_y$ pulse converts it into the state,

$$-I_z S_z \xrightarrow{90 I_y} -I_x S_z, \quad (2.71)$$

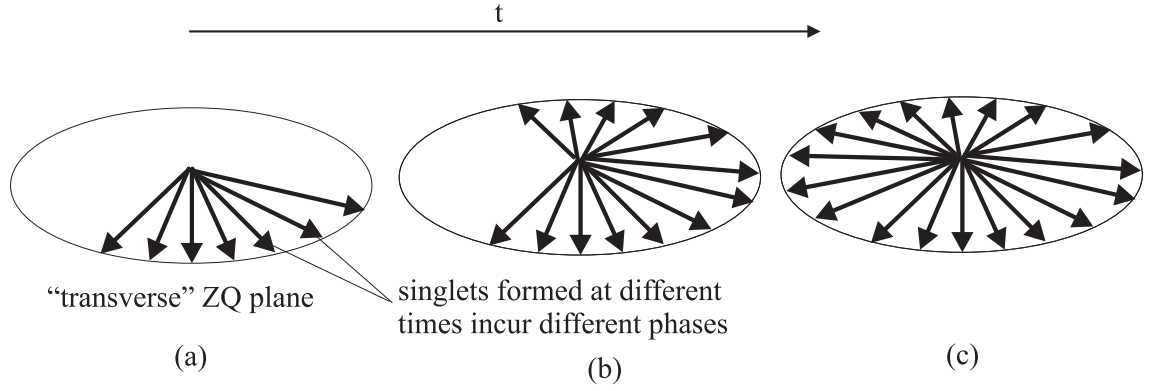


Figure 2.7: The incoherent PASADENA experiment. As time t increases from (a) through (c), new singlets are continuously being created and previously formed singlets begin to spread out in the ZQ plane. At the end of the irradiation period, $t = \tau_h$, the magnetization vectors are evenly distributed in the ZQ plane.

resulting in an anti-phase multiplet on the I spin while S remains completely “silent”,

$$\mathbf{Sg}(\rho_{inc}, 90 I_y) = \frac{1}{4}\{-1, 1, 0, 0\}, \quad (2.72)$$

and therefore could be used to identify the I or S identities of the multiplets. A hard 90_y pulse does not render the state observable, $-I_z S_z \xrightarrow{90_y} I_x S_x$; however, a θ_y pulse with $\theta \neq \pi/2$ converts ρ_{inc} into the state,

$$\begin{aligned} \rho_{inc} &\sim -I_z S_z \xrightarrow{\theta_y} -(I_z \cos \theta + I_x \sin \theta)(S_z \cos \theta + S_x \sin \theta) \\ &= -(I_z S_z \cos^2 \theta + I_z S_x \sin \theta \cos \theta + I_x S_z \sin \theta \cos \theta + I_x S_x \sin^2 \theta) \\ &\xrightarrow{\text{obs}} \frac{1}{2} \sin(2\theta) (I_z S_x + I_x S_z), \end{aligned} \quad (2.73)$$

with the resulting signal vector,

$$\mathbf{Sg}(\rho_{inc}, \theta_y) = \frac{1}{8} \sin(2\theta) \{1, -1, 1, -1\}. \quad (2.74)$$

The spectrum is of the form $\{-, +, -, +\}$ or $\{+, -, +, -\}$, comprising two anti-phase multiplets, and the intensities are maximized for the angle $\theta = \pi/4$. The 45_y hard pulse yields the spectrum,

$$\mathbf{Sg}(\rho_{inc}, 45_y) = \frac{1}{8} \{1, -1, 1, -1\}. \quad (2.75)$$

and the enhancement over the thermal signal (2.39) is found out to be,

$$\eta_{inc} = \frac{1/8}{\mathcal{B}/8} = 1/\mathcal{B}, \quad (2.76)$$

which is ≈ 15432 for a proton frequency of 400 MHz at 295 K, and is half the enhancements in the ALTADENA (2.44) and instantaneous PASADENA (2.48) setups.

2.12 Isotropic PASADENA

Isotropic PASADENA is a variant of incoherent PASADENA: hydrogenation is allowed to proceed for a duration τ_h , but in the presence of an *isotropic mixing* [4, 6] sequence. The experiment uses the CW laser and is shown in Figure 2.5(d). The singlet will evolve under the Hamiltonian (2.49). However, consider replacing H with a new Hamiltonian,

$$H_{J,\text{weak}} = \pi J 2 I_z S_z, \quad \text{or} \quad (2.77)$$

$$H_{J,\text{strong}} = \pi J 2 \mathbf{I} \cdot \mathbf{S}. \quad (2.78)$$

The state S_0 commutes with these coupling Hamiltonians, and is therefore, a stationary state, ideally remaining unchanged, even for extended lengths of time. Isotropic mixing sequences, built around inversion ($180_{x,y}$) pulses [35], in general, achieve the strong coupling Hamiltonian, (2.78), and therefore, hydrogenation in the presence of an ideal isotropic mixing preserves the singlet [152].

The Hamiltonian, (2.78), comprises only a J coupling and no Zeeman (or chemical shift) terms. In this case, $\Omega_I = \Omega_S = 0$, satisfying the so-called *Hartmann-Hahn* matching [6, 4, 181] condition, under which the polarizations are *mixed* (shared) between the spins, much like coupled pendulums continuously exchanging their kinetic energies, while keeping the total energy constant [183]. This energy-matched polarization transfer is the basis of the **total correlation spectroscopy**, TOCSY [184] experiment, which allows polarization to periodically “hop” among spins, even if they are not directly coupled.

The underlying concept in modifying a Hamiltonian is very simple and can be understood using a familiar example: the homonuclear spin-echo sequence [3, 7], shown in Figure 2.8. The sequence, shown in part (a) of the figure, sandwiches a 180_x pulse between two periods of free precession under the weak coupling Hamiltonian, (2.49). If the two spin system is observed after the second $\tau/2$ period, then the evolution can always be described by an effective Hamiltonian $H_{J,\text{weak}} = 2\pi J I_z S_z$, which involves only the scalar coupling term. Successive inversion pulses can be applied at intervals of τ , which should be less than $|1/J|$, and if the observation is synchronized with the

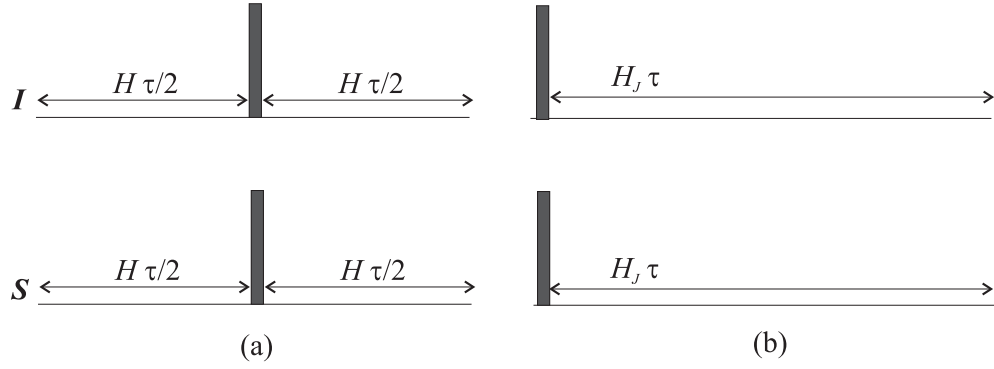


Figure 2.8: Modifying the \mathbf{AX} Hamiltonian (2.49), to make it “look like” $H_{J,\text{weak}} = 2\pi J I_z S_z$. The pulse sequence (a) is the spin echo and (b) is its equivalent description, provided observation is stroboscopic. The black rectangle in each case, denotes a 180_x hard pulse. The upper line is the spin I and the lower is S .

repetition rate, the effective Hamiltonian will be $H_{J,\text{weak}}$.

It is possible to “sculpt” more complicated Hamiltonians, using recurrent combinations of pulses and interspersed delays of free precession, or back-to-back pulses, and the mathematical theory of coherent averaging (also called average Hamiltonian theory) [2, 185], remains a powerful tool for analyzing such sequences. For example, different kinds of pulse sequences can be designed to attain an effective Hamiltonian of the form, (2.78). Most of these isotropic mixing sequences use composite pulses [42, 43, 45], instead of the simple inversion pulses, as depicted in Figure 2.8. The composite pulses can compensate systematic errors and act over larger frequency ranges without overly demanding power requirements. Different possibilities of ‘composite pulse mixing’⁵ sequences exist, and they are thoroughly investigated in [181].

Composite pulse mixing sequences are generally “built up” from their constituent pulses by a more or less algorithmic procedure, which is outlined in Appendix ?? for the MLEV-16 sequence [186]. I numerically investigated the performance of different naïve and sophisticated isotropic mixing sequences, in terms of their ability to preserve an ideal singlet state. These numerical results are also presented in Appendix ?. The next chapter describes our experimental results from isotropic PASADENA demonstrating the approximate preservation of the singlet.

⁵I use this non-standard phrase in comparison with the established phrase of ‘composite pulse decoupling’ [35, 181].

Experiment	excitation pulse	spectral form	predicted enhancement
ALTADENA	90_y	$\{+, +, -, -\}$	$2/\mathcal{B}$
Instantaneous PASADENA	$90 I_y$	$\{-, +, +, -\}$	$2/\mathcal{B}$
Delayed PASADENA	90_x	$\{+, -, -, +\}$	$2/\mathcal{B} \sin(2\pi\delta\tau)$
Incoherent PASADENA	45_y	$\{+, -, +, -\}$	$1/\mathcal{B}$
Incoherent PASADENA	$90 I_y$	$\{-, +, 0, 0\}$	$2/\mathcal{B}$

Table 2.4: Summary of the main results for ALTADENA and the various kinds of PASADENA style hydrogenations.

2.13 Summary of PHIP signals

The main results including suitable detection strategies, spectral forms and signal enhancements for different PHIP based experiments are summarized in Table 2.4. Predicted spectra for the different experiments are presented in Figure 2.9.

The next two chapters discuss our PHIP experiments.

1. Our primary motivation in harnessing the PHIP effect was to prepare pure initial states that could be used for quantum information processing. We experimentally demonstrate the preparation of such states using a single flash of a pulsed laser, utilizing instantaneous PASADENA detection. The resulting two qubit system is almost pure and also lies above the entanglement threshold.
2. With the isotropic PASADENA, we can demonstrate interesting dynamical characteristics of the singlet state, including decoherence.
3. Finally, we implement two quantum algorithms (Deutsch and Grover) using pure initial states, demonstrating for the first time the use of pure states in liquid state NMR for quantum computation; the experiments are taken up in Chapter 4 .

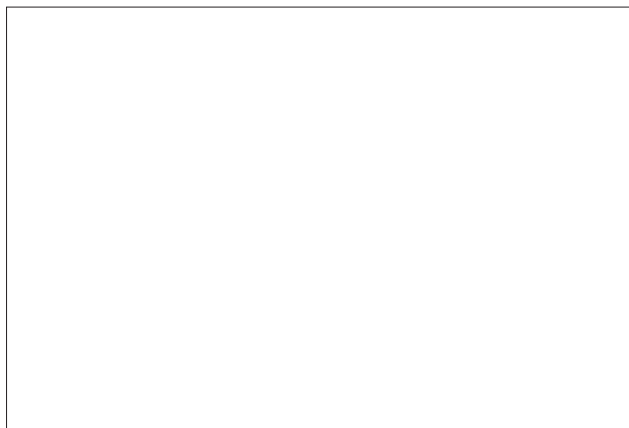


Figure 2.9: Predicted spectra from (a) an ALTADENA experiment with a 90_y detection pulse, (b) instantaneous PASADENA with $90 I_y$, (c) delayed PASADENA with 90_x , (d) incoherent PASADENA with a 45_y hard pulse and (e) incoherent PASADENA with a $90 I_y$ pulse. The I spin is *assumed* to be towards the left of the spectrum. All of these spectra are drawn to the same vertical scale; with (a), (b) and (e) of similar size and twice as big as (d). In plotting (c), I assumed $\sin(2\pi\delta\tau) = 0.6$, resulting in a signal smaller than (a) by a factor $1/0.6$.

Chapter 3

Preparing pure initial states using *para*-hydrogen

Every computation must start off in a well defined initial state. As seen in Chapter 1, one of the major objections against NMR as a scalable quantum computing technology, is the problem of initialization. This chapter deals with our initialization experiment, which is an important first and *successful* attempt at realizing an essentially pure quantum state, also capable of performing universal quantum dynamics. The state also lies above the entanglement threshold.

In our initialization experiment, pure *para*-hydrogen is prepared. The magnetic order is then coherently deposited into a molecule through a precisely controlled, fast chemical reaction. The migration of spin order from *para*-hydrogen to the molecule of interest must take place coherently and without appreciable loss, and at the end we must determine the density matrix and thus its purity and entanglement of formation. The preparation must also take place in a single experiment, without the need for multiple runs (as in temporal averaging schemes for pseudopure state preparation [87]). Our experiment demonstrably achieves all these requirements.

Section 3.1 describes a method of filtering the state for quantum state tomography in a single experiment and Section 3.2 describes the actual pulse sequence used for detection. The experiment itself, with all accompanying technical details is surveyed in Section 3.3. The acquired spectra are then processed and interpreted; the data processing and the final results are presented in Section 3.4. Finally, Section 3.5 shows some results from the isotropic PASADENA experiment, utilizing the CW laser. A

very concise description of this experiment can also be found in our published work, [58].

Unsurprisingly, the *para*-hydrogen route to achieving pure initial states has also been attempted previously [152], although the purity reached in that case was $\varepsilon \approx 0.1$, well below the entanglement threshold. Hübler and co-workers used the molecule $\text{Ir}(\text{H})\text{Cl}(\text{H})(\text{CO})(\text{PPh}_3)_2$ as their quantum computer, which they obtained from the addition of a 1 : 1 *para-ortho* mixture to their precursor molecule $\text{IrCl}(\text{CO})(\text{PPh}_3)_2$ (Vaska’s catalyst). Our results show an almost nine-fold improvement in the purity, and we attribute this increase to two factors. *First*, we use almost pure *para*-hydrogen, prepared at 20 K and using Equation (2.31) with singlet fractions $F = 1$ and $F = 1/2$, gives us a three-fold enhancement in the magnetic order straight away (see Figure 2.1). *Second*, the original experiment permitted hydrogenation for an extended period of time, resulting in signal loss due to the rotating frame spin-lattice relaxation, $T_1\rho$ [187] (in the presence of the isotropic mixing sequence [186]); and we believe relaxation diminished their purity by another factor of three. Our experiment overcomes this second problem by letting the reaction proceed to completion almost instantaneously. Pure *para*-hydrogen gas and faster reaction times, therefore, act together in bringing our purity levels very close to one.

3.1 One-shot tomography

Full state tomography requires multiple copies of ρ and so we have come up with a so-called partial “twirl”¹ operation, which prepares a state having only two independent parameters, and is therefore characterizable in a single experiment. Our procedure characterizes the state obtained *after* the assumedly perfect partial twirl, and not the initial state prepared by the laser flash. In this sense, the tomography is restricted to only a constrained state, in which several independent parameters have been zeroed out. (As I will discuss later, our experiments indicate that the constrained state is almost indistinguishable from the initial state.)

The ideal initialization experiment, which is instantaneous PASADENA, produces the singlet state, S_0 . If this were the case, no tomography is needed, as the output would be known before hand. However, more realistically, impurity terms mix in with

¹The twirl is the subject of Chapter 5.

S_0 . This could be due to several possible reasons: the small but finite reaction times, $ZQ_x \leftrightarrow ZQ_y$ mixing under the \mathbf{AX} Hamiltonian, the appearance of T_1 and T_{-1} terms due to spin-lattice relaxation and reaction with residual *ortho*-hydrogen. The partial twirl takes an input state, ρ_{in} , with all these error terms, and simplifies it into a known form, ρ_{out} ,

$$\rho_{in} \xrightarrow{\text{partial twirl}} \rho_{out}. \quad (3.1)$$

A key requirement of the partial twirl is that it leaves the singlet unchanged, both in form and fraction. Our partial twirl satisfies this requirement and outputs an $S_0/T_0/T_m$ mixture (see Section 1.4.6), a state of the form,

$$\rho_{out} = a S_0 + b T_0 + c (T_1 + T_{-1}). \quad (3.2)$$

The coefficients a , b and c are the singlet and triplet fractions, *i.e.*, $a = \langle S_0 \rangle = F$, $b = \langle T_0 \rangle$ and $c = \langle T_1 \rangle = \langle T_{-1} \rangle$. For a valid density matrix, $a + b + 2c = 1$, acting as a constraint on the $\{a, b, c\}$ trio; as a result, only two coefficients are linearly independent and one-shot tomography is possible. An alternative representation of ρ_{out} is in the product operator-multiple quantum basis,

$$\rho_{out} = \frac{\mathbf{1}_4}{4} + p ZQ_x + q I_z S_z, \quad (3.3)$$

which parameterizes the state in terms of p and q , the two independent parameters, which are directly related to the singlet and T_0 triplet fractions,

$$p = -a + b \quad \text{and} \quad (3.4)$$

$$q = 1 - 2a - 2b, \quad (3.5)$$

and conversely,

$$a = \frac{1}{4}(1 - 2p - q) \quad (3.6)$$

$$b = \frac{1}{4}(1 + 2p - q). \quad (3.7)$$

For pure S_0 , $a = 1$, $b = c = 0$ and $p = q = -1$. Tomography translates into determining the values of these coefficients. The initialization experiment therefore involves a single laser flash for making the dihydride, filtering it to bring it into the desired form, and finally measuring the state achieved; the overall scheme is shown in Figure 3.1.

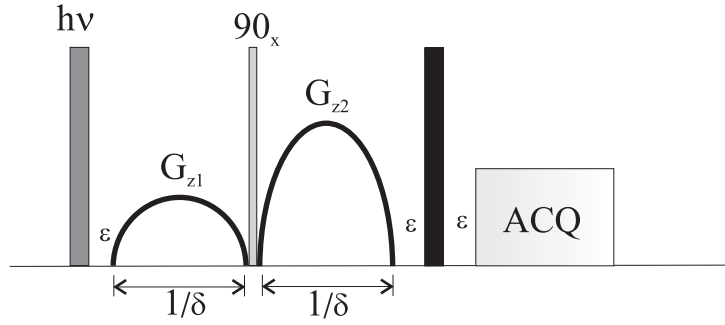


Figure 3.1: Scheme of the initialization experiment. The dark grey rectangle represents a single flash from the pulsed laser, the black rectangle indicates a $90 I_y$ detection pulse. The arcs show strong gradient fields, sandwiching a light grey rectangle, representing a 90_x pulse. The gradients and the intervening pulse comprise the partial twirl, also called the *filtration* sequence.

3.1.1 Implementing the partial twirl

The partial twirl comprises a pair of strong z gradients (crushes), \mathbf{G}_{z1} and \mathbf{G}_{z2} , of unequal strengths, surrounding a 90_x pulse. I assume all pulse elements to be ideal. We can understand the working of the $[\mathbf{G}_{z1} 90_x \mathbf{G}_{z2}]$ sequence by following the fate of the various terms in the density matrix as the sequence progresses. Defining the intermediate states ρ_1 and ρ_2 , the states transforms as,

$$\rho_{in} \xrightarrow{\mathbf{G}_{z1}} \rho_1 \xrightarrow{90_x} \rho_2 \xrightarrow{\mathbf{G}_{z2}} \rho_{out}. \quad (3.8)$$

I expand the deviation part of ρ_{in} in the product operator-multiple quantum coherence basis,

$$\begin{aligned} \rho_{in} \sim & e_1(I_x + I_y + S_x + S_y + I_x S_z + I_y S_z + I_z S_x + I_z S_y) \\ & + e_2(I_z + S_z) + e_3(DQ_x + DQ_y) + e_4(ZQ_y) + \{l(ZQ_x) + m(I_z S_z)\}. \end{aligned} \quad (3.9)$$

This is not a completely arbitrary state, as several terms are tied up with the same coefficient; however, the state is sufficiently general for our purposes. The terms with the e coefficients are the error terms and must therefore be prevented from reaching the output stage, ρ_{out} , while ZQ_x and $I_z S_z$ should survive the filtration.

The first gradient crushes all the single and double quantum terms, shown with coefficients e_1 and e_3 , resulting in,

$$\rho_{in} \xrightarrow{\mathbf{G}_{z1}} \rho_1 \sim e_2(I_z + S_z) + e_4(ZQ_y) + \{l(ZQ_x) + m(I_z S_z)\}. \quad (3.10)$$

The Zeeman ($I_z + S_z$) and anti-symmetric ZQ_y terms are transformed into single quantum coherences under the 90_x pulse and are crushed by the second gradient,

$$e_2(I_z + S_z) \xrightarrow{90_x} e_2(-I_y - S_y) \xrightarrow{\mathbf{G}_{z2}} \text{decohere}, \quad \text{and} \quad (3.11)$$

$$e_4(ZQ_y) = e_4(I_y S_x - I_x S_y) \xrightarrow{90_x} e_4(I_z S_x - I_x S_z) \xrightarrow{\mathbf{G}_{z2}} \text{decohere}. \quad (3.12)$$

Finally, for the ZQ_x and $I_z S_z$ terms, the $[90_x \mathbf{G}_{z2}]$ sequence mixes the l and m coefficients,

$$ZQ_x = I_x S_x + I_y S_y \xrightarrow{90_x} I_x S_x + I_z S_z = \frac{1}{2}(ZQ_x + DQ_x) + I_z S_z \quad (3.13)$$

$$\xrightarrow{\mathbf{G}_{z2}} \frac{1}{2}ZQ_x + I_z S_z \quad \text{and} \quad (3.14)$$

$$I_z S_z \xrightarrow{90_x} I_y S_y = \frac{1}{2}(ZQ_x - DQ_x) \quad (3.15)$$

$$\xrightarrow{\mathbf{G}_{z2}} \frac{1}{2}ZQ_x, \quad (3.16)$$

$$\implies l(ZQ_x) + m(I_z S_z) \xrightarrow{90_x} \xrightarrow{\mathbf{G}_{z2}} \frac{1}{2}(l + m)(ZQ_x) + l(I_z S_z) \sim \rho_{out}. \quad (3.17)$$

If we compare the above output, ρ_{out} , with (3.3), we deduce that $p = (l + m)/2$ and $q = l$, immediately suggesting that if $l = m = -1$, then $p = q = -1$, showing that the singlet component in ρ_{in} is completely conserved, as we desired. I now consider the effects of finite duration gradient pulses.

3.1.2 Finite duration gradient pulses

It is not possible to implement zero length gradients, so we can instead think about selecting the *proper* rather than just the *shortest* timings. For this purpose, we can use the results in Section 2.9: ZQ_x evolves in the transverse zero quantum plane according to (2.64), and therefore, setting the duration of each gradient to $t_g = (1/\delta)$, we ensure that ZQ_x is practically “frozen” in time. Furthermore, the $I_z S_z$ term does not precess at all, and neither of these terms evolves under the scalar coupling. For a ball-park figure of $\delta = 500$ Hz, $t_g = 1/\delta = 2$ ms, and the complete filtration sequence lasts for about $2(1/\delta) = 4$ ms, so no appreciable signal loss due to relaxation takes place in this small amount of time. (For example, considering a T_2 of 500 ms, the signal decreases by only 0.8%.)

In our initialization experiment, we use two schemes: one without (Figure 2.5(a)) and the other with (Figure 3.1) the partial twirl. State tomography shows very similar

results for the two experiments, indicating that the error terms (with coefficients e in (3.9)) are very small, and that the laser flash generates a state which is *close* to a Werner singlet.

We can also adjust the length of the gradient pulses to determine the I and S spin identities of the spectral multiplets. Halving the duration of each gradient from $(1/\delta)$ to $(1/2\delta)$ prepares the longitudinal state $I_z S_z$,

$$\begin{aligned} -ZQ_x - I_z S_z &\xrightarrow{\mathbf{G}_{z1}, t_g=1/2\delta} ZQ_x - I_z S_z = I_x S_x + I_y S_y - I_z S_z \\ &\xrightarrow{90_x} I_x S_x + I_z S_z - I_y S_y = DQ_x + I_z S_z \\ &\xrightarrow{\mathbf{G}_{z2}, t_g=1/2\delta} I_z S_z, \end{aligned} \quad (3.18)$$

which is converted to $I_x S_z$ by a $90 I_y$ detection pulse, resulting in the spectrum,

$$\mathbf{Sg}(I_z S_z, 90 I_y) = \frac{1}{4}\{1, -1, 0, 0\}. \quad (3.19)$$

The $I_z S_z$ state formed above is the same state, (of course with a negative sign,) as ρ_{inc} , (2.71), and the partial twirl with the gradient durations reduced to half, is therefore, a *way of making the incoherent state from the coherent state*. A selective pulse renders observable only one spin, which is unambiguously assigned the label I and the signal (3.19) together with (2.47) can then be used to determine the positive and negative amplitude directions in the spectral outputs.

3.2 The detection pulse

We have devised a detection pulse sequence, determining the parameters p and q , all that is needed to completely reconstruct the density matrix, ρ_{out} .

In fact, the detection pulse is simply the selective $90 I_y$ pulse already described in context of singlet detection in the PASADENA experiment (Section 2.8). The singlet (with $p = q = -1$) results in the spectrum (2.47) while the general state, (3.3), with arbitrary p and q , results in,

$$p(I_x S_x + I_y S_y) + q(I_z S_z) \xrightarrow{90 I_y} \xrightarrow{\text{obs}} p(-I_z S_x) + q(I_x S_z). \quad (3.20)$$

The coefficients do not mix and are seen on separate spins, the p coefficient prepended to the S observable and the q coefficient to the I observable. The resulting signal vector is,

$$\mathbf{Sg}(\rho_{out}, 90 I_y) = \frac{1}{4}\{q, -q, -p, p\}. \quad (3.21)$$

Excitation pulse P	signal vector $\mathbf{Sg}(\rho_{out}, P)$
$90 I_y$	$1/4 \{q, -q, -p, p\}$
θ_y	$1/8(p - q) \sin(2\theta) \{-1, 1, -1, 1\}$
90_y	$\{0, 0, 0, 0\}$
45_y	$1/8(p - q) \{-1, 1, -1, 1\}$

Table 3.1: Signal vectors from application of some hard and selective pulses on the output of the filtration sequence ρ_{out} as given in (3.3).

The signals resulting from applying different kinds of detection pulses are summarized in Table 3.1.

Two comments about the detection pulse are not out of place here.

1. The zero order phasing of the NMR spectrum is arbitrary. The y phase of the detection pulse results in absorption Lorentzians but using for example, a $90 I_x$ pulse instead would result in the dispersive spectrum,

$$\mathbf{Sg}(\rho_{out}, 90 I_x) = \frac{1}{4} \{iq, -iq, -ip, ip\} = i\mathbf{Sg}(\rho_{out}, 90 I_y), \quad (3.22)$$

which could be easily brought into the absorptive form.

2. Similarly we could have also applied a $90 S_y$ instead of a $90 I_y$ pulse without loss of generality. However, in our experiments and mathematical analysis, we consistently followed the $90 I_y$ description.

3.2.1 Implementing the selective detection pulse

There is a repertoire of methods available in the NMR literature [4, 188, 189] to apply selective pulses to one spin in a multi-spin system, the commonest being shaped pulses. In all our quantum information processing experiments, we have achieved spin selectivity using sequences based on the Jump-and-Return method [24, 60]. These kind of sequences, originally developed for water suppression, use only hard pulses and interleaving delays.

Here I present an explicit construction for designing the Jump-and-Return implementation of our $90 I_y$ selective pulse. The I selective pulse can be written as,

$$90 I_y \equiv \left\{ \begin{array}{c|c} 45 I_y & 45 I_y \\ \hline 45 S_y & 45 S_{-y} \end{array} \right., \quad (3.23)$$

the top and bottom rows comprising pulses on the I and S spins respectively, and time ordering in the pulse sequences being from left to right. Now, we know that a θ_y pulse can be decomposed² as a composite rotation [4, 62, 42],

$$\theta_y \equiv 90_x \theta_z 90_{-x}, \quad (3.24)$$

allowing us to rewrite (3.23) as,

$$90 I_y \equiv \left\{ \begin{array}{c|c|c|c} 45 I_y & 90 I_x & 45 I_z & 90 I_{-x} \\ \hline 45 S_y & 90 S_x & 45 S_{-z} & 90 S_{-x} \end{array} \right., \quad (3.25)$$

which can be expressed in more compact notation as,

$$45_y 90_x 45_{\pm z} 90_{-x}, \quad (3.26)$$

where the sequence now comprises only hard pulses and “contra-axial” ($\pm z$) pulses. This sequence can in fact be simplified [18] further. Rearranging the terms in (3.24), we are able to deduce the relation,

$$\theta_y 90_x \equiv 90_x \theta_z. \quad (3.27)$$

Furthermore, we can displace the z rotation to the left or to the right, while changing the phase of a neighbouring pulse. For example, using the identity,

$$\alpha_\phi \beta_z \equiv \beta_z \alpha_{\phi+\beta} \quad (3.28)$$

the sequence (3.27) becomes,

$$\theta_y 90_x \equiv 90_x \theta_z \equiv \theta_z 90_{0+\theta} \equiv \theta_z 90_\theta. \quad (3.29)$$

This allows us to re-write (3.26) in the form,

$$45_z 90_{45} 45_{\pm z} 90_{-x}, \quad (3.30)$$

²This identity can be easily proven by explicit calculation.

a sequence comprising a non-selective z rotation, a pulse, a contra-axial $\pm z$ rotation and a final pulse; both pulses being hard. This sequence is a *state independent* prescription for implementing a $90 I_y$ selective pulse. For the output of the filtration sequence ρ_{out} (3.3), comprising only ZQ_x and $I_z S_z$ terms, a further simplification is possible, as both terms in ρ_{out} commute with non-selective z rotations. In fact, the very purpose of the transformation (3.29) was to bring this z rotation to the beginning of the sequence; it has no effect on the state ρ_{out} and could therefore be simply dropped altogether. The pulse sequence for fully characterizing the filter output can therefore be written as,

$$90_{45} \ 45_{\pm z} \ 90_{-x}, \quad (3.31)$$

two hard pulses sandwiching a properly timed delay, in the spirit of the Jump-and-Return style selective pulses. The hard pulses are straightforward to implement, while the $45_{\pm z}$ rotation is achievable by observing its propagator form,

$$\exp\left(-i\frac{\pi}{4}(I_z - S_z)\right). \quad (3.32)$$

From this, we immediately recognize that a suitable Hamiltonian to implement this function would be the non-commuting part $H_{nc} = \Delta(I_z - S_z)$ of the background Hamiltonian H as described in (2.53). This Hamiltonian is achieved by *necessarily* placing the transmitter in the exact middle of the I and S spin resonances and allowing the two spin system to evolve under the background Hamiltonian H (2.49) for a time t_d ,

$$\Delta t_d = \frac{\pi}{4} \implies t_d = \frac{\pi}{4\Delta} = \frac{\pi}{4\pi\delta} = \frac{1}{4\delta}. \quad (3.33)$$

For a representative value of $\delta = 500$ Hz, this delay is $500 \mu\text{s}$.

The complete pulse sequence for the initialization experiment can therefore be written as,

$$\text{flash } \mathbf{G}_{z1,[t_g]} \ 90_x \ \mathbf{G}_{z2,[t_g]} \ 90_{45} [t_d] \ 90_{-x} \ \text{acquire}, \quad (3.34)$$

schematically represented in Figure 3.2(a). If the laser flash produces a hydride without any error terms in ρ_{in} , we could rather leave out the partial twirl altogether; the resulting scheme is shown in part (b) of the figure. We have performed both kinds of experiments and observe no appreciable difference between the results. Interestingly, if we *knew* that ρ_{out} is indeed the singlet with $p = q = -1$, we could also leave out the first hard pulse in the tomography sequence (3.31) as the singlet commutes with hard pulses. However, for mathematical completeness, we retain this initial pulse. A few additional comments about the detection pulse sequence are the following.

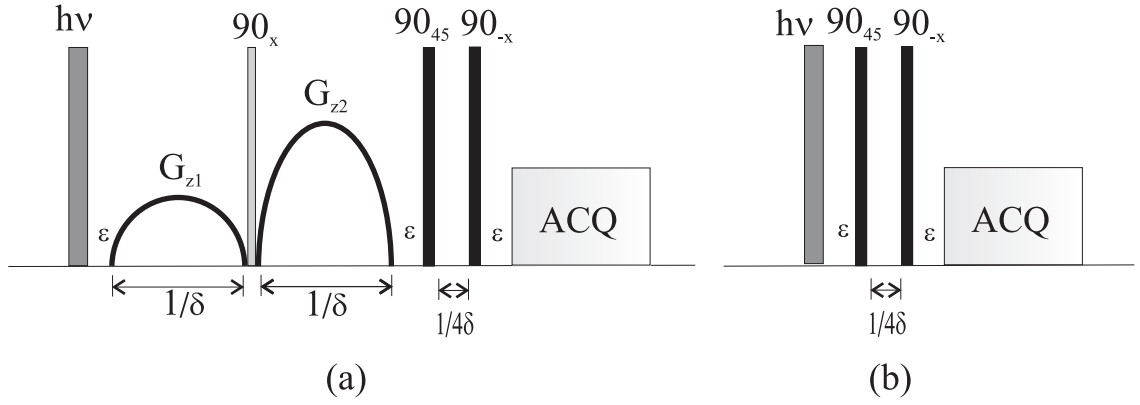


Figure 3.2: The initialization experiment pulse sequences with (a) and without (b) the partial twirl. All rectangles are appropriately labelled. The transmitter frequency is placed in the middle of the resonances.

1. Analysis shows that the inter-pulse delay, $t_d = 1/(4\delta)$ maximizes the ZQ_x to ZQ_y conversion, acting as a $\pi/2$ rotation in the transverse zero quantum plane.
2. The sequence is most robust against pulse width errors when the phases of the pulses are 135° apart. The role of errors in this sequence is considered in Appendix ??.

3.3 Experimental system and methods

In this section, I describe the experimental details of our instantaneous PASADENA experiment³.

³All experiments discussed in this and the next chapter, were performed by Dr. S. B. Duckett and Dr. D. Blazina at the University of York. This included synthesis and characterization of all compounds, manufacture of the *para*-hydrogen plant, building and adjusting the optics for efficient transfer of light to the sample, and finally implementing the pulse sequences on the spectrometer. Myself and my supervisor, at Oxford, were involved in pulse sequence design and analysis, data processing, state tomography, decoherence modelling, simulations and the theoretical design of the experiment. However, I visited York a couple of times to assist in the experiments and also carried out local experiments on simulated states.

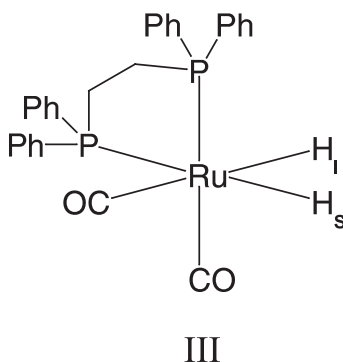


Figure 3.3: The product of the photolysis reaction, $\text{Ru}(\text{H})_2(\text{CO})_2(\text{dppe})$. The two qubits in the quantum computer are the protons H_I and H_S .

3.3.1 Chemical system

The molecules used in our experiment have already been identified in Section 2.4 and the photolysis reaction underpinning pure state preparation is illustrated in Figure 2.2. The stable precursor, **I**, $\text{Ru}(\text{C}\emptyset)_3(\text{dppe})$ is photolyzed using a laser flash, converting it into the transitory species, **II**, $\text{Ru}(\text{C}\emptyset)_2(\text{dppe})$, which immediately reacts with dissolved *para*-hydrogen producing $\text{Ru}(\text{H})_2(\text{C}\emptyset)_2(\text{dppe})$, **III** (Figure 3.3), the molecule of interest. The reaction takes place *inside* a magnet and is an example of instantaneous PASADENA.

The dihydride **III** is a well-characterized system [174] and no secondary isomers are known to be produced during or after the photolysis. The reverse reaction, **III** \rightarrow **I** is extremely slow at the operating temperature of 295 K. (The backward reaction is catalyzed by higher temperatures, above 340 K, and by the presence of $\text{C}\emptyset$.)

The precursor **I**, was dissolved in deuterated benzene (C_6D_6) and placed in a 5 mm (diameter) NMR tube; from which dissolved gases were subsequently removed using freeze-pump-thaw cycles, corresponding to, respectively, freezing with liquid N_2 , degassing and finally melting the sample. The tube was covered in Al foil to protect against premature photolysis by ambient light. *Para*-hydrogen prepared at 20 K was introduced into the tube, at a pressure of about 3 bar. Warming and subsequent shaking ensured that the *p*- H_2 gas dissolved in the solvent. All NMR studies were carried out with samples of approximately 1 mM concentration on a Bruker DMX-400 spectrometer with ^1H at 400.1 and ^{31}P at 161.9 MHz, respectively. NMR properties of the system and several other experimental parameters are summarized in Table 3.2.

System NMR parameters	
Ru(H) ₂ (CØ) ₂ (dppe)	
resonance frequencies	−6.32 and −7.55 ppm
δ	492 Hz (on the 400 MHz spectrometer)
¹ H T_1 (single quantum)	1.7 s
¹ H T_2 (single quantum)	0.58 s
² J_{HH}	4.6 Hz
Experimental parameters	
Proton frequency	400 MHz
System temperature (T)	295 K
$t_{\pi/2}$	8.25 μs
Number of laser flashes (F) for control *	1000
Inter-flash delay (t_f) *	7 s
Number of scans (S) *	3072
Inter-scan delay (t_s) *	20 s
Active volume fraction (V_f) *	12.5/34 = 0.368
Spectral width	\approx 30 ppm
Receiver gain	128

Table 3.2: Important system and experimental parameters involved in the initialization experiment. Parameters marked with a “*” are described in the text.

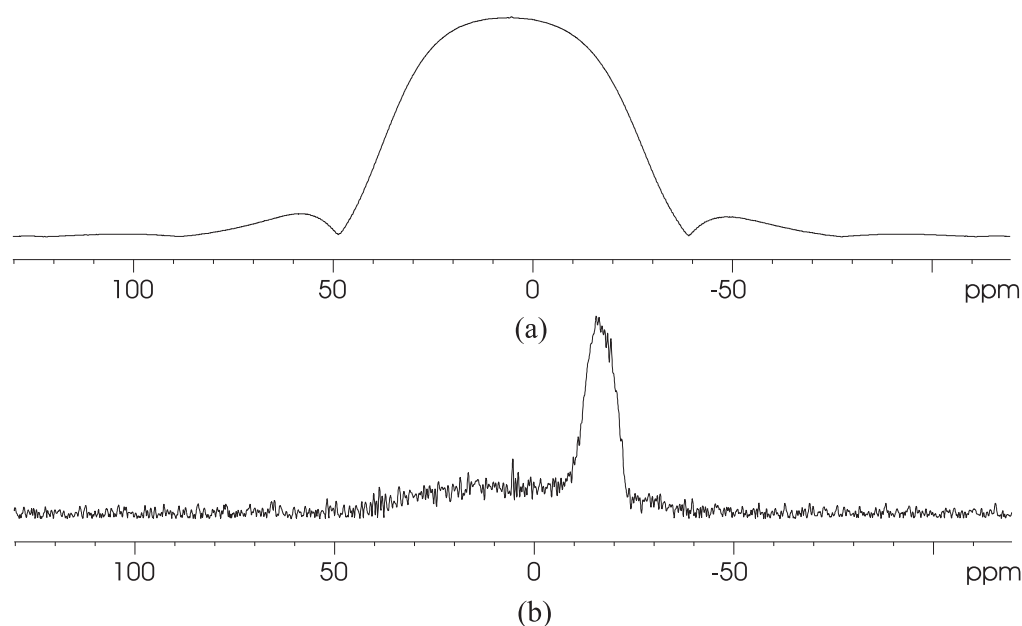


Figure 3.4: One dimensional image of the (a) NMR tube filled with water and (b) of the dihydride after the laser flash; showing that it is indeed formed within the coil region. The “hump” in the active region is mainly due to non-deuterated protons in the benzene solvent.

3.3.2 Optical assembly

The spectrometer was fitted with a special probe equipped for *in situ* photolysis [173], also designed by colleagues at York. For the single flash experiment, an MSX-250 pulsed XeCl excimer laser radiating 308 nm UV light was employed. The flash lasted for 12 ns and the flash-to-flash variability was known to be less than 1 ns. The specification sheet of the laser quotes a beamwidth of 12×6 mm and a beam divergence of 2×2 mrad; and the power per pulse was measured to be 32 mJ. The single pulse of UV light was then directed into the probe of the spectrometer using a carefully aligned assembly of quartz prisms, an arrangement resembling a periscope. The UV light was directed to fall in the active region of the NMR tube, lying directly below the RF coils; this is made possible by precise engineering of the probe head. The laser is triggered by a control signal, initiated from within the pulse programme. There is also a small ($\approx 10 \mu\text{s}$) trigger-flash delay and the tomography pulse or filtration sequence can “wait” to take into account this small time interval. The dihydride is formed within the coil region because of the optical positioning; this is also confirmed by a one dimensional image [35] of the dihydride taken after the laser flash, showing the relative positions of the hydride

and the active region and is shown in Figure 3.4. The experiment was performed in a darkened room, reducing the possibility of background photodissociation of the compound, ensuring that all dihydride formation is initiated by the UV laser.

For extended durations of irradiation, a Kimmon IK3202R-D 325 nm He-Cd 27 mW CW UV laser was used; the optical assembly was left unchanged. To enable a pre-determined amount of laser light to reach the sample, the CW laser was employed in conjunction with a Vincent Associates Uniblitz VMM-D1 shutter, which was opened and closed from within the logic of the pulse programme. The response time of the shutter was 1.5 ms; and since our CW experiments involved minimum irradiation times of 60 ms, errors due to shutter timing were negligible.

3.3.3 Dihydride spectra

The NMR spectra for different pulse sequences, in conjunction with a single flash of the pulsed laser, are shown in Figure 3.5. The GARP broadband decoupling sequence [190] was applied throughout signal acquisition to remove couplings to ^{31}P nuclei. For the initialization experiment, the NMR tube must not contain any residual $\text{Ru}(\text{H})_2(\text{C}\text{O})_2(\text{dppe})$ *before* the flash is triggered. This is verified by applying a simple 90_y hard pulse prior to irradiation, no signal is seen, suggesting that no dihydride exists before the flash or its concentration is too minute to be detectable. The resulting spectrum, which is essentially noise, is shown in part (a) of the figure. Figure 3.5(b) is the result of performing instantaneous PASADENA experiment depicted in Figure 3.2(b), a selective Jump-and-Return sequence applied soon after the flash. The spectrum shows the expected pair of anti-phase doublets, in accordance with (2.47). Part (c) of the figure, shows the spectrum resulting from the sequence (3.34), but this time also includes the filtration sequence before the Jump-and-Return. The result is very similar, and in fact apparently indistinguishable from (b), suggesting that the *para*-hydrogen addition is clean, and that error terms mixing in with the singlet are very small. Modifying the filtration sequence by reducing the duration of each gradient to $1/(2\delta)$, results in only the I spin being observed. Part (d) of Figure 3.5 shows exactly this, authenticating the right multiplet as belonging to I . With the identity of the spins now revealed, we can translate the spectral pattern in Figure 3.5(b), (read



Figure 3.5: NMR spectra from the single flash experiment. The spectrum in (a) is the output from a 90_y hard pulse *before* the laser flash; (b) is the spectrum from the pulse sequence (3.31), *i.e.*, without the filtration; (c) is acquired after the sequence (3.34), inclusive of the filtration; while in (d), the length of each gradient is halved, exciting only the I spin; and finally, (e) is the spectrum obtained from the sequence (3.31), but without the initial 90_{45} hard pulse.

leftwards as down, up, up, down), into the signal vector $\{-, +, +, -\}$ ⁴, where the leftmost entries *in the vector* correspond to spin I and the rightmost to S . For example, with this convention the spectrum (d) translates to $\{+, -, 0, 0\}$. In short, the pair of lines *appearing* to the right in our displayed spectra belong to spin I and correspond to the two leftmost positions in the signal vector. Finally, part (e) of the figure shows the spectrum obtained from the pulse sequence $[t_d \ 90_{-x}]$, dropping out the first hard pulse from (3.31) and the result is apparently indistinguishable from (b). Hard pulses are irrelevant for the singlet, indicating that the state prepared after the laser flash is indeed close to being a perfect Werner singlet. Our tomography results in Section 3.4, will in fact, state the exact component-wise breakup of the quantum state.

Figure 3.6 shows spectra from the delayed PASADENA experiments (Figure 2.5(b)), in which the selective detection pulse is postponed for a variable delay τ after the laser flash. The results are in complete agreement with (2.68), with the I multiplet remaining more or less unchanged (neglecting relaxation), and the phases of the component lines in the S multiplet varying sinusoidally, with the expected frequency of δ .

⁴I assume ‘+’ is upwards and ‘−’ is downwards.

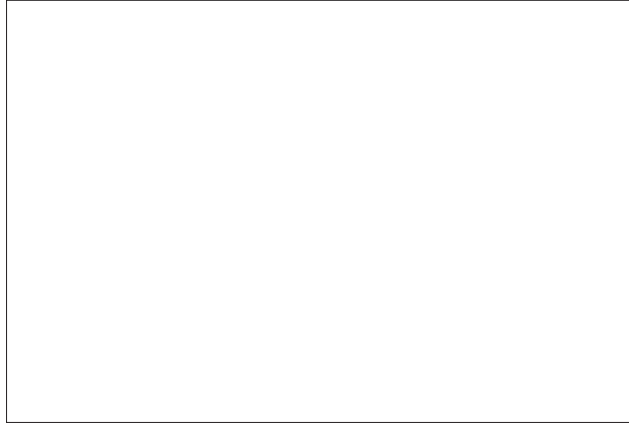


Figure 3.6: Spectra from delayed PASADENA, in which the selective detection pulse sequence is initiated with a variable delay τ after the laser trigger. The plotted spectra were obtained by systematically varying τ under computer control: increasing in steps of nearly $1/(4\delta) \approx 510 \mu\text{sec}$, from $3 \mu\text{s}$ in (a) to $2043 \mu\text{s}$ in (e). Multiplet I remains unchanged (ignoring relaxation), while the components of the S multiplet change phase in steps of $\pi/2$; going from (a) absorption $\{-, +, +, -\}$, to (b) dispersion $\{-, +, i, -i\}$, (c) negative absorption $\{-, +, -, +\}$ to (d) negative dispersion $\{-, +, -i, i\}$ and back to (e) absorption $\{-, +, +, -\}$. This cyclic variation of the phase occurs at a frequency δ .

3.3.4 Control experiment

The experimental spectra (Figure 3.5) are in almost perfect agreement with the theoretical predictions. However, we are interested in initializing the two qubit system in a pure state, and to find the exact purity, it is essential to know not only the form, but also the *intensity* of the signal. As absolute intensities are hard to come by in NMR, we need a reference spectrum with a *known* intensity. The thermal signal, specified in (2.39), is a readily available reference with an intensity deducible from first principles. Our control experiment provides this intensity reference and thereby calibrates the enhanced hyper-polarized signal strengths.

One straightforward means to implementing the control is allowing the highly polarized dihydride to relax to the thermal equilibrium state (2.37) and applying a hard 90_y pulse, followed by acquisition. Indeed this is a completely valid strategy, but the problem is that the amount of dihydride, $\text{Ru}(\text{H})_2(\text{C}\emptyset)_2(\text{dppe})$, formed from a *single* laser flash is much too small and, after relaxation, the thermal signal is too weak to be detected. For example, assume we make a pure state in our initialization experiment, then if the thermal signal from a single laser flash is to be detected over and above the noise floor, the signal-to-noise ratio for the pure-state spectrum should be of the order of 30000: this is something clearly not possible. Our spectra in Figure 3.5 show a signal-to-noise ratio of only about 40.

One way around this limitation is to increase the concentration of the dihydride by applying more flashes. The initialization experiment with F flashes⁵ is schematically shown in Figure 3.7. In practice, we applied 1000 laser flashes in total, thereby increasing the concentration of the dihydride a thousand-fold. Even then, the signal-to-noise of the thermal spectrum was not sufficient, and it was necessary to perform signal averaging [35]. We performed 3072 scans before a thermal spectrum with a reasonable signal-to-noise ratio was obtained. The control and enhanced spectra are shown side-by-side in Figure 3.8. The resulting thermal signal is a sum of S scans and for meaningful comparison with the *para*-hydrogen enhanced spectrum from a single flash, must be divided by $S \times F$. We can then compare the *para*-hydrogen with the properly rescaled thermal spectrum and determine the enhancement and hence the purity. This

⁵The notation F should not be confused with the identical notation I have used for the singlet fraction.

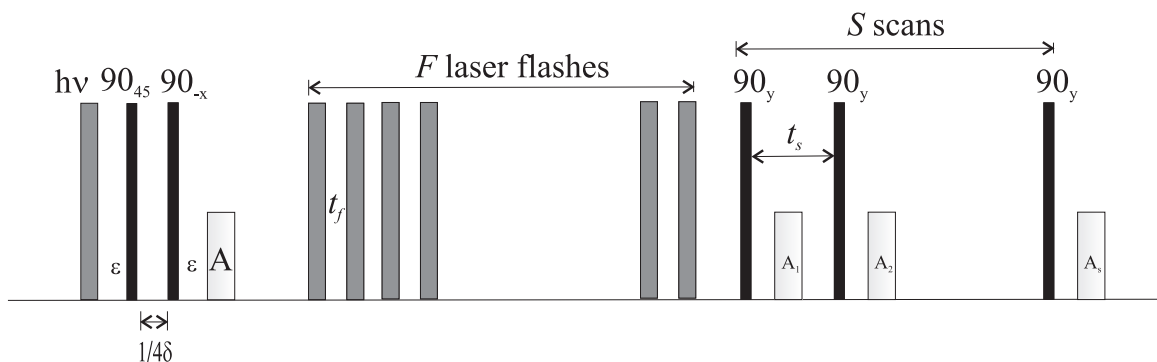


Figure 3.7: Schematic outline of the calibration experiment. The first laser flash, shown by a grey rectangle, produces $\text{Ru}(\text{H})_2(\text{C}\emptyset)_2(\text{dppe})$ which is detected and the signal acquired (A). Subsequently we apply F laser flashes producing F times as much dihydride. Adjacent flashes are separated in time by t_f . The thermal signal was measured by signal averaging S times (A_1 through A_s), and the averaged spectrum obtained after signal averaging, is in fact, the *sum* of the S transients. Two successive scans are separated by a delay of t_s .

naïve approach, however, yields an enhancement of about 77000, well above the theoretical maximum. The apparent discrepancy is addressed and resolved by an active volume argument and is the subject of the next subsection.

In the preceding discussion, we have assumed that F flashes produce F times as much $\text{Ru}(\text{H})_2(\text{C}\emptyset)_2(\text{dppe})$ than the amount produced by a single shot, or in other words, the precursor **I** is not *depleted*. Our collaborators, in fact, performed a ^{31}P quantitative experiment [35] to examine the extent of depletion, which turns out to be very small. The underlying concept of the quantitative experiment and results are outlined in Section 3.3.6.

An inter-flash delay t_f of 7 s is sufficiently long to allow *different* precursor molecules, which are subject to convective and diffusive motions, to cross the path of the laser beam, and be irradiated by successive laser flashes. This ensures that there is, more or less, a linear relationship between the amount of $\text{Ru}(\text{H})_2(\text{C}\emptyset)_2(\text{dppe})$ formed and the number of flashes [153]. As a matter of principle, the selected t_f should be large as compared to the characteristic timescales for diffusion and convection. Furthermore, successive scans are separated by about 20 s, which is greater than $5T_1 \approx 8.5$ s and so saturation effects [35] can also be safely ignored. With these values of t_f and t_s , the

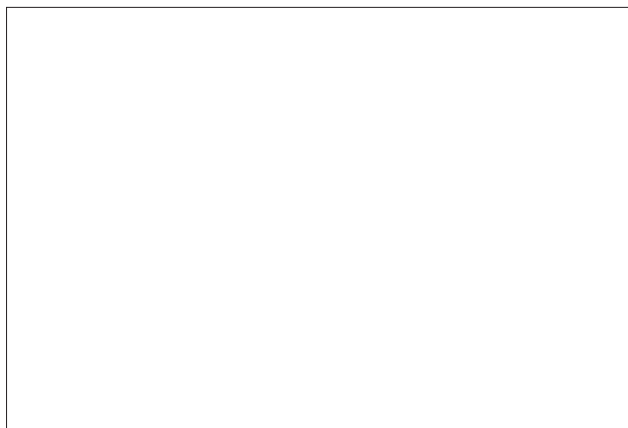


Figure 3.8: The *para*-hydrogen enhanced and calibration spectra of $\text{Ru}(\text{H})_2(\text{CO})_2(\text{dppe})$. The enhanced spectrum (a) is a single scan after a single laser flash, and is identical to Figure 3.5(b), while the calibration spectrum (b) is the sum of 3072 scans after 1000 laser flashes. The calibration spectrum has been divided by 3072000 and then multiplied by 30864 (the theoretical maximum enhancement) before plotting, so that the two spectra should show the same intensity. In fact the *para*-hydrogen enhanced spectrum (a) is even more intense than naïvely predicted.

total time required for the experiment is about 19 hours.

3.3.5 Active volume correction

Figure 3.5 shows the spectrum from a single laser flash alongside the calibration spectrum, which has been multiplied by $30864/(S \times F)$ before plotting. For an almost pure state the two spectra should be roughly the same size, but the *para*-hydrogen enhanced spectrum is significantly bigger than the thermal spectrum, resulting in an apparent enhancement about 2.5 times larger than the maximum possible. This discrepancy is explained by considering the fact that the NMR probe is not sensitive to the *entire* sample, but only to an “active” region, lying inside the RF coil (refer to Figure 3.4). Only the sample that lies within the active volume can be detected, the rest remains undetected, and therefore lies in what I call the “passive” region.

A single laser flash produces $\text{Ru}(\text{H})_2(\text{CO})_2(\text{dppe})$ lying wholly within the active region and therefore, *all* of it is detected and contributes to the enhanced signal. This is not true for the calibration signal. Applying the 1000 laser flashes takes about 2 hours during which the dihydride distributes itself throughout the entire volume of the

sample by diffusion and convection. As a result, the calibration spectrum does not record *all* of the dihydride present in the NMR tube, but only registers the fraction lying inside the active region; molecules in the passive region yield no spectrum. As a result, the calibration signal is attenuated by a factor V_f , the *active volume fraction*, corresponding to the ratio of the active to the total volumes. The true enhancement is therefore smaller than it appears, the correction factor being V_f . As expected the directly measured enhancement (that is, before correction) shows a linear dependence on the total sample volume (data is shown in our submitted work [153]), confirming our active volume hypothesis.

The active volume fraction can be estimated using simple geometrical considerations. Considering a ratio of lengths as a good substitute for a ratio of volumes, V_f can be estimated from the length of the RF coil and the depth of the NMR sample. In the experiment described, these lengths were measured⁶ to be 12.5 mm and 34 mm, resulting in an approximate fraction V_f of 12.5/34. This deduction of the V_f fraction, however, is prone to error, as it is based on an “all or none” assumption of the probe sensitivity, that is, *all* of the dihydride inside the active region and *none* in the passive region is detectable. But as Figure 3.4(a) shows, the sensitivity drops off smoothly near the edges of the RF coil, rather than in a sharp step-like manner. As a result, the sensitivity is not uniform even within the active region, and our estimated V_f remains, at best, only an estimate⁷ and addressing this should be a priority in future experiments.

3.3.6 Depletion of the precursor

The control experiment assumes that all flashes behave identically: having identical photon fluxes, quantum yields and more importantly, that the precursor (**I**) concentration is constant at all times during the experiment. This section considers the effects of depletion of the precursor molecules, ignoring any variability in the light pulses.

Under this assumption each flash delivers a *fixed* number of photons to the sample. Suppose this number is R . Each of the R photons can potentially affect the conversion of a precursor molecule to the dihydride, however the number of molecules converted

⁶The sample is long because this improves the homogeneity of the magnetic field by moving the susceptibility boundary away from the detection region.

⁷My rough guesstimate for the error in the active volume fraction would be 10–30%.

depends on the concentration of the precursor, $[C]$, existing just *before* the flash. A simple first order model for the conversion can be written as,

$$\frac{d[C]}{dF} = -AR[C], \quad (3.35)$$

where A is a rate constant independent of the concentration. What this constant signifies is that although the *absolute number* of photons converted will fall with each successive flash, the *fraction* of the molecules converted *per flash* remains constant. For example, the thousandth flash would convert a smaller number of precursor molecules to the dihydride than the first pulse, but in each case the fractional conversion would remain the same. Now suppose that each flash converts a constant 0.01% of the precursor. If depletion was not an issue, then 1000 flashes would convert $1000 \times 0.01\% = 10\%$ of the precursor, but taking depletion into account, we predict an overall conversion of,

$$1 - (1 - 0.0001)^{1000} \quad (3.36)$$

which is 9.52%, smaller than the 10% as expected. Thus the no depletion assumption *underestimates* the thermal signal and *overestimates* the purity of the *para*-hydrogen state by a factor of $10/9.52 = 1.05$, which is our depletion correction factor. In the hypothetical limit of an infinite precursor concentration, the rate of conversion $d[C]/dt$ becomes more or less independent of $[C]$ and the conversion acts as a pseudo zeroth order reaction in which the absolute number of molecules converted per flash *appears* to be constant. This is because the initial concentration of the precursor is so high and the conversion per flash so low, that $[C]$ does not substantially decrease on the application of successive flashes. Mathematically, this implies that all three parameters in the R.H.S. of (3.35) act like constants, resulting in a linear decrease in the precursor concentration (or linear increase in the dihydride concentration). These ideas are illustrated in Figure 3.9.

In fact, we carried out a simple experimental calculation to determine the extent of precursor depletion. The two phosphorus nuclei acquire different chemical shifts in **I** and **III**, [174], resulting in distinct ^{31}P signals for these compounds. This fact helps in performing a quantitative experiment⁸, determining the relative concentrations of the

⁸The experiment involves direct ^{31}P detection; uses 10000 scans (the large number of scans are needed because of the low concentrations of the precursor), an inter-scan delay of 20 s and proton-decoupling turned on only during acquisition, preventing build-up of artificial intensities due to the

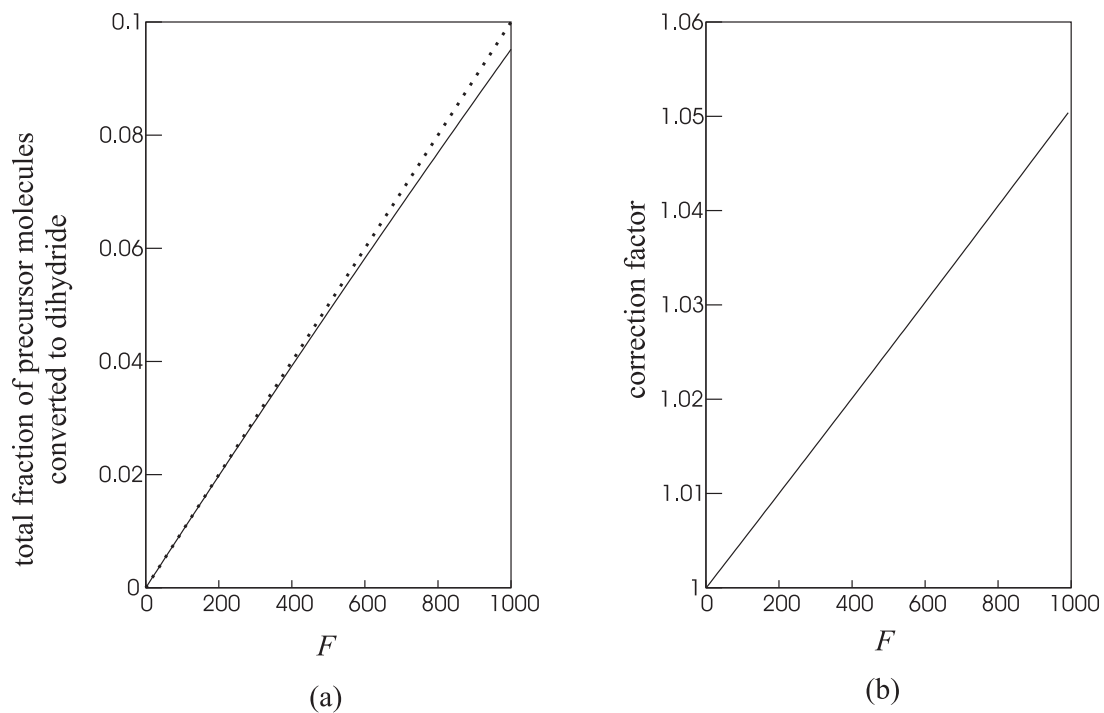


Figure 3.9: Depletion of the precursor: in (a), the solid line shows the overall fraction of molecules converted, $(1 - (1 - x)^F)$, as a function of F . The dotted line is a plot of Fx , the total fraction of molecules converted for a hypothetical pseudo-zero order conversion and coincides with the depletion curve for small values of Fx . Part (b) shows the depletion correction factor, $Fx / (1 - (1 - x)^F)$, as a function of F . The fraction converted per flash x is assumed to be 0.01%.

two species after F laser flashes, and therefore, the extent of conversion of **I** to **III**. One such experiment (see footnote) showed that after 1000 flashes, about 4.46% of **I** was converted into **III**. Suppose that after one flash, a constant fraction x of the precursor is converted, then after 1000 flashes, the fraction converted is $(1 - (1 - x)^{1000})$, and equating this with the experimentally determined fraction of 0.0446, yields a conversion per flash x of $4.56 \times 10^{-3}\%$. Therefore, to correct for the effect of depletion, the *para*-hydrogen enhancement must be divided by,

$$\frac{1000 x}{(1 - (1 - x)^{1000})} \approx 1.023. \quad (3.37)$$

3.4 Data processing

An estimate of the purity of the two qubit (Werner singlet) state is,

$$\frac{P}{T \times 1.023} \times S \times F \times V_f \times \frac{1}{30864}, \quad (3.38)$$

where P is *some kind* of intensity of the enhanced *para*-hydrogen signal and T is *some measure* of intensity of the thermal signal acquired from the multi-scan, multi-flash control experiment. This section considers the data processing steps we employed in interpreting the spectra and determining the appropriate values of P and T for the purity calculation and state tomography.

3.4.1 Peak integration

The enhanced and control spectra were processed [191, 192] using home-written software⁹ and analyzed by integration: measuring areas between the absorptive Lorentzian peaks and a flat, zero mean baseline. The integrals are a more reliable measure of signal intensity than line heights due to two reasons. *First*, line heights critically depend

Nuclear Overhauser Effect during inter-scan delays.

⁹The data processing was done on a Sun Blade 1000 machine running Solaris OS. Spectra were acquired on a Bruker spectrometer at the University of York, and the data was then converted and adapted for use on the Blade machine. I wrote the programmes and scripts for data conversion, manipulation, J matching, doubling and integration in C and in AWK [193]. Other processing tasks such as zero-filling, Fourier and inverse Fourier transformations and plotting/display were performed using software written by my supervisor. Finally, offset and baseline correction were done with Mathematica and the Grace [194] data visualization package.

on the *frequency resolution* [191, 192] of the spectrum, which is quite poor for our raw spectra; poorly digitized spectra often resulting in underestimates of the height. *Second*, the total integral under a band-unlimited frequency domain spectrum is equal to the first point in the time domain FID (besides a normalization factor) [195], and is therefore independent of RF inhomogeneities and T_2 relaxation effects.

However, prior to integration, it is important to deal with some spectral artifacts. A baseline offset or a sloping baseline introduces errors; the effect is illustrated in Figure 3.10. I employed second order curve fitting (baseline correction) prior to integration. Other important factors to consider are the need for properly phased, absorptive mode spectra and the number and extent of data points [191], over which the peaks are integrated. The integrals also fluctuate due to noise and standard errors on the integral values were measured by calculating the variance over regions of baseline noise of identical spectral widths.

3.4.2 J processing

In the *para*-hydrogen experiment, the integrals of the anti-phase multiplet partially cancel due to overlap. Any peak integrals we directly measure, even after removing all the artifacts discussed above, will therefore be an underestimate. There is however, one way of reducing the overlap by “dragging” apart the peaks; the method is called *J-doubling* [196, 197]. In summary, the data processing steps involved in accurate peak integration comprised the following steps. (I have described the reduction in peak integrals due to overlap and *J*-doubling in considerable detail in Appendix ?? and here I give only the major results.)

1. We excised a small section from the overall spectrum that contained the dihydride peaks.
2. The excised spectrum was inverse-Fourier transformed to yield a time domain signal and zero-filled [191, 192] to increase the apparent frequency resolution.
3. We implemented a computer algorithm scanning trial J' values, looking for a global minimum in the integrals of absolute J' -modulated spectra. This step results in an estimate for the true splitting, J . A plot of integrals of the J' -modulated spectra is shown in Figure 3.11.

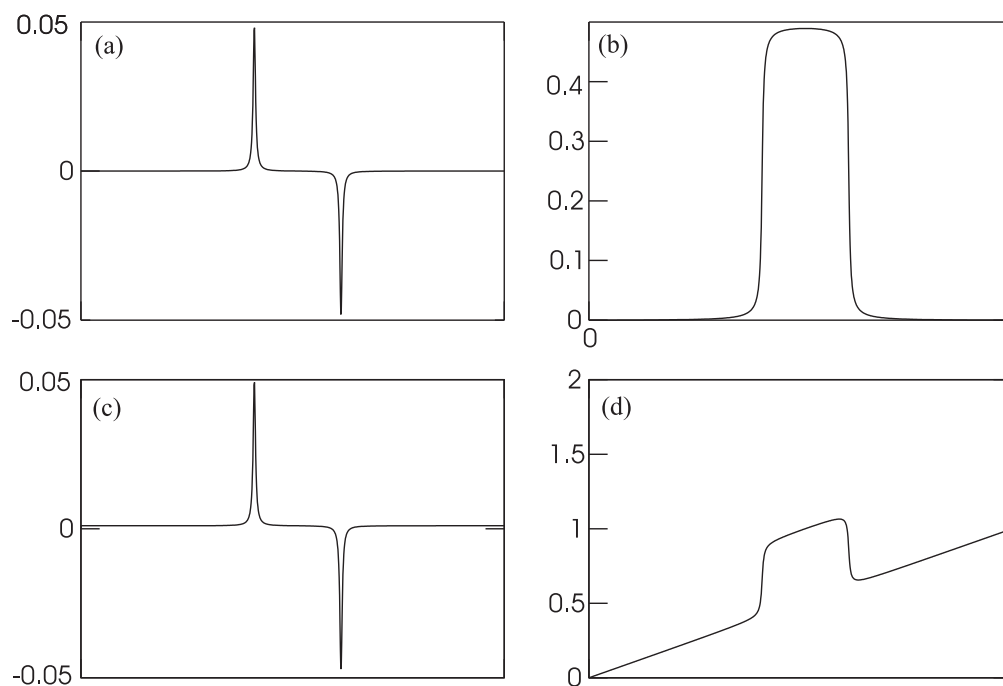


Figure 3.10: Effect of a baseline zero-offset on the peak integrals. The spectrum in (a) comprises an ideal anti-phase peak (maximum and minimum are between $\approx \pm 0.05$) and (b) is the corresponding integral (obtained by summing up all previous points, starting from the left edge of the spectrum). The integral is uniformly zero in the baseline region, reaches a maximum ≈ 0.5 in the region between the peaks and drops back to zero after the second peak. In (c), the spectrum (a) is raised upwards by a small amount (≈ 0.001), and (d) shows the corresponding integral, indicating that now, even the baseline region has a positive integral which additively interferes with the peak integral. In this case, the peak integrals will be an over-estimate and baseline correction becomes necessary.

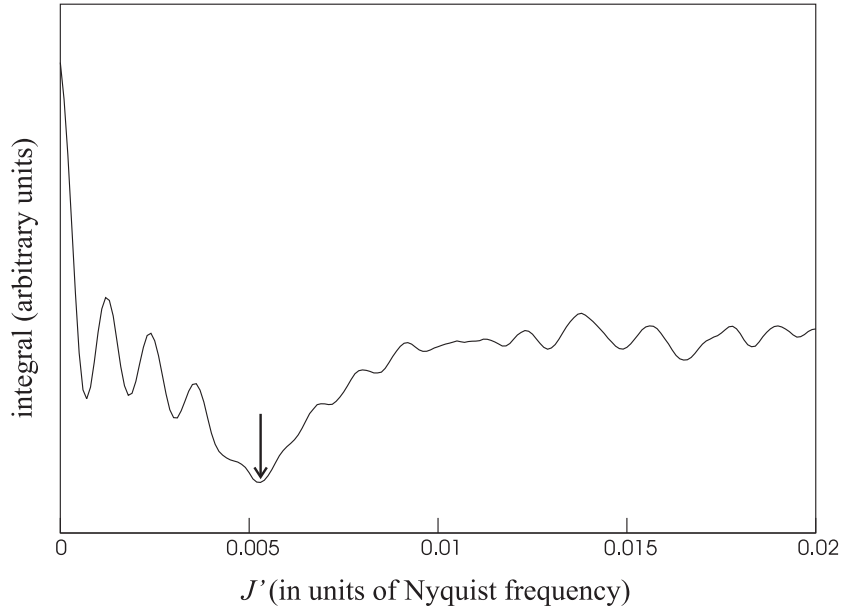


Figure 3.11: Results of the computer programme searching for the global minimum in the integrals of absolute J' modulated spectra (Appendix ??). The trial values, J' are given in units of the Nyquist frequency. The global minimum of the integral plot is indicated by an arrow and corresponds to the matched $J' = J = 0.0054$ value.

4. The matched J value is then used to double the original spectrum. We double four times, substantially reducing the effects of overlap but also degrading the signal-to-noise ratio. The successively doubled spectra are shown in Figure 3.12.
5. Peak integrals are determined from the doubled spectra and rescaled, taking into account the number of doublings employed. These rescaled integrals are given in Table 3.3. As expected, after doubling a sufficient number of times, the overlap disappears and the integrals no longer destructively interfere. As a result the measured peak integrals increase and the effect is shown in Figure 3.13. Another important consequence of the doubling is to reduce the artificial imbalance between the peaks within a doublet. We take the average between the statistically indistinguishable peaks from the $m = 4$ spectra, resulting in accurate I and S peak integrals, which in this experiment are 8.0310 ± 0.1936 and 7.4328 ± 0.1936 (calculated from the entries in the last row in Table 3.3).

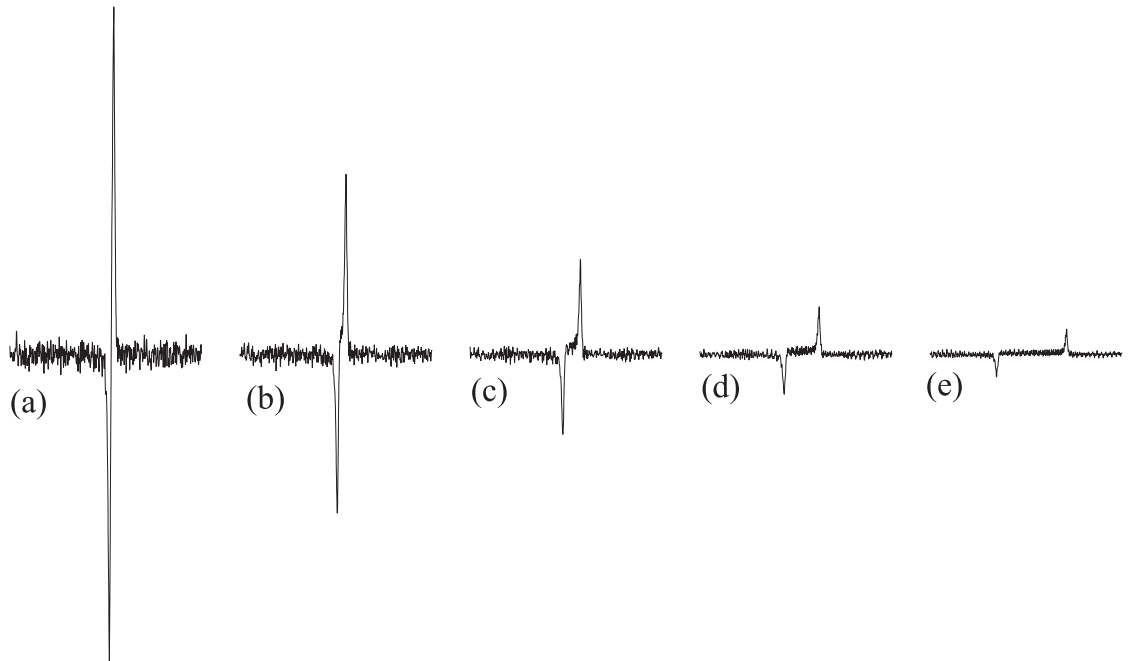


Figure 3.12: Effect of J -doubling. Only the left (S) peak is shown. Part (a) shows the original spectrum ($m = 0$), and (b)–(e) show the successively doubled spectra ($m = 1, 2, 3, 4$). The spectra are drawn to the same vertical scale and the signal heights are seen to drop by roughly half at each stage.

m	S_l	S_r	I_l	I_r	SD
0	5.9381	6.8250	6.3643	6.8375	0.075
1	6.6281	7.3230	7.0029	7.3095	0.128
2	7.1190	7.2129	7.5793	7.2402	0.136
3	7.2967	7.0603	8.0698	7.3507	0.090
4	7.6220	7.2544	8.0594	8.0027	0.194

Table 3.3: Integrals calculated from the spectra, where m is the number of J -doublings employed. The subscripts “l” and “r” refer to the left and right lines in the I and S spin peaks.

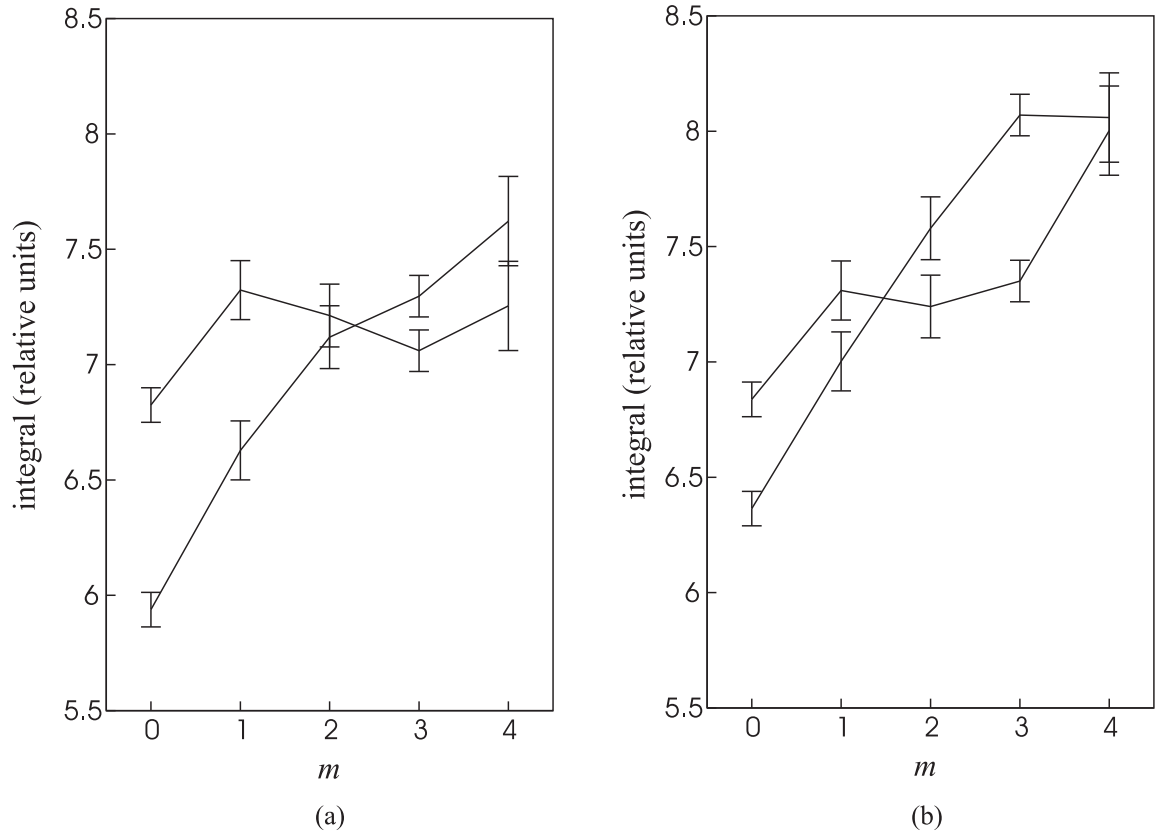


Figure 3.13: Peak integrals as a function of the number of J -doubling steps, m . The plot (a) shows the integrals for the S spin and (b) shows the integrals for the I spin. The integrals, in general, increase with increasing m and for $m = 4$, the peak integrals within a doublet become statistically indistinguishable.

3.4.3 State tomography results

The I and S integrals of the processed spectra are then normalized by multiplying by the factor $(S \times F \times V_f)/(T \times 1.023 \times 30864)$, where T is the “raw” average integral under each of the four peaks, determined after baseline correction but without any J -processing. In our case, we measured a T of 303.12 ± 4.44 . The other experimental parameters were: $S = 3072$, $F = 1000$ and $V_f = 12.5/34 = 0.368$. This calculation gives us the p and q coefficients in the state representation (3.3), therefore achieving state tomography. However, we prefer to express the state in the form, (3.2) and use the equations (3.6)–(3.7) to determine the singlet and triplet fractions (a, b, c) from p and q . For example, in the particular experiment I am discussing, the I spin normalized integral corresponds to $q = -8.0310 \pm 0.1936$ and the S spin integral corresponds to $p = -7.4328 \pm 0.1936$. For a pure S_0 , we expect $p = q = -1$, however in our case, the multiplets are slightly imbalanced, resulting in unequal fractions of the triplets. Using (3.6)–(3.7), the exact state characterization is,

$$a = 0.9371, \quad (3.39)$$

$$b = 0.0448, \quad \text{and} \quad (3.40)$$

$$c = 0.00905, \quad (3.41)$$

not identical but very similar to a Werner singlet with balanced triplets. The resulting density matrix is portrayed in Figure 3.14 and has a concurrence and entanglement of formation of 0.874 and 0.822 respectively.

If we *assume* that our quantum state is a Werner singlet, $(1 - \varepsilon)\mathbf{1}_4/4 + \varepsilon S_0$, with a singlet fraction equal to the a calculated above, then the polarization of the state is,

$$\varepsilon = 0.916 \pm 0.2, \quad (3.42)$$

which I call the *effective purity* and is consistent with a spin temperature of 6.4 mK or an effective magnetic field of 0.45 MT at room temperature.

3.5 CW experiments

This section discusses our isotropic PASADENA experiment utilizing the CW laser. The spectra from extended hydrogenation periods of 60 ms and 300 ms, in the presence

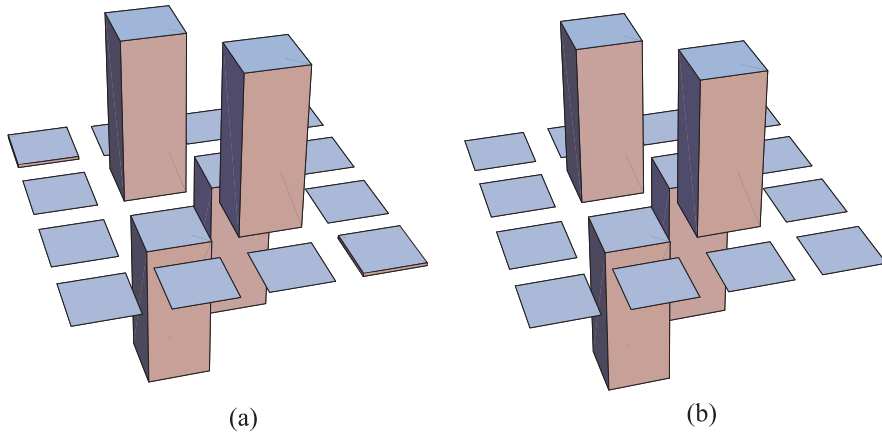


Figure 3.14: Results from quantum state tomography, showing the density matrices from (a) the state generated by the pulsed laser, compared with (b) a perfect singlet. Despite small non-zero amounts of $T_{\pm 1}$ in (a), the overall density matrices are very similar. The elements in the bar chart represent magnitudes of the elements in the density matrix written in the conventional $\{|\alpha\beta\rangle, |\alpha\beta\rangle, |\beta\alpha\rangle, |\beta\beta\rangle\}$ order. For example, the top left element in the graph represents the magnitude of the element $\langle\alpha\alpha|\rho|\alpha\alpha\rangle$ and so on. All elements in the matrix are real.

of the MLEV-16 isotropic mixing sequence are shown in Figure 3.15. These spectra show that the doubly anti-phase character of the spectrum is maintained, indicating that the mixing sequence is very good at preserving the form of the singlet. However, there is one problem: naïvely one would expect the 300 ms spectrum to be five times bigger than the 60 ms spectrum, but it is not quite so large. We attribute this discrepancy to the relaxation of the highly polarized state, which can cause pronounced signal loss for extended durations of hydrogenation. A rough calculation gives a value of about 0.6 s for the relaxation constant. It is important to note that this value does not correspond to the single quantum T_2 relaxation normally quoted in NMR, but rather it corresponds to a complicated decay of an isotropic state towards the maximally mixed state in the presence of a mixing sequence; this is sometimes described as “spin-lattice relaxation in the rotating frame”, $T_{1\rho}$ [187]. Quantum state tomography results are outlined in Table 3.4 and the density matrices for the CW experiment are depicted in Figure 3.16.



Figure 3.15: Spectra from the isotropic PASADENA experiment, employing MLEV-16 isotropic mixing. The spectrum in (a) is acquired after 60 ms of laser irradiation and (b) shows the spectrum obtained after 300 ms of irradiation. Naïvely one would expect (b) to be five times bigger as compared to (a), however the signal intensities are smaller than expected. For comparison, (c) is a plot of the spectrum (a) multiplied by five.

	60 ms	300 ms
<i>a</i>	0.9159	0.8191
<i>b</i>	0.0565	0.0687
<i>c</i>	0.0138	0.05615
ε	0.8879	0.7588

Table 3.4: Tomography results from isotropic PASADENA experiments, involving CW irradiation for 60 and 300 ms; ε is the effective purity.

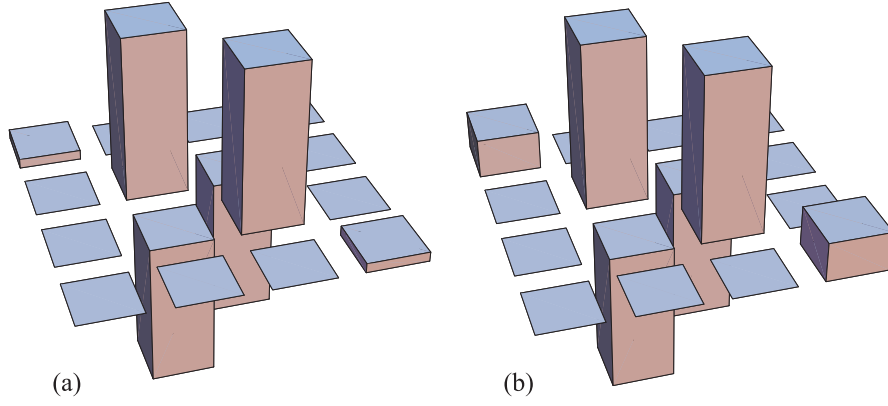


Figure 3.16: Tomography results from the CW data, showing the density matrices after (a) 60 ms and (b) 300 ms irradiation. Build-up of significant $T_{\pm 1}$ error terms is evident from (b). Interpretation and labelling of this figure are identical to those in Figure 3.14.

Chapter 4

Implementation of quantum computation with the pure state quantum computer

Chapter 3 described the experimental preparation of a two qubit pure quantum state—the qubits are the two ^1H nuclei in the organometallic compound $\text{Ru}(\text{H})_2(\text{C}\text{O})_2(\text{dppe})$, and the nuclei inherit the nuclear spin singlet state, derived from pure *para*-hydrogen. At this juncture, the natural question to ask is, having *prepared* a pure state, can we go one step further and actually *use* this as an initial state for a quantum information processing task, such as for implementing a quantum algorithm? The answer is yes and this chapter describes our experiments achieving this.

The extremely high purity of the system, quite naturally, obviates the need for assembling pseudopure states, a process requiring non-unitary operations and generally lengthy or complicated pulse sequences. Our experiments [59, 154] constitute the first implementation of quantum algorithms in liquid state NMR using pure initial states. As a result, they do not prepare pseudopure states, instead they initialize the system directly in an essentially pure quantum state (also lying above the entanglement threshold). In related work, Hübler *et al.* implemented [152] the Deutsch algorithm on a *para*-hydrogen derived two qubit system, although with much smaller purities, $\varepsilon \approx 0.1$. Our implementations extend their results, to almost perfectly pure quantum states, with ε very close to 1. Furthermore, in addition to achieving high purity and the possibility for distilling entanglement [135], our experiments are unique in the sense

System NMR parameters	
Ru(H) ₂ (CO) ₂ (dpae)	
resonance frequencies	−7.61 and −7.22 ppm
δ	160 Hz (on the 400 MHz spectrometer)
¹ H T_1 (single quantum)	1.9 s
¹ H T_2 (single quantum)	0.67 s
² J_{HH}	4.8 Hz

Table 4.1: Important NMR parameters of Ru(H)₂(CO)₂(dpae) used in the implementation of Grover’s search.

that they prepare pure states *on demand*; our laser flash acts as a convenient switch, enabling us to generate the initial state, as and when desired.

In this chapter, I describe the implementation of two quantum algorithms using pure initial states. They are solving Deutsch’s problem of distinguishing between constant and balanced functions and performing Grover’s search on an unstructured database of four quantum states. For the two algorithms, we employed two different molecular systems: for Deutsch’s algorithm, we used Ru(H)₂(CØ)₂(dppe)—a chemical system with which we are quite familiar by now—and for Grover’s search, we used its closely related arsenic analogue, Ru(H)₂(CO)₂(dpae), where dpae is 1,2-bis(diphenylarsino)ethane. The important NMR parameters of the latter compound, whose structure is also shown in Figure 2.3, are summarized in Table 4.1.

Comparing the NMR parameters for Ru(H)₂(CO)₂(dpae) with Ru(H)₂(CØ)₂(dppe) (see Table 3.2), two results are obvious: *first*, the Ru(H)₂(CO)₂(dpae) has a slightly longer T_2 relaxation time, resulting in better decoherence properties and *second*, the frequency separation is about three times smaller in the “dpae” than in the “dppe” and this puts more stringent requirements on spin selective pulse sequences in the “dpae” system. These properties are important in evaluating the suitability of a molecular system for NMR quantum computing, and are captured by the ratios (δ/J) and $(J/(1/T_2))$: a system is suited for quantum information processing, if the condition $\delta \gg J \gg 1/T_2$ is satisfied. These characteristic ratios for the two molecules are compared in Table 4.2, indicating that the “dpae” has slightly better decoherence and

Parameter	“dppe”	“dpae”
δ/J	106.96	33.33
$J/(1/T_2)$	2.67	3.22

Table 4.2: Frequency separation, splitting and decoherence parameters for the “dppe” and “dpae” compounds.

worse frequency selectivity properties.

However, there is one clear cut advantage of using the $\text{Ru}(\text{H})_2(\text{CO})_2(\text{dpae})$ system: the initial state can be prepared with a purity indistinguishable from one; our measurements indicate a purity of $\epsilon \approx 1.06 \pm 0.2$. Thus, we can describe our initial states as being pure, without further qualification.

This chapter is organized as follows. Section 4.1 describes the Deutsch algorithm and Section 4.2 takes up Grover’s search with the pure state quantum computer. Experimental imperfections are visible in our spectra, and these can be roughly explained using a simple model based on representing quantum operations in terms of a family of Kraus operators. Appendix ?? exemplifies the use of this model, in context of the Deutsch spectra. The following two sections, more or less, reproduce our published and submitted works, [59] and [154], and so include brief discussions of many topics I have already discussed in previous chapters.

4.1 Deutsch’s algorithm with pure quantum states

A published version of this Section can be found on the e-print server:

<http://www.arxiv.org/quant-ph/0406044>.

4.2 Grover’s quantum search with pure quantum states

A published version of this Section can be found on the e-print server:

<http://www.arxiv.org/quant-ph/0407091>.

Chapter 5

Practical implementation of twirl operations

Entanglement is an important resource in the quantum setting and has been introduced in Chapter 1. Communication protocols, such as quantum teleportation [109, 110], work optimally, when they use maximally entangled pure states. For two qubits, these states are well known and are simply the four Bell states, given as $|\phi^\pm\rangle = (|00\rangle \pm |11\rangle)/\sqrt{2}$ and $|\psi^\pm\rangle = (|01\rangle \pm |10\rangle)/\sqrt{2}$. In the standard teleportation experiment, Alice and Bob share a pair of maximally entangled pure states and the pre-existing entanglement, in fact, constitutes a noiseless quantum channel. In real life situations however, the channels are never perfect. The pure states are subject to decoherence and degrade into mixed states, entailing a decrease in both the purity and the entanglement. Entanglement concentration or purification protocols [202, 203] then pick up these degenerated states and recover both the lost purity and entanglement, accompanying a decrease in the ensemble size [204]. The first step in most of these protocols is the “twirl” operation which converts an arbitrary mixed state ρ' , not maximally mixed, into the Werner state ρ_ε , (1.69). A useful fidelity measure [202] for such states is their most significant overlap with the maximally entangled state,

$$F(\rho) = \max \langle \psi | \rho | \psi \rangle, \quad (5.1)$$

where the maximum is taken over all four Bell states. It is well known that entanglement can be distilled from the mixed ρ whenever the state fidelity $F > 1/2$ [202]. Without loss of generality, we can also assume that the dominant term in ρ is the singlet state $|\psi^-\rangle$; the fidelity F then becomes the overlap of the state with the singlet,

which I have referred to as the singlet fraction, (1.84). An equivalent parametrization of ρ_ε can thus be made in terms of F ,

$$\begin{aligned}\rho_W = & F|\psi^-\rangle\langle\psi^-| \\ & + \frac{1-F}{3}(|\psi^+\rangle\langle\psi^+| + |\phi^+\rangle\langle\phi^+| + |\phi^-\rangle\langle\phi^-|),\end{aligned}\tag{5.2}$$

the correspondence between the polarization ε of the Werner singlet and its singlet fraction being given as

$$F(\rho_\varepsilon) = \frac{1+3\varepsilon}{4}.\tag{5.3}$$

It can be checked that for the maximally mixed state $\varepsilon = 0$ and $F = 1/4$; whereas for the pure singlet $\varepsilon = 1$ and $F = 1$.

Consider a mixed state ρ' which satisfies two properties: *first*, it is not maximally mixed and *second*, it has a non-zero singlet fraction F . The twirl operation would take such a state to ρ_ε , while conserving the singlet fraction,

$$\rho' \longrightarrow \rho_\varepsilon, \quad \text{such that}\tag{5.4}$$

$$F(\rho_\varepsilon) = F(\rho').\tag{5.5}$$

The restraints on ρ' simply arise from the fact that maximally mixed states remain unchanged under all quantum operations, and that ρ' must have a non-zero singlet fraction because the twirl sequence does not *create* new singlet, rather it only *preserves* the singlet, while averaging out all other terms, converting them effectively to the maximally mixed state. In other words, the twirl sequence “Wernerizes” the input state, by letting the singlet pass unscathed, while scrambling other terms into the maximally mixed state.

We have already come across the partial twirl in Section 3.1 in context of preparing a state for one-shot tomography. This chapter discusses the full twirl: the different ways of practically implementing the operation, especially on an ensemble quantum computer. Section ?? introduces the implementation. Twirling is a kind of state averaging and Section ?? discusses this concept for a single qubit while Section ?? extends these ideas to the two qubit case. Finally, a step-by-step NMR implementation is discussed in Section ?? and then I conclude in Section ??. This material is closely based on our submitted manuscript, [205].

An updated version of this chapter can be found on the e-print server:

<http://www.arxiv.org/quant-ph/0409142>.

Chapter 6

Purity sharing

Preceding chapters dealt with different aspects of our *para*-hydrogen derived two qubit NMR quantum computer. Scaling up the prototype computer to larger-sized systems is important if we wish to address more challenging and practically useful mathematical problems. In this spirit, one can come up with different ideas for extending the size of our quantum computer. Some of these ideas seem promising but may prove quite difficult to implement in practice.

1. For example, we can envisage a molecule (like an unsaturated organic polymer) which has multiple sites where H_2 molecules can add forming a $2\mathbf{M}$ qubit quantum computer, \mathbf{M} being the number of dihydrogen molecules.
2. Another scheme can be visualized, involving the *transfer* of purity from the two pure hydrogen qubits onto other weakly polarized qubits. After the polarization transfer, the hydrogens are allowed to detach from the molecule and their place is taken up by fresh, pure qubits and the transfer step is repeated. In this manner, purity can be “pumped” into the molecule. This scheme to some extent *resembles* the method of algorithmic cooling [96] already mentioned in Section 1.2.4.
3. Both of the above ideas involve bringing purity into the molecule from outside. We can also think of another scenario: suppose we are *given* a molecule with $2\mathbf{M}$ pure or nearly pure qubits, derived from \mathbf{M} *para*-hydrogen molecules. Instead of “importing” more purity into the molecule, we can consider the question of *sharing* out the purity on $k > 2\mathbf{M}$ qubits. The question that I investigate in this chapter is whether this sharing can be carried out, *while remaining above the*

entanglement threshold. This question is related to purity compression strategies outlined by Schulman and Vazirani [94], but while the latter schemes *concentrate* purity onto a smaller number of spins, what I consider here is “diluting” or *sharing* out this purity onto a larger quantum subspace.

An updated version of this chapter can be found on the e-print server:
<http://www.arxiv.org/quant-ph/0509036>.

Bibliography

- [1] A. Abragam, *The Principles of Nuclear Magnetism*, Clarendon Press, Oxford, 1961.
- [2] R. R. Ernst, G. Bodenhausen, and A. Wokaun, *Principles of Nuclear Magnetic Resonance in One and Two Dimensions*, Clarendon Press, Oxford, 1987.
- [3] M. H. Levitt, *Spin Dynamics: Basics of Nuclear Magnetic Resonance*, John Wiley and Sons, 2001.
- [4] R. Freeman, *Spin Choreography: Basic Steps in High Resolution NMR*, Oxford University Press, Oxford, 1998.
- [5] R. Freeman, *A Handbook of Nuclear Magnetic Resonance*, Longman Scientific and Technical, 1988.
- [6] J. Cavanagh, W. J. Fairbrother, A. G. Palmer, and N. J. Skelton, *Protein NMR Spectroscopy*, Academic Press, 1996.
- [7] P. Hore, J. A. Jones, and S. Wimperis, *NMR: The Toolkit*, Oxford Chemistry Primers, Oxford, 2000.
- [8] M. A. Nielsen and I. L. Chuang, *Quantum Computation and Quantum Information*, Cambridge University Press, 2000.
- [9] C. H. Bennett and D. DiVincenzo, *Nature* **404**, 247 (2000).
- [10] I. I. Rabi, *Phys. Rev.* **51**, 652 (1937).
- [11] D. P. DiVincenzo, *Fortschr. der Physik* **48**, 771 (2000).
- [12] A Quantum Information Science and Technology Roadmap, ARDA, <http://qist.lanl.gov>.

- [13] Phil. Trans. R. Soc. Lond. A **361** (2003).
- [14] J. A. Jones, Nature **421**, 28 (2003).
- [15] J. A. Jones, Prog. NMR Spectrosc. **38**, 325 (2002).
- [16] D. G. Cory et al., Fortschr. der Phys. **48**, 875 (2000).
- [17] D. G. Cory, A. F. Fahmy, and T. F. Havel, Proc. Nat. Acad. Sci. USA **94**, 1634 (1997).
- [18] L. M. K. Vandersypen and I. L. Chuang, Rev. Mod. Phys. (in Press), e-print: quant-ph/0404064 (2004).
- [19] L. M. K. Vandersypen, *Experimental Quantum Computation with Nuclear Spins in Liquid Solution*, PhD thesis, Stanford University, 2001.
- [20] L. M. K. Vandersypen, M. Steffen, G. Breyta, C. S. Yannoni, M. H. Sherwood, and I. L. Chuang, Nature **414**, 883 (2001).
- [21] J. A. Jones and M. Mosca, J. Chem. Phys. **109**, 1648 (1998).
- [22] I. L. Chuang, L. M. K. Vandersypen, X. Zhou, D. W. Leung, and S. Lloyd, Nature **393**, 143 (1998).
- [23] I. L. Chuang, N. Gershenfeld, and M. Kubinec, Phys. Rev. Lett. **80**, 3408 (1998).
- [24] J. A. Jones and M. Mosca, Phys. Rev. Lett. **83**, 1050 (1999).
- [25] J. A. Jones, M. Mosca, and R. H. Hansen, Nature **393**, 344 (1998).
- [26] D. Collins, K. W. Kim, and W. C. Holton, Phys. Rev. A **58**, R1633 (1998).
- [27] R. Das, T. S. Mahesh, and A. Kumar, Chem. Phys. Lett. **369**, 8 (2003).
- [28] K. Dorai, A. Kumar, and A. Kumar, Phys. Rev. A **63**, 034101 (2001).
- [29] T. S. Mahesh, K. Dorai, A. Kumar, and A. Kumar, J. Magn. Reson. **148**, 95 (2001).
- [30] S. Gulde, M. Riebe, G. P. T. Lancaster, C. Becher, J. Eschner, H. Haffner, F. Schmidt-Kaler, I. L. Chuang, and R. Blatt, Nature **421**, 48 (2003).

- [31] C. Cohen-Tannoudji, B. Diu, and F. Laloë, *Quantum Mechanics*, volume 1, John Wiley and Sons, 1977.
- [32] O. W. Sørensen, G. W. Eich, M. H. Levitt, G. Bodenhausen, and R. R. Ernst, *Prog. NMR Spectrosc.* **16**, 163 (1983).
- [33] I. S. Podkorytov, *Conc. Magn. Reson.* **9**, 117 (1997).
- [34] L. E. Kay and R. E. D. McClung, *J. Magn. Reson.* **77**, 258 (1988).
- [35] T. Claridge, *High-resolution NMR Techniques in Organic Chemistry*, Pergamon, 1999.
- [36] K. Schmidt-Rohr and H. W. Spiess, *Multidimensional solid-state NMR and polymers*, Academic Press, London, 1994.
- [37] D. D. Laws, H. L. Bitter, and A. Jerschow, *Angew. Chem. Int. Ed.* **41**, 3096 (2002).
- [38] C. S. Yannoni, M. H. Sherwood, D. C. Miller, I. L. Chuang, L. M. K. Vander-sypen, and M. G. Kubinec, *Appl. Phys. Lett.* **75**, 3563 (1999).
- [39] G. M. Leskowitz, N. Ghaderi, R. A. Olsen, and L. J. Mueller, *J. Chem. Phys.* **119**, 1643 (2003).
- [40] A. Kumar, K. V. Ramanathan, T. S. Mahesh, N. Sinha, and K. V. R. Murali, *Pranama J. Phys.* **59**, 243 (2002).
- [41] M. H. Levitt, *J. Magn. Reson.* **126**, 164 (1997).
- [42] M. Levitt, *Prog. NMR Spectrosc.* **18**, 61 (1986).
- [43] C. Counsell, M. H. Levitt, and R. R. Ernst, *J. Magn. Reson.* **63**, 133 (1985).
- [44] R. Tycko, *Phys. Rev. Lett.* **51**, 775 (1983).
- [45] S. Wimperis, *J. Magn. Reson. Ser. A* **109**, 221 (1994).
- [46] R. Freeman, T. A. Frenkiel, and M. Levitt, *J. Magn. Reson.* **44**, 409 (1981).
- [47] D. P. DiVincenzo, *Phil. Trans. R. Soc. Lond. A* **454**, 261 (1998).

- [48] J. A. Jones, R. H. Hansen, and M. Mosca, J. Magn. Reson. **135**, 353 (1998).
- [49] M. Price, S. S. Somaroo, C. H. Tseng, J. C. Gore, A. F. Fahmy, T. F. Havel, and D. G. Cory, J. Magn. Reson. **140**, 371 (1999).
- [50] M. Price, S. S. Somaroo, A. E. Dunlop, T. F. Havel, and D. G. Cory, Phys. Rev. A **60**, 2777 (1999).
- [51] N. Linden, H. Barjat, E. Kupce, and R. Freeman, Chem. Phys. Lett. **307**, 198 (1999).
- [52] M. D. Price, T. F. Havel, and D. G. Cory, New. J. Phys. **2**, 10.1 (2000).
- [53] K. Dorai, A. Kumar, and A. Kumar, Phys. Rev. A **61**, 042306 (2000).
- [54] D. G. Cory, M. D. Price, and T. F. Havel, Physica D **120**, 82 (1998).
- [55] L. Elmsley and G. Bodenhausen, Chem. Phys. Lett. **168**, 297 (1990).
- [56] M. Steffen, L. M. K. Vandersypen, and I. L. Chuang, J. Magn. Reson. **146**, 369 (2000).
- [57] N. Linden, B. Herve, R. J. Carbajo, and R. Freeman, Chem. Phys. Lett. **305**, 28 (1999).
- [58] M. S. Anwar, D. Blazina, H. A. Carteret, S. B. Duckett, T. K. Halstead, J. A. Jones, C. M. Kozak, and R. J. K. Taylor, Phys. Rev. Lett. **93**, 040501 (2004).
- [59] M. S. Anwar, J. A. Jones, D. Blazina, S. B. Duckett, and H. A. Carteret, Phys. Rev. A **70**, 032324 (2004).
- [60] P. Plateau and M. Guéron, J. Am. Chem. Soc. **104**, 7310 (1982).
- [61] E. M. Fortunato, M. A. Pravia, N. Boulant, G. Teklemariam, T. F. Havel, and D. G. Cory, J. Chem. Phys. **116**, 7599 (2002).
- [62] H. K. Cummins and J. A. Jones, New J. Phys. **2**, 6.1 (2000).
- [63] H. K. Cummins and J. A. Jones, J. Magn. Reson. **148**, 338 (2001).
- [64] J. A. Jones, Phys. Rev. A **67**, 012317 (2003).

- [65] J. A. Jones, Phil. Trans. R. Soc. Lond. A **361**, 1429 (2003).
- [66] A. Barenco, C. H. Bennett, R. Cleve, D. P. DiVincenzo, M. Margolius, P. Shor, T. Sleator, J. Smolin, and H. Weinfurter, Phys. Rev. A **52**, 3457 (1995).
- [67] D. Deutsch, A. Barenco, and A. Ekert, Phil. Trans. Roy. Soc. Lond. A **449**, 669 (1995).
- [68] W. H. Zurek, Phys. Rev. D. **26**, 1862 (1982).
- [69] J. McConnell, *Theory of Nuclear Magnetic Relaxation in Liquids*, Cambridge University Press, Cambridge, 1987.
- [70] J. A. Jones, Fortschr. der Physik **48**, 909 (2000).
- [71] G. Teklemariam, E. M. Fortunato, C. C. Lopez, J. Emerson, J. P. Paz, T. F. Havel, and D. G. Cory, Phys. Rev. A. **67**, 062316 (2003).
- [72] N. Boulant, T. F. Havel, M. A. Pravia, and D. G. Cory, Phys. Rev. A. **67**, 042322 (2003).
- [73] L. Viola, e-print: quant-ph/0404038 (2004).
- [74] L. Viola, E. Knill, and S. Lloyd, Phys. Rev. Lett. **82**, 2417 (1999).
- [75] D. A. Lidar, I. L. Chuang, and K. B. Whaley, Phys. Rev. Lett. **81**, 2594 (1998).
- [76] J. E. Ollerenshaw, D. A. Lidar, and L. E. Kay, Phys. Rev. Lett. **91**, 217904 (2003).
- [77] L. Viola, E. M. Fortunato, M. A. Pravia, E. Knill, R. Laflamme, and D. G. Cory, Science **293**, 2059 (2001).
- [78] J. Keeler, R. T. Clowes, A. L. Davis, and E. Laue, Methods Enzymol. **239**, 145 (1994).
- [79] M. J. Thrippleton and J. Keeler, Angew. Chem. Int. Ed. **42**, 3938 (2003).
- [80] U. Fano, Rev. Mod. Phys. **29**, 74 (1957).
- [81] G. Teklemariam, E. M. Fortunato, M. A. Pravia, Y. Sharf, T. F. Havel, D. G. Cory, A. Bhattacharyya, and J. Hou, Phys. Rev. A **66**, 012309 (2002).

- [82] M. Mehring, J. Mende, and W. Scherer, *Phys. Rev. Lett.* **90**, 153001 (2003).
- [83] G. L. Long, H. Y. Yan, and Y. Sun, *J. Opt. B: Quantum Semiclass. Opt.* **3**, 376 (2001).
- [84] J. J. Sakurai, *Modern Quantum Mechanics*, Addison-Wesley Publishing Company, 1994.
- [85] D. G. Cory, A. F. Fahmy, and T. F. Havel, in *PhysComp '96*, edited by T. Toffoli, M. Biafore, and J. Leão, pages 87–91, New England Complex Systems Institute, 1996.
- [86] O. W. Sørensen, *Prog. NMR Spectrosc.* **21**, 503 (1989).
- [87] E. Knill, I. Chuang, and R. Laflamme, *Phys. Rev. A* **57**, 3348 (1998).
- [88] R. Marx, A. F. Fahmy, J. M. Myers, W. Bermel, and S. J. Glaser, *Phys. Rev. A* **62**, 012310 (2000).
- [89] N. A. Gershenfeld and I. L. Chuang, *Science* **275**, 350 (1997).
- [90] L. M. K. Vandersypen, C. S. Yannoni, M. H. Sherwood, and I. L. Chuang, *Phys. Rev. Lett.* **83**, 3085 (1999).
- [91] E. Knill, R. Laflamme, and C.-H. Tseng, *Nature* **404**, 368 (2000).
- [92] W. S. Warren, *Science* **277**, 1688 (1997).
- [93] R. Blume-Kohout, C. M. Caves, and I. H. Deutsch, *Found. Phys.* **32**, 1641 (2002).
- [94] L. J. Schulman and U. Vazirani, in *Proc. 31'st STOC (ACM Symp. Theory Comp.)*, ACM Press, 1999.
- [95] D. E. Chang, L. M. K. Vandersypen, and M. Steffen, *Chem. Phys. Lett.* **338**, 337 (2001).
- [96] P. O. Boykin, T. Mor, V. Roychowdhury, F. Vatan, and R. Vrijen, *Proc. Natl. Acad. Sci.* **99**, 3388 (2002).
- [97] J. M. Fernandez, S. Lloyd, T. Mor, and V. Rowchowdhury, e-print: quant-ph/0401135 (2004).

- [98] P. Shor, Phys. Rev. A **52**, 2493 (1995).
- [99] A. Steane, Proc. R. Soc., London A **452**, 2551 (1996).
- [100] D. Leung, L. M. K. Vandersypen, X. L. Zhou, M. Sherwood, C. Yannoni, M. Kubinec, and I. Chuang, Phys. Rev. A **60**, 1924 (1999).
- [101] D. G. Cory, M. D. Price, W. Maas, E. Knill, R. Laflamme, W. H. Zurek, T. F. Havel, and S. S. Somaroo, Phys. Rev. Lett. **81**, 2152 (1998).
- [102] D. I. Hoult and B. Bhakar, Conc. Magn. Reson. **9**, 277 (1997).
- [103] D. Rugar, R. Budakian, H. J. Mamin, and B. W. Chui, Nature **430**, 329 (2004).
- [104] J. M. Elzerman, R. Hanson, L. H. W. van Beveren, B. Witkamp, L. M. K. Vandersypen, and L. P. Kouwenhoven, Nature **430**, 431 (2004).
- [105] J. Kohler, J. A. M. Disselhorst, M. C. J. M. Donkers, E. J. J. Groenen, J. Schmidt, and W. E. Moerner, Nature **363**, 242 (1993).
- [106] J. Wrachtrup, C. von Borczyskowski, J. Bernhard, M. Orrit, and R. Brown, Nature **363**, 244 (1993).
- [107] M. Eickhoff and D. Suter, J. Magn. Reson. **166**, 69 (2004).
- [108] E. Schrödinger, Proc. Cambridge Philos. Soc. **31**, 555 (1935).
- [109] C. H. Bennett, G. Brassard, C. Crépeau, R. Jozsa, A. Peres, and W. K. Wootters, Phys. Rev. Lett. **70**, 1895 (1993).
- [110] D. Bowmeester, J.-W. Pan, K. Mattle, M. Eibl, H. Weinfurter, and A. Zeilinger, Nature **390**, 575 (1997).
- [111] C. H. Bennett and S. J. Weisner, Phys. Rev. Lett. **69**, 2881 (1992).
- [112] K. Mattle, H. Weinfurter, P. G. Kwiat, and A. Zeilinger, Phys. Rev. Lett. **76**, 4656 (1996).
- [113] C. H. Bennett and G. Brassard, Quantum cryptography: public key distribution and coin tossing, in *Proceedings of IEEE Conference on Computers, Systems and Signal Processing*, page 175, IEEE, New York, 1984.

- [114] C. H. Bennett, F. Bessette, G. Brassard, L. Salvail, and J. Smolin, *J. Cryptology* **5**, 3 (1992).
- [115] R. Laflamme, D. G. Cory, C. Negreveregne, and L. Viola, *Quantum Inform. and Compu.* **1**, 1 (2001).
- [116] R. F. Werner, *Phys. Rev. A* **40**, 4277 (1989).
- [117] S. L. Braunstein, C. M. Caves, R. Jozsa, N. Linden, S. Popescu, and R. Schack, *Phys. Rev. Lett.* **83** (1999).
- [118] A. O. Pittenger and M. H. Rubin, *Opt. Commun.* **179**, 447 (2000).
- [119] L. Gurvits and H. Barnum, *Phys. Rev. A* **68**, 042312 (2003).
- [120] R. Schack and C. M. Caves, *J. Mod. Optic.* **47**, 387 (2000).
- [121] S. J. Glaser, T. Schulte-Herbrüggen, M. Sieveking, O. Schedletsky, N. C. Nielsen, O. W. Sørensen, and C. Griesinger, *Science* **280**, 421 (1998).
- [122] A. Peres, *Phys. Rev. Lett.* **77**, 1413 (1996).
- [123] R. Schack and C. M. Caves, *Phys. Rev. A* **60**, 4354 (1999).
- [124] H. Ollivier and W. H. Zurek, *Phys. Rev. Lett.* **88**, 017901 (2002).
- [125] E. Biham, G. Brassard, D. Kenigsberg, and T. Mor, *Theor. Comp. Sci.* **320**, 15 (2004).
- [126] A. Ekert and R. Jozsa, *Phil. Trans. R. Soc. London Ser. A* **356**, 1769 (1998).
- [127] P. W. Shor, Algorithms for quantum computation: discrete logarithm and factoring, in *Proceedings of the 35th Annual Symposium on Fundamentals of Computer Science*, page 124, 1994.
- [128] M. Lewenstein, J. I. C. D. Bruß, B. Kraus, M. Kus, J. Samsonowicz, A. Sanpera, and R. Tarrach, *J. Mod. Optic.* **47**, 2481 (2000).
- [129] D. Bruß, *J. Math. Phys.* **43**, 4237 (2002).
- [130] M. Horodecki, P. Horodecki, and R. Horodecki, *Physics Letters A*. **223**, 1 (1996).

- [131] P. Horodecki, Phys. Lett. A **232**, 333 (1997).
- [132] M. Horodecki, P. Horodecki, and R. Horodecki, Phys. Rev. Lett. **80**, 5239 (1998).
- [133] W. Dür, J. I. Cirac, and R. Tarrach, Phys. Rev. Lett. **83**, 3562 (1999).
- [134] V. Vedral, M. B. Plenio, M. A. Rippin, and P. L. Knight, Phys. Rev. Lett. **78**, 2275 (1997).
- [135] C. H. Bennett, D. P. DiVincenzo, J. A. Smolin, and W. K. Wootters, Phys. Rev. A. **54**, 3824 (1996).
- [136] W. K. Wootters, Phys. Rev. Lett. **80**, 2245 (1997).
- [137] R. Horodecki and M. Horodecki, Phys. Rev. A **54**, 1838 (1996).
- [138] T. Schulte-Herbrüggen and O. W. Sørensen, Conc. Magn. Reson. **12**, 389 (2000).
- [139] A. W. Overhauser, Phys. Rev. **91**, 476 (1953).
- [140] A. W. Overhauser, Phys. Rev. **92**, 411 (1953).
- [141] H. Kurreck, B. Kirste, and W. Lubitz, Angew. Chem. Int. Ed. Engl. **23**, 173 (1984).
- [142] J. H. Ardenkjær-Larsen, B. Fridlund, A. Gram, G. Hansson, L. Hansson, M. H. Lertche, R. Servin, M. Thanning, and K. Golman, Proc. Natl. Acad. Sci. **100**, 10158 (2003).
- [143] B. M. Goodson, J. Magn. Res. **155**, 157 (2002).
- [144] E. Brunner, Conc. Magn. Res. **11**, 313 (1999).
- [145] G. Navon, Y. Q. Song, T. Room, A. Appelt, R. E. Taylor, and A. Pines, Science **271**, 1848 (1996).
- [146] Y. Q. Song, Conc. Magn. Reson. **12**, 6 (1999).
- [147] J. J. Heckman, M. P. Ledbetter, and M. V. Romalis, Phys. Rev. Lett. **91**, 067601 (2003).
- [148] A. S. Verhulst, O. Liivak, M. H. Sherwood, H. Vieth, and I. L. Chuang, Appl. Phys. Lett. **79**, 2480 (2001).

- [149] P. W. Atkins, *Physical Chemistry*, Oxford University Press, 1994.
- [150] S. B. Duckett and C. J. Sleigh, *Prog. NMR Spectrosc* **34**, 71 (1999).
- [151] K. Golman, O. Axelsson, H. Jóhannesson, S. Månsson, C. Olofsson, and J. S. Petersson, *Magn. Reson. Med.* **46**, 1 (2001).
- [152] P. Hübler, J. Bargon, and S. J. Glaser, *J. Chem. Phys.* **113**, 2056 (2000).
- [153] D. Blazina, S. B. Duckett, T. K. Halstead, C. M. Kozak, R. J. K. Taylor, M. S. Anwar, J. A. Jones, and H. A. Carteret, *Magn. Reson. Chem.* (Submitted) (2004).
- [154] M. S. Anwar, D. Blazina, H. A. Carteret, S. B. Duckett, and J. A. Jones, *Chem. Phys. Lett.* (In Press), e-print: quant-ph/0407091 (2004).
- [155] D. P. Weitekamp, Sensitivity enhancement through spin statistics, in *Encyclopedia of NMR*, edited by D. M. Grant and R. K. Harris, page 696, Wiley, New York, 1996.
- [156] C. R. Bowers and D. P. Weitekamp, *Phys. Rev. Lett.* **57**, 2645 (1986).
- [157] M. de Angelis, G. Gagliardi, L. Gianfrani, and G. M. Tino, *Phys. Rev. Lett.* **76**, 2840 (1996).
- [158] G. Modugno, M. Inguscio, and G. M. Tino, *Phys. Rev. Lett.* **81**, 4790 (1998).
- [159] R. Shankar, *Principles of Quantum Mechanics*, Kluwer Academic/Plenum Publishers, 1994.
- [160] J. Natterer and J. Bargon, *Prog. NMR Spectrosc.* **31** (1997).
- [161] C. R. Bowers, D. H. Jones, N. D. Karur, J. A. Labinger, M. G. Pravica, and D. P. Weitekamp, *Adv. Magn. Reson.* **15**, 269 (1990).
- [162] I. F. Silvera, *Rev. Mod. Phys.* **52**, 393 (1980).
- [163] G. Herzberg, *Molecular Spectra and Molecular Structure*, volume 1, Van Nostrand Reinhold Company, 1950.
- [164] J. M. Hollas, *Modern Spectroscopy*, John Wiley and Sons, 1987.

- [165] C. N. Banwell, *Fundamentals of Molecular Spectroscopy*, McGraw-Hill Book Company (UK) Limited, 1983.
- [166] G. Arfken, *Mathematical Methods for Physicists*, Academic Press, 1985.
- [167] M. G. Pravica and I. F. Silvera, Phys. Rev. Lett. **81**, 4180 (1998).
- [168] A. M. Juarez, D. Cubric, and C. C. King, Meas. Sci. Tech. **13**, N52 (1998).
- [169] V. I. Tikhonov and A. A. Volkov, Science **296**, 2363 (2002).
- [170] J. Crovisier, K. Leech, D. Bockelée-Morvan, T. Y. Brooke, M. S. Hanner, B. Altieri, H. U. Keller, and E. Lellouch, Science **275**, 1904 (1997).
- [171] A. Miani and J. Tennyson, J. Chem. Phys. **120**, 2732 (2004).
- [172] D. L. Andrews, *Lasers in Chemistry*, Springer-Verlag, 1986.
- [173] C. Godard, P. Callaghan, J. L. Cunningham, S. B. Duckett, J. A. B. Lohman, and R. N. Perutz, Chem. Comm. **23**, 2836 (2002).
- [174] D. Schott, C. J. Sleight, J. P. Lowe, S. B. Duckett, R. J. Mawby, and M. G. Partridge, Inorg. Chem. **41**, 2960 (2002).
- [175] L. Cronin, M. C. Nicasio, R. N. Perutz, R. G. Peters, D. M. Roddick, and M. K. Whittlesey, J. Am. Chem. Soc. **117**, 10047 (1995).
- [176] C. R. Bowers, *Para-hydrogen and Synthesis Allow Dramatic Enhanced Nuclear Alignment*, PhD thesis, California Institute of Technology, 1991.
- [177] M. G. Pravica and D. P. Weitekamp, Chem. Phys. Lett. **145**, 255 (1988).
- [178] G. Buntkowsky, J. Bargon, and H. H. Limbach, J. Am. Chem. Soc. **118**, 8677 (1996).
- [179] A. J. Moulé, M. M. Spence, S.-I. Han, J. A. Seeley, K. L. Pierce, S. Saxena, and A. Pines, Proc. Natl. Acad. Sci. **100**, 9122 (2003).
- [180] P. F. Siedler, H. E. Bryndza, J. E. Frommer, L. S. Stuhl, and R. G. Bergman, Organometallics **2**, 1701 (1983).
- [181] S. J. Glaser and J. J. Quant, Adv. Magn. Optic. Reson. **19**, 59 (1996).

- [182] Y. S. Weinstein, T. F. Havel, J. Emerson, N. Boulant, M. Saraceno, S. Lloyd, and D. G. Cory, (2004).
- [183] R. Marx and S. J. Glaser, J. Magn. Reson. **164**, 338 (2003).
- [184] L. Braunschweiler and R. R. Ernst, J. Magn. Reson. **53**, 521 (1983).
- [185] U. Haeberlen and J. S. Waugh, Phys. Rev. **175**, 453 (1968).
- [186] M. H. Levitt, R. Freeman, and T. Frenkiel, J. Magn. Reson. **47**, 328 (1982).
- [187] S. W. Homans, *A Dictionary of Concepts in NMR*, Clarendon Press, Oxford, 1989.
- [188] N. Linden, H. Barjat, E. Kupce, and R. Freeman, Chem. Phys. Lett. **296**, 61 (1998).
- [189] R. Freeman, Prog. NMR Spectrosc. **32**, 59 (1997).
- [190] A. J. Shaka, P. B. Barker, and R. Freeman, J. Magn. Reson. **64**, 547 (1985).
- [191] J. C. Hoch and A. S. Stern, *NMR Data Processing*, Wiley-Liss, Inc., 1996.
- [192] J. C. Lindon and A. G. Ferridge, Prog. NMR Spectrosc. **14**, 27 (1980).
- [193] An Awk Tutorial, <http://www.vectorsite.net/tsawk.html>.
- [194] Grace User's Guide (for Grace-5.1.10), <http://plasma-gate.weizmann.ac.il/grace/doc/usersguide>.
- [195] R. N. Bracewell, *The Fourier Transform and its Applications*, McGraw-Hill Book Company, 1986.
- [196] L. McIntyre and R. Freeman, J. Magn. Reson. **96**, 425 (1992).
- [197] J. A. Jones, Conc. Magn. Reson. **8**, 175 (1996).
- [198] D. Deutsch and R. Jozsa, Proc. R. Soc. London Ser. A **439**, 553 (1992).
- [199] R. Cleve, A. Ekert, C. Macchiavello, and M. Mosca, Proc. R. Soc. London Ser. A **454**, 339 (1998).
- [200] B. Eastin and S. T. Flammia, Q-circuit tutorial, e-print: quant-ph/0406003 (2004).

- [201] L. K. Grover, Phys. Rev. Lett. **79**, 2645 (1986).
- [202] C. H. Bennett, G. Brassard, S. Popescu, B. Schumacher, J. A. Smolin, and W. K. Wootters, Phys. Rev. Lett. **76**, 722 (1996).
- [203] D. Deutsch, A. Ekert, R. Jozsa, C. Macchiavello, S. Popescu, and A. Sanpera, **77**, 2818 (1996).
- [204] N. A. Peters, J. B. Altepeter, D. Branning, E. R. Jeffrey, T. C. Wei, and P. G. Kwiat, Phys. Rev. Lett. **90**, 193601 (2003).
- [205] M. S. Anwar, L. Xiao, A. J. Short, J. A. Jones, D. Blazina, S. B. Duckett, and H. A. Carteret, Phys. Rev. A (Submitted), e-print:quant-ph/0409142 (2004).
- [206] M. A. Nielsen, E. Knill, and R. Laflamme, Nature **396**, 52 (1998).
- [207] V. D. Kleiman, H. Park, R. J. Gordon, and R. N. Zare, *Companion to Angular Momentum*, John Wiley and Sons, Inc., London, 1998.
- [208] H. F. Jones, *Groups, Representations and Physics*, Institute of Physics Publishing, Bristol and Philadelphia, 1996.
- [209] A. Bax, N. M. Szeverenyi, and G. E. Maciel, J. Magn. Reson. **52**, 147 (1983).
- [210] P. K. Aravind, Phys. Lett. A **233**, 7 (1997).
- [211] E. Knill and R. Laflamme, Phys. Rev. Lett. **81**, 5672 (1998).
- [212] D. Poulin, R. Laflamme, G. J. Milburn, and J. P. Paz, Phys. Rev. A **68**, 022302 (2003).
- [213] W. V. Dam, M. Mosca, and U. Vazirani, e-print: quant-ph/0206003 (2003).
- [214] V. Murg and J. I. Cirac, Phys. Rev. A **69**, 042320 (2004).
- [215] J. S. Waugh, J. Magn. Reson. **50**, 30 (1982).
- [216] P. A. Jansson, Convolution and related concepts, in *Deconvolution: with Applications in Spectroscopy*, edited by P. A. Jansson, pages 1–34, Academic Press, New York, 1984.
- [217] P. Huber and G. Bodenhausen, J. Magn. Reson., Ser. A **102**, 81 (1993).

- [218] K. Kraus, *State, Effects, and Operations*, Springer, Berlin, 1983.
- [219] B. Schumacher, Phys. Rev. A **54**, 2614 (1996).
- [220] I. Solomon, Phys. Rev. **99**, 559 (1955).

